Sapienza
Università di Roma

Search for the Standard Model Higgs Boson in the $H \to ZZ^* \to \ell^+\ell^- q\bar{q}$ final state with the ATLAS detector at the LHC

Scuola di dottorato in Fisica

Dottorato di Ricerca in Fisica – XXV Ciclo

Candidate

Francesco Lo Sterzo
ID number 1063889

Thesis Advisors

Prof. Claudio Luci
Dr. Marco Rescigno

A thesis submitted in partial fulfillment of the requirements
for the degree of Doctor of Philosophy in Physics

October 2012

Thesis not yet defended

Francesco Lo Sterzo. *Search for the Standard Model Higgs Boson in the $H \to ZZ^* \to \ell^+\ell^- q\bar{q}$ final state with the ATLAS detector at the LHC.*

Ph.D. thesis. Sapienza – University of Rome

VERSION: October 12, 2012

EMAIL: francesco.losterzo@roma1.infn.it

Contents

Introduction

The Standard Model of elementary particles is the theory our comprehension of the subatomic world is based on. It is the most successful and precise scientific theory ever elaborated: during all the past century its predictions have been confirmed to unprecedented degree of precision by many experiments involving different experimental techniques and aimed at studying very different subatomic phenomena. The theoretical consistency of the Standard Model relies on the existence of the Higgs boson, a scalar particle theorized in 1964.

The mass of the Higgs boson is not constrained by the theory, and it is allowed to vary in a very wide range. In the past decades many experiments have performed unsuccessful Higgs boson searches, but nevertheless they have been able to set limits on its existence. The searches performed at the LEP collider, operating at CERN up to 2000, excluded the existence of the Higgs boson setting a lower bound on its mass at $m_H = 114.4$ GeV/c^2, while the searches performed at the TeVatron collider at Fermilab have excluded the presence of the Higgs boson in the mass range $147 - 180$ GeV/c^2.

Searches for the Higgs boson have been performed also at the Large Hadron Collider (LHC), the pp collider which is operational at CERN since 2008. It has been colliding protons at a center of mass energy of 7 TeV in 2010 and 2011, while the colliding energy has been raised to 8 TeV in 2012.

The ATLAS detector is one of the four main experiments which records and analyses the pp collision provided by the LHC. It is a multi-purpose detector whose main goal is the discovery and the measurement of any new phenomenon arising beyond the Standard Model, be it the Higgs boson or anything else.

At the LHC a very wide Higgs boson mass range can be probed and, as a function of its postulated mass, different decay processes may take place, offering several experimental challenges. One of its main decay channels is the $H \to ZZ^*$, in which the Higgs boson decays into two Z boson, one of which may be virtual depending on the Higgs boson mass. The final state of this process depends on the decay of the two Z bosons: requiring at least one of them to decay into light charged leptons reduces the possible sources of background at an hadron collider.

An Higgs-like particle has actually been discovered, and its discovery has been made public on July 4th 2012. The search presented in this thesis has been developed throughout the last year and an half with the aim of contributing with as much information and data as possible to the Higgs boson search.

In this thesis a search for the Higgs boson in the low mass range ($120 < m_H < 180$ GeV/c^2) using the $H \to ZZ^* \to \ell^+\ell^- q\bar{q}$ decay process has been performed, with 4.7 fb^{-1} of data collected by the ATLAS detector in the 2011 LHC run. This is a very challenging search because of two main reasons. The presence of jets arising from quarks in the final state may allow great background contamination, since background processes with jets are very abundant and therefore an high background rejection is needed in order to achieve competitive results. Moreover the jets are complex objects and performances of identification, reconstruction and measurements of their parameters may not be as effective as for the leptons. In addition to this, the presence of one off mass-shell Z boson introduces further complications, since just one of the final state pairs (either the $\ell\ell$ or the $q\bar{q}$ pair) can be constrained to the Z boson mass. On the other hand this final state offers an high production cross section, since takes advantage of the $BR(Z \to q\bar{q})$.

The first Chapter of this thesis offers brief summary of the theoretical structure of the Standard Model and the reason why an Higgs boson is needed to let it be consistent. Furthermore a summary of the experimental Higgs boson searches performed in the past decades is given, as well as an introduction to the Higgs boson search at the LHC, with a detailed explanation of the $H \to ZZ^* \to \ell^+\ell^- q\bar{q}$ process.

In Chapter 2 a description of the experimental apparatus used to perform the measure is given. The Large Hadron Collider is introduced, and the ATLAS detector is described in all it subparts.

The final state physics objects on which this analysis is based are muons, electrons, jets and missing energy, hence a detailed overview of the algorithms used in ATLAS to identify and reconstruct them is given in Chapter 3.

Chapter 4 gives an overview and a description of the Monte Carlo programs used to model the background and the signal processes throughout the analysis, while in Chapter 5 a detailed description of the analysis is given. In this chapter the several challenges of this analysis are reviewed in detail and a full description of the methods developed to face them is given.

In Chapter 6 the events passing the full selection are analyzed in detail to probe the presence of any signal compatible with the Higgs boson. This is done by means of the advanced statistical techniques described in this chapter. Once the final result is obtained a detailed comparison with other similar results available from both the ATLAS and CMS experiments is given.

Chapter 1

The Higgs Boson

This Chapter will give an introduction to the current theoretical panorama in elementary particle physics: the Standard Model will be described, as well as the Higgs mechanism and its consequences. The Higgs mechanism is needed in order to have a theory describing properly the phenomena we observe. After the first theoretical approach we will give a summary of the experimental results from the previous searches for the Higg boson performed at CERN and Fermilab with the LEP the TeVatron accelerators respectively. An introduction to the Higgs searches at Large Hadron Collider (LHC) will be given with particular attention to the $H \to ZZ^{(*)} \to llqq$ channel.

1.1 The Standard Model

The current understanding of the sub-atomic particles and their behaviour is based on the Standard Model. It is a physical theory which gives a very accurate quantitative description of three of the four fundamental forces observed in nature: the electromagnetism, the weak interactions and the strong nuclear force. This theory was developed at the end of 1960's putting together several studies carried out by different people [1, 2, 3, 4]: it is a renormalizable field theory compatible with special relativity, and during the past decades all its predictions have been confirmed with very high precision [6].

The Standard Model (SM) Lagrangian describes a non-Abelian gauge symmetry which refers to the group $SU(3) \times SU(2) \times U(1)$, in which the $SU(3)$ group refers to the *Quantum Chromodynamics* (QCD), the theory describing the interactions of quark and gluons due to the colour charge, while the $SU(2) \times U(1)$ group refers to the *electroweak* interactions. Given this separation, the SM Lagrangian can be written as follows:

$$\mathscr{L}_{SM} = \mathscr{L}_{QCD} + \mathscr{L}_{EW} \tag{1.1}$$

The $\mathscr{L}_{QCD}$ term describes the $SU(3)_C$ group (C stands for the colour charge) and its analytical form is:

$$\mathscr{L}_{QCD} = -\frac{1}{4}\sum_i F^i_{\mu\nu}F^{i,\mu\nu} + i\sum_r \bar{q}_{r\alpha}\gamma^\mu D^\alpha_{\mu\beta} q^\beta_r \tag{1.2}$$

In this formula the $F^i_{\mu\nu}$ tensors are defined as:

$$F^i_{\mu\nu} = \partial_\mu G^i_\nu - \partial_\nu G^i_\mu - g_F f_{ijk} G^j_\mu G^k_\nu \tag{1.3}$$

where G^i ($i = 1, ..., 8$) are the 8 gluon field, g_F is the strong coupling constant and f_{ijk} are the $SU(3)$ structure constants. In the second term of eq. 1.2 q_r is the quark field of flavour r, α and β are the colour indexes and the covariant derivative $D^{\alpha}_{\mu\beta}$ is defined as:

$$D^{\alpha}_{\mu\beta} = \partial_\mu \delta^{\alpha}_{\beta} + \frac{i}{2} g_F \sum_i G^i_\mu \lambda^{i,\alpha}_{\beta} \tag{1.4}$$

where λ^i are the generator matrices of $SU(3)$. The above Lagrangian describes quarks q_r interacting by means of gluons, and the first term of eq. 1.2 describes the gluon dynamics, including the self-interacting term derived by the non-Abelian nature of the $SU(3)$ symmetry.

The Electroweak lagrangian describes the $SU(2)_L \times U(1)_Y$ group, where the $SU(2)_L$ group refers to the weak isospin (I) and the $U(1)_Y$ group refers to the weak hypercharge (Y). In this picture the left-handed (L) fermions are coupled in $I = 1/2$ doublets, while the the right-handed fermions (R) are organized in $I = 0$ singlets.

$$I = 0 : \begin{array}{c} (e)_R,\ (\mu)_R,\ (\tau)_R \\ (u)_R,\ (c)_R,\ (t)_R \\ (d)_R,\ (s)_R,\ (b)_R \end{array}$$

$$I = \frac{1}{2} : \begin{array}{c} \binom{\nu_e}{e}_L,\ \binom{\nu_\mu}{\mu}_L,\ \binom{\nu_\tau}{\tau}_L \\ \binom{u}{d}_L,\ \binom{c}{s}_L,\ \binom{t}{b}_L \end{array}$$

The request of the local gauge invariance leads to the introduction of four vector bosons: the W^i fields ($i = 1, 2, 3$) for the $SU(2)_L$ group and the B field for $U(1)_Y$. From these four fields it is possible to obtain the physical fields combining them:

$$A_\mu = B_\mu \cos\theta_W + W^3_\mu \sin\theta_W \tag{1.5}$$

$$Z_\mu = W^3_\mu \cos\theta_W - B_\mu \sin\theta_W \tag{1.6}$$

$$W^{\pm}_\mu = \frac{W^1_\mu \mp i W^2_\mu}{\sqrt{2}} \tag{1.7}$$

where A_μ is the photon field, Z_μ is the field associated to the neutral Z^0 boson and $W^{\pm}_\mu$ are the fields describing the two charged W bosons. In the previous equations the weak mixing angle θ_W has been introduced. The analytical form for this lagrangian is:

$$\mathscr{L}_{EW} = -\frac{1}{4} \sum_G F^{\mu\nu}_G F_{\mu\nu\,G} + i \sum_f \bar{f} D_\mu \gamma^\mu f \tag{1.8}$$

where the two indexes G and f indicate that the two sums are extended to all the vectorial and fermionic fields respectively. More in detail the $F^{\mu\nu}_G$ tensors describe the dynamics of the four bosons in the theory, while the second term in equation 1.8 describes the interaction between the fermions which are mediate by the four boson. This kind of interaction is contained into the definition of the covariant derivative D_μ:

$$D_\mu = \partial_\mu - i g_G (\lambda^\alpha G_\alpha)_\mu \tag{1.9}$$

where g_G is the coupling constant to the G field ($G = A, Z, W^+, W^-$) and λ^α stands for the generators of the group to which the G field refers.

The Standard Model thus obtained is invariant under local gauge transformations, and it describes massless particles (no mass-like terms are contained in the above formulas). This contradicts the experimental evidence according to which the particles we observe in nature have non-zero masses (with some exceptions, like the photon). In addition it is impossible to add the mass terms into the lagrangian in eq. 1.1 without spoiling its gauge invariance. A theoretical solution to this problem was proposed the mid-1960 [7, 8, 9, 10, 11] invoking the spontaneous breaking of the lagrangian's symmetry, and it is known as *the Higgs mechanism*.

1.2 The Higgs Mechanism

The problem to preserve the invariance under local gauge transformations of the SM lagrangian introducing at the same time the mass terms for the particles (which would explicitly break such a symmetry if added by hand) is solved by the usage of the *spontaneous symmetry breaking*: in such a way the symmetry is not broken by terms added by hand (i.e. the mass terms), but it is broken by the intrinsic features of the fields involved in the theory. The simplest way to introduce this mechanism into the SM lagrangian is to add a new $SU(2)_L$ doublet of complex scalar fields

$$\phi = \begin{pmatrix} \phi^+ \\ \phi^0 \end{pmatrix} \tag{1.10}$$

the self-interaction of which leads to the spontaneous breaking of the electroweak symmetry. The additional term to the SM lagrangian involving this new field is

$$\mathscr{L}_H = (D_\mu\phi)^\dagger(D^\mu\phi) - V(\phi) \tag{1.11}$$

$$D^\mu = \partial^\mu + \frac{i}{2}g\tau_j W_j^\mu + \frac{1}{2}g'YB^\mu \tag{1.12}$$

where the sum over the index $j = 1, 2, 3$ is implied, τ_j are the Pauli matrices, g and g' are the coupling constants of fermions to the W^μ and B^μ respectively and Y is the weak hypercharge operator. The most general form of the scalar potential $V(\phi)$ in eq. 1.11 is

$$V(\phi) = \mu^2\phi^\dagger\phi + \lambda(\phi^\dagger\phi)^2 = \mu^2|\phi|^2 + \lambda|\phi|^4 \tag{1.13}$$

The actual shape of the potential $V(\phi)$ depends on the values of the two parameters μ and λ: the request $\lambda > 0$ ensures the existence of a lower bound for $V(\phi)$ and therefore guarantees the existence of a ground state for such a potential. If the parameter μ is chosen so that $\mu^2 < 0$ then the symmetry of the $V(\phi)$ potential can be broken, since its ground state occurs for

$$|\phi|^2 = -\frac{\mu^2}{2\lambda} = \frac{v^2}{2} \tag{1.14}$$

and its shape is shown in figure 1.1. Equation 1.14 tells that the ground state of the $V(\phi)$ potential (i.e. the physical vacuum state) occurs for a non-vanishing value of the ϕ field. The ground state thus obtained is not symmetric under $SU(2)_L \times U(1)_Y$ transformations since there is a preferred direction, and the symmetry is then spontaneously broken. In the above, the ϕ field is the Higgs field.

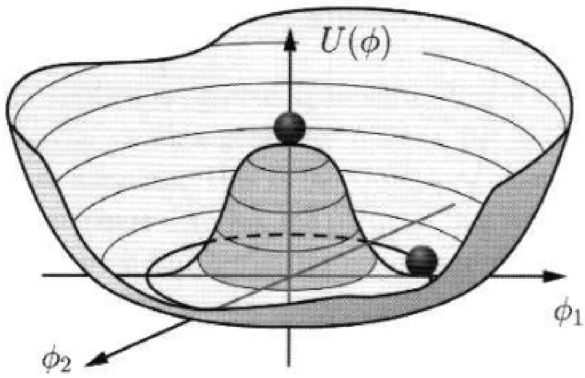

Figure 1.1. Shape of the $V(\phi)$ potential for $\mu^2 < 0$ and $\lambda > 0$

The physical content of this mechanism, the Higgs mechanism, is revealed studying the perturbative expansion of the lagrangian around its ground state. In general the ϕ field around the grond state can be expressed as

$$\phi = \frac{1}{\sqrt{2}}\begin{pmatrix} 0 \\ v + h(x) \end{pmatrix} \tag{1.15}$$

where the imaginary part of the perturbative field is absorbed by the local nature of the gauge invariance of the theory (*unitary gauge*) and $h(x)$ is a real function, without loosing generality. The Higgs field $\phi(x)$ describes a scalar neutral particle, the Higgs boson, of mass

$$m_H = \sqrt{2}\mu = \sqrt{2\lambda}v \tag{1.16}$$

The value of m_H depends on μ (λ and v) and is therefore unpredictable and it is a free parameter of the theory.

1.2.1 The masses of the gauge bosons

In the Higgs mechanism the generation of the masses is given by the interaction of the Higgs field ϕ with the particles fields. For the gauge bosons this interaction takes place through the covariant derivative D^μ in eq. 1.12: expanding around the ground state in terms of the $SU(2)_L \times U(1)_Y$ fields $((W^i)^\mu, B^\mu)$ one can obtain (only the mass terms):

$$g^2 W^i_\mu (W^j)^\mu \left[\phi \frac{\tau_i \tau_j}{4}\phi\right] - (g')^2 \frac{1}{4}\frac{v^2}{2} B_\mu B^\mu + 2gg' W^3_\mu B^\mu \left[\phi \frac{\tau_3}{4}\phi\right] \tag{1.17}$$

from which one can exract the mass terms for the three vectorial fields in eq. 1.5 in form of a matrix:

$$\mathbf{M} = \frac{1}{4}v^2 \begin{pmatrix} g^2 & -gg' \\ -gg' & (g')^2 \end{pmatrix}$$

the $\mathbf{M}$ matrix satisfies the condition $det\mathbf{M} = 0$ and this implies the existence of an eigenstate with zero mass. Using the combinations in eq. 1.5 and requiring A^μ to be the massless field one can obtain:

$$\tan\theta = \frac{g'}{g} \tag{1.18}$$

that is the relation which says that the field A^μ couples to the electron through the electromagnetic current. For the other non-zero eigenvalues one can obtain:

$$M_W = \tfrac{vg}{2} \qquad \text{for the } W^\pm_\mu \text{ fields}$$

$$M_Z = \tfrac{v}{2}\sqrt{g^2 + g'^2} \qquad \text{for the } Z_\mu \text{ field}$$

1.2.2 Fermion masses

The fermion masses arise from the Higgs mechanism when a Yukawa coupling between the Higgs field ϕ and the fermionic fields is added. For a generic fermionic field, the additional term to the lagrangian is:

$$\mathscr{L} = -g_\psi(\bar{\psi}^L \phi \psi^R) + h.c. \tag{1.19}$$

where g_ψ is the coupling constant of the fermionic field ψ to the Higgs field. Expanding eq. 1.19 around the ground state of the Higgs field, it is possible to derive the mass term for the generic field ψ that is

$$m_\psi = g_\psi v/\sqrt{2} \tag{1.20}$$

In the above procedure it is possible to consider the possibility that the mass terms are not diagonal in the ψ^R and ψ^L fields, thus opening the chance to describe the observed quark mixing in weak interactions.

From equations 1.20 and 1.2.1 it is possible to see that the Higgs coupling to bosons and fermions is a function of the free parameter v, as well as m_H (eq. 1.16). Combining these informations one can see that the Higgs couplings (and then its production and decay processes) strongly depend on its own mass (fig. 1.6 and 1.8).

The problem of the mass generation in the Standard Model is thus solved by the introduction of a new scalar field $\phi(x)$. This field confers mass to fermions and bosons through its interaction with the fields themselves. This new field describes a new massive, neutral, scalar particle: the Higgs boson.

1.3 Experimental Searches for the Higgs Boson

The search for the Higgs boson has been one of the most important and challenging searches in the past decades at the particles colliders. A brief summary of the Higgs searches performed before the LHC start is given in this section. Experimental limits on its mass are of two kinds: direct limits coming from direct Higgs searches performed at colliders like LEP at CERN and TeVatron at Fermilab, and indirect limits, arising from precision measurements of the electroweak parameters.

The LEP machine was an e^+e^- collider which was operative at CERN from 1989 to 2000. In the first phase of its operations (LEP I) it provided collision at $89 < \sqrt{s} < 93$ GeV to perform precision studies on the recently discovered Z boson, while in the second phase (LEP II) the search for the Higgs boson became one of its main goals, and collision where recorded at increasing energy up to $\sqrt{s} = 210$ GeV. The main Higgs production mechanism at LEP was the so-called "associate production" (also known as "Higgs-strahlung"), in which an Higgs boson

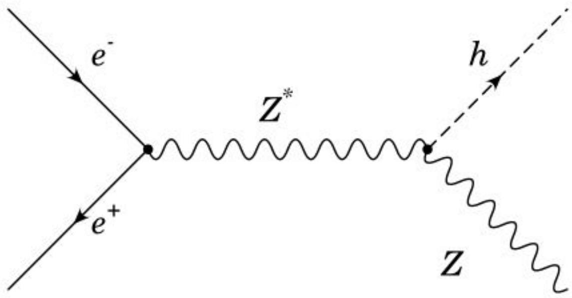

Figure 1.2. Feynman diagram of the Higgs boson associate production

is radiated by a virtual Z boson (fig. 1.2): $e^+e^- \to Z^* \to ZH$. In the Higgs mass range allowed by the LEP colliding energy the main decay processes for the Higgs boson were the $H \to b\bar{b}$ and the $H \to \tau^+\tau^-$ final states. The LEP machine provided data to four detector experiments: ALEPH [12], DELPHI [13], L3 [14] and OPAL [15]. The combined result of the searh for the Higgs boson performed by the four experiments didn't show any relevant excess, and the final result is shown in fig. 1.3: the test statistics is

$$-2\ln Q = -2\ln \frac{\mathcal{L}_{\int}}{\mathcal{L}_{\lfloor}}$$

where $\mathcal{L}_{\lfloor}$ and $\mathcal{L}_{\int}$ are the likelihood of the background only and signal plus background hypotheses respectively. From fig. 1.3 one can deduce that up to a Higgs mass of 114.4 GeV/c^2 the observed data are consistent with the background only hypothesis.

The TeVatron is a proton-antiproton collider operating in the so called RUN II at a center of mass energy of 1.96 TeV and it has been taking data up to 2011 providing data to two detector experiments: CDF [16] and D0 [17]. The main Higgs production mechanism at the TeVatron collider was the associate production including also the W boson ($p\bar{p} \to VH, V = W^{\pm}, Z$), while the main decay channels include also the decay to pairs of vector bosons ($H \to ZZ^*$ and $H \to W^+W^-$) because of the wider mass range accessible at the TeVatron. The results of the combined search of CDF and D0 are shown in figure 1.4, [18]: the 95% confidence level upper limit on the ratio of the Higgs boson production to the SM expectation is shown as a function of the Higgs boson mass. As can be seen the observed limit goes below unity in the interval $147 < m_H < 180$ GeV/c and therefore the presence of the Higgs boson is excluded in this mass range with a 95% confidence level.

The indirect constraints to the Higgs mass come from a fit to the precision measurements performed in the electroweak sector of the Standard Model: these variables are sensitive to the Higgs mass as this can modify, through loop corrections, the vacuum polarization of the W and Z bosons. The variations of the χ^2 of this fit to the data collected by the LEP, TeVatron and SLC accelerators are shown in fig. 1.5. The main result of this fit is that the low mass region (compatible with LEP and TeVatron results) is favoured, but also the high-mass region is not excluded.

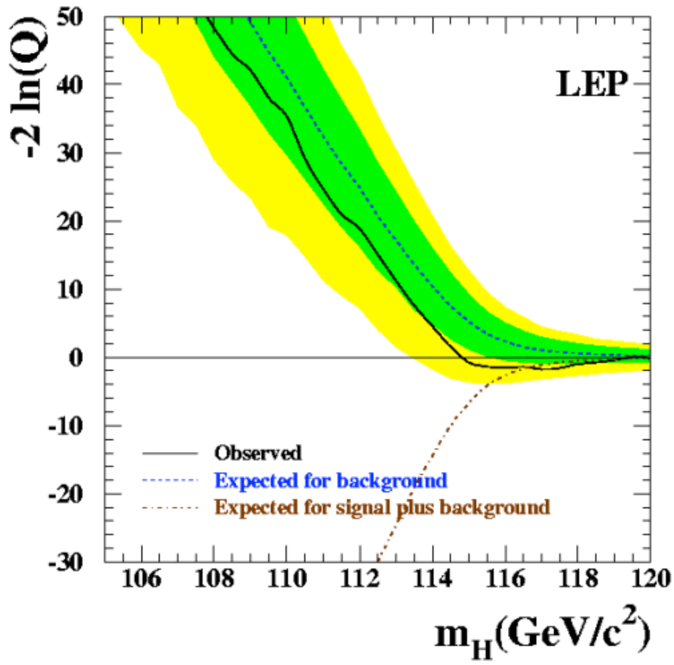

Figure 1.3. Combined results of the direct Higgs search preformed by the four experiments at LEP. The expected trend of the $-2lnQ$ variable is shown for the background only hypothesis (blue dashed line), for the signal plus background hypothesis (brown hashed line) and the observed one (black solid line). The green and the yellow bands represent the 68% and 95% probability intervals respectively

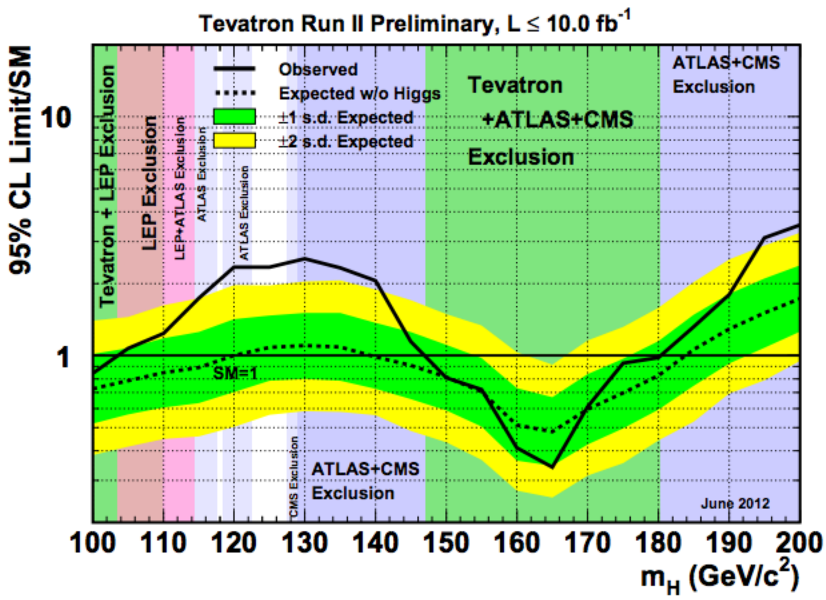

Figure 1.4. Combined results of the Higgs searches by the CDF and D0 collaborations: the expected (dashed line) and observed (solid line) limits at 95% of confidence level are shown as well as the mass regions excluded by all the experiments

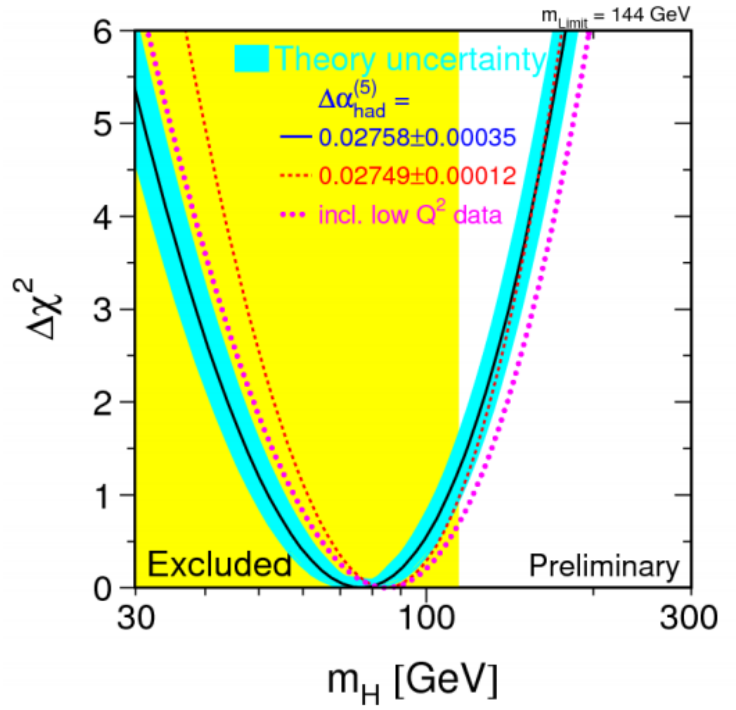

Figure 1.5. Variation of the χ^2 of the electroweak fit as a function of the Higgs boson mass

1.4 The Higgs Boson at the LHC

The Large Hadron Collider is a proton-proton collider which is operating at CERN since 2009. It has been operating at $\sqrt{s} = 7$ TeV in 2010 and 2011 and at $\sqrt{s} = 8$ TeV in 2012. Further details about the accelerating machine and the detectors recording the collisions will be given in chapter 2, while the Higgs boson production and decay mechanisms at LHC will be discussed in the following.

The Higgs mass range that is accessible at the LHC is very wide, and goes from below 100 GeV up to about 1 TeV. The main Higgs production mechanisms at the LHC and their cross sections are shown in fig. 1.6, as a function of the Higgs mass. The dominant production mechanism over all the mass spectrum is the *gluon fusion*. The subleading process is the *vector-boson fusion* in which two vector bosons (W or Z) are radiated from the partons in the initial state and give rise to an Higgs boson. Feynman's diagrams for these two processes are shown in fig. 1.7. Associate production with either a W, or Z boson or event with a $t\bar{t}$ pair are expected to give a minor contribution.

The Higgs decay channels and branching ratios strongly depend on the Higgs mass, and therefore the experimental strategies vary in the available mass spectrum. The Higgs branching ratios as a function of the boson mass are shown in fig. 1.8. In the low mass range ($m_H \lesssim 135$ GeV/c^2) the dominant decay channel is $H \to b\bar{b}$ but this process is very hard to be identified and studied at an hadron collider: the QCD processes, which are largely predominant at hadron colliders, give multiple jets in the final state, with a cross section of $\mathcal{O}(100$ mb) and therefore it is overwhelming with respect to the $H \to b\bar{b}$ process whose cross section is of $\mathcal{O}(10$pb). The second

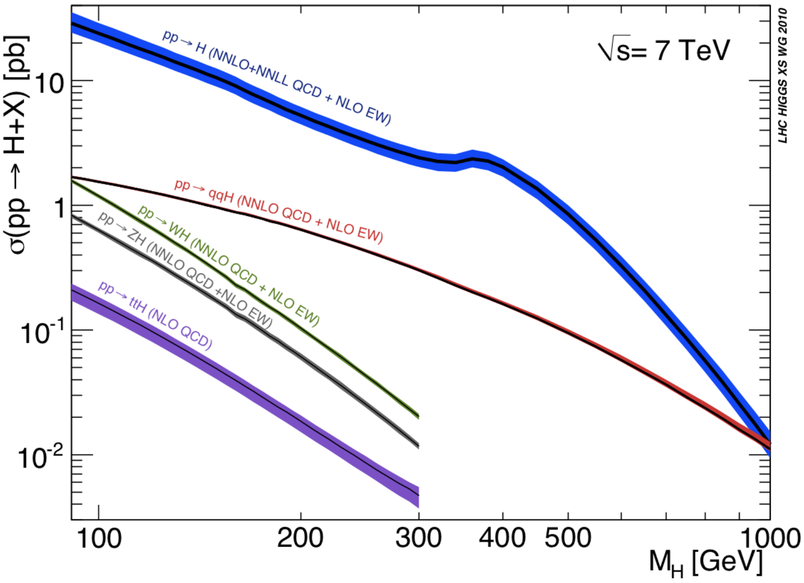

Figure 1.6. Higgs production mechanisms and their cross sections as a function of the Higgs boson mass at LHC for $\sqrt{s} = 7$ TeV

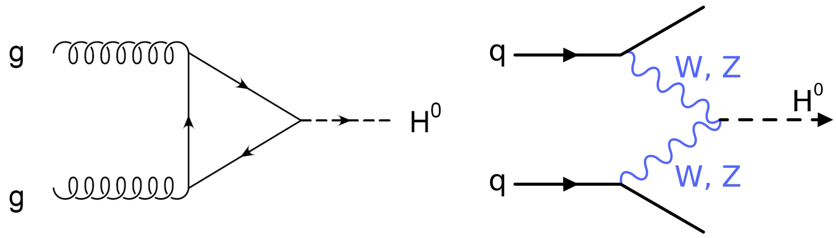

(a) (b)

Figure 1.7. Feynman's diagrams of the *gluon fusion* 1.7(a) and *vector boson fusion* 1.7(b) Higgs production mechanisms

decay channel in this mass region in terms of branching ratio is the $H \to WW^*$ process, in which one of the two W bosons is off mass shell because of the low mass of the Higgs boson. In general to reduce the background from QCD activity in an hadronic collider leptonic signatures are chosen, and for the $H \to WW^*$ process this means requiring at least one of the two W bosons to decay leptonically, thus generating a neutrino. This feature makes this measurement extremely challenging since the presence of the neutrino makes the final state not fully reconstructable, resulting in a very low resolution on the Higgs boson's mass and high background contamination. Given the above, the two most promising channels in the low Higgs boson mass regions are the $H \to \gamma\gamma$ and the $H \to ZZ^*$: The former benefits from the excellent invariant mass resolution that it is possible to achieve in order to distinguish the peak due to the tiny expected signal over a huge background with a smooth shape. Thanks to this feature the $H \to \gamma\gamma$ process can be considered one of the most important decay channels to be used for the Higgs search. The $H \to ZZ^*$

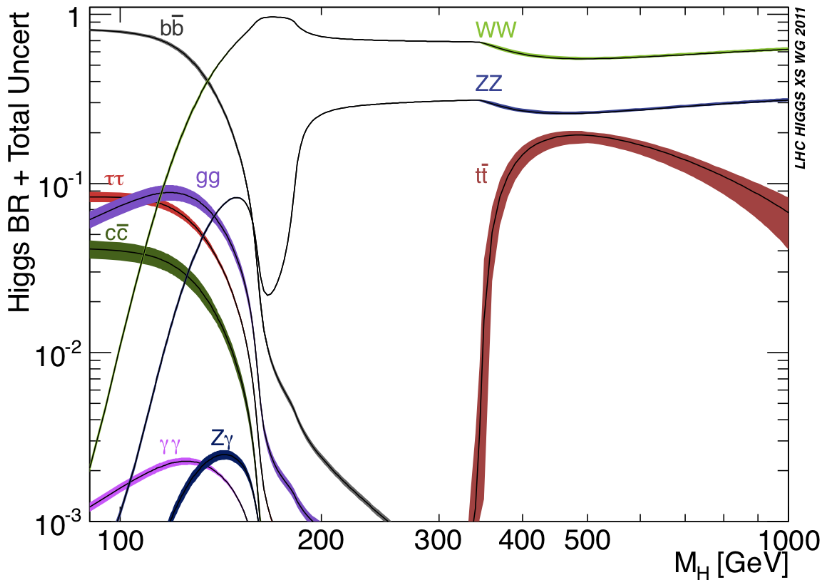

Figure 1.8. Higgs decay channels and branching ratios as a function of its mass

benefits of the possibility to fully reconstruct the final state. More details will be given on this final state in the next sections, but the $H \to ZZ^* \to \ell^+\ell^-\ell^+\ell^-$ is known to be the "gold-plated" channel for the Higgs boson search since it has very clean signature and very small background contribution, even if it is characterized by a tiny cross section.

At higher masses ($m_H > 160$ GeV/c^2) the decay to two vector bosons becomes dominant in both the $H \to W^+W^-$ and $H \to ZZ$ processes. In this mass region both the WW and the ZZ final states are vey important and are very powerful channels since raising the kinematic requirements on the final state particles the contribution from some of the background processes can be reduced without loosing acceptance on the signal process. As in the low mass region the $H \to WW$ suffers the presence of (at least) a neutrino in the final state, while the $H \to ZZ$ process benefits from the possibility of fully reconstructing of the final state. A detailed discussion of the final states available when studying the $H \to ZZ$ decay channel is given next.

1.5 The $H \to ZZ^{(*)} \to \ell^+\ell^-q\bar{q}$ Process

As already said in the previous section, the $H \to ZZ^{(*)}$ process is one of the dominant decay channel in a very wide mass range and it becomes dominant, together with the $H \to W^+W^-$ in the high-mass range ($m_H > 180$ GeV/c^2). The detection and the power of each Higgs boson decay channel depends also on the final state in which the intermediate bosons decay: as an example the fully leptonic decay modes $H \to W^+W^{-(*)} \to \ell^+\nu\ell^-\nu$ and $H \to ZZ^{(*)} \to \ell^+\ell^-\ell^+\ell^-$ (with $\ell = e, \mu$) are considered the most promising channels as their signature are easily reconstructable and the background contribution is very low. In particular the $H \to ZZ^{(*)} \to \ell^+\ell^-\ell^+\ell^-$ process is considered the "golden" channel for the Higgs discovery, since the decay chain is fully reconstructable with high precision and the background from the Standard Model processes giving the same final state is small ($\mathcal{O}$(10 pb)). This means that one can expect a very narrow signal peak over a small and smooth background distribution. However the purity and the precision of this channel have a drawback: the $H \to ZZ^{(*)} \to \ell^+\ell^-\ell^+\ell^-$ is very rare since it depends on the branching ratio of the two Z bosons to decay to muon or electron pairs, and the BR for the $Z \to \ell^+\ell^-$ process is 3.37% [19]. Therefore, despite of its mass, only a very little fraction of the produced Higgs bosons will decay to the $\ell^+\ell^-\ell^+\ell^-$ final state. In order to exploit the fully reconstructable final state offered by the $H \to ZZ^{(*)}$ process a different final state can be chosen: the highest branching ratio is given by the fully hadronic final state in which each Z boson decays to a $q\bar{q}$ pair ($BR(Z \to q\bar{q}) = 70\%$ [19]), but this process, as the $H \to b\bar{b}$ process discussed in the previous section, would be indistinguishable from the Standard Model background processes producing the same final state, such as QCD processes that are overwhelmingly more frequent at an hadron collider.

A compromise between the extreme purity but low statistics of the $H \to ZZ^{(*)} \to \ell^+\ell^-\ell^+\ell^-$ process and the high statistics but extremely high background contamination of the $H \to ZZ^{(*)} \to q\bar{q}q\bar{q}$ process is the "mixed" $H \to ZZ^{(*)} \to \ell^+\ell^-q\bar{q}$ channel: this process has a cross section about twenty times higher than the fully leptonic one, and the presence of a lepton pair originating from the Z boson in the final state reduces the sources of background. Even if this channel offers all these advantages, there is also some drawback: the resolution of the reconstruction of the four-momentum of a jet is not as good as what we can obtain for a lepton, and this reflects directly on the resolution that we can obtain on the Higgs signal. Moreover, even if the background contribution is not as high as in the fully hadronic final state, it is much higher than in the four lepton case, as jet production is much more frequent than lepton production in an hadronic collider. In particular any event with two opposite sign leptons and at least two jets in the final state will contribute to the background of this analysis.

The main contribution to the background is expected to derive from the Drell-Yan production of opposite sign lepton pairs in addition to jets: this process gives lepton pairs over all the mass spectrum (from few GeV/c^2 up to the Z boson peak and beyond) and the additional jets produced together with the leptons perfectly mimic the signal we are looking for. In addition, at the Z peak the Z+jets process has a production cross section of about 3 nb, that is about 10^4 times larger than the signal cross section.

Additional background comes from $t\bar{t}$ and single-t production: this can contribute in three ways to the background:

$$t\bar{t} \to (W^+ \to \ell^+\nu)b + (W^- \to \ell^-\bar{\nu})\bar{b}$$

$$tW^- \to (W^+ \to \ell^+\nu)b + \ell^-\bar{\nu} \qquad (+1 \text{ jet})$$

$$\bar{t}W^+ \to (W^- \to \ell^-\bar{\nu})\bar{b} + \ell^+\nu \qquad (+1 \text{ jet})$$

Even if the final state of these processes is the same as in the signal, in this case the dilepton invariant mass is not resonant, while in the signal it is resonant when looking for an high mass Higgs boson (and therefore the two Z bosons coming from its decay are both on mass shell). Therefore when looking for a low mass Higgs boson in this channel, an higher $t\bar{t}$ and single-t contribution to the background is expected.

A big contribution to the background comes also from QCD multijet events, in which leptons come from heavy flavor decay or from jets faking leptons in the detector. This background is expected to be small in the high Higgs mass region, but becomes important in the low mass range: the QCD fake rate, that is the probability of misidentifying a jet as a lepton, is higher at low-p_T(details on the reconstruction of the final state physics objects are given in chapter 3) and this leads to an higher contribution from QCD events to the final analysis sample. Moreover since in the $H \to ZZ^* \to \ell^+\ell^- q\bar{q}$ process one of the two Z boson produced in the Higgs boson decay is off mass-shell, the $Z^* \to \ell^+\ell^-$ process has to be taken into account, and, since the Z boson is virtual, no resonant peak is found in the dilepton mass distribution, thus making it harder to reject the QCD background.

Other background processes come from Standard Model diboson production (ZZ, WZ, WW) since the decay chain can produce two same flavor opposite sign leptons in addition to two high-p_T jets. These processes constitute a really irreducible background for two reasons: the $\ell^+\ell^- q\bar{q}$ final state can be obtained by means of two Z bosons exactly as in the signal process so this kind of event may have the same topology as the signal ones. Moreover the jet invariant mass resolution does not allow to distinguish between the $Z \to q\bar{q}$ and $W \to q\bar{q}'$ processes. However, despite the Standard Model diboson production is an irreducible background for this process, its very small cross section makes it a minor background.

The total background cross section is much higher than the signal one, and this leads to a very challenging search. However we can use some handles deriving from the features of the signal process: in the signal events the dijet system originates from a Z boson and therefore it has a resonant invariant mass. Being able to use this feature provides separation between signal and background.

Moreover we are looking for a tiny peak over a huge background shape so it is of crucial importance to understand all the background processes both in terms of shape and normalization in order to have a good description of the known processes and be ready for any new signal that could appear. In order to do this one can use the data in signal free regions in order to check if the understanding of the Standard Model processes is good.

In this thesis we will show the search of the Higgs boson in the $H \to ZZ^{(*)} \to \ell^+\ell^- q\bar{q}$, and we will demonstrate how it is possible to exploit the handles described above to reduce and control the backgrounds in order to achieve competitive results in such a challenging channel.

1.6 An Higgs-like particle has been discovered

As said in the previous section, this thesis is about the search for the Standard Model Higgs boson in the $\ell^+\ell^- q\bar{q}$ final state. This search is performed using the full 2011 dataset collected by the ATLAS experiment, while the 2012 data are not included (further details on this are given in chapter 2 and in section 6.4).

The astonishing performances of the Large Hadron Collider and the great work carried out by the physicists in both the ATLAS and CMS collaborations led to the discovery of a new particle, which seems to be compatible with the Higgs boson

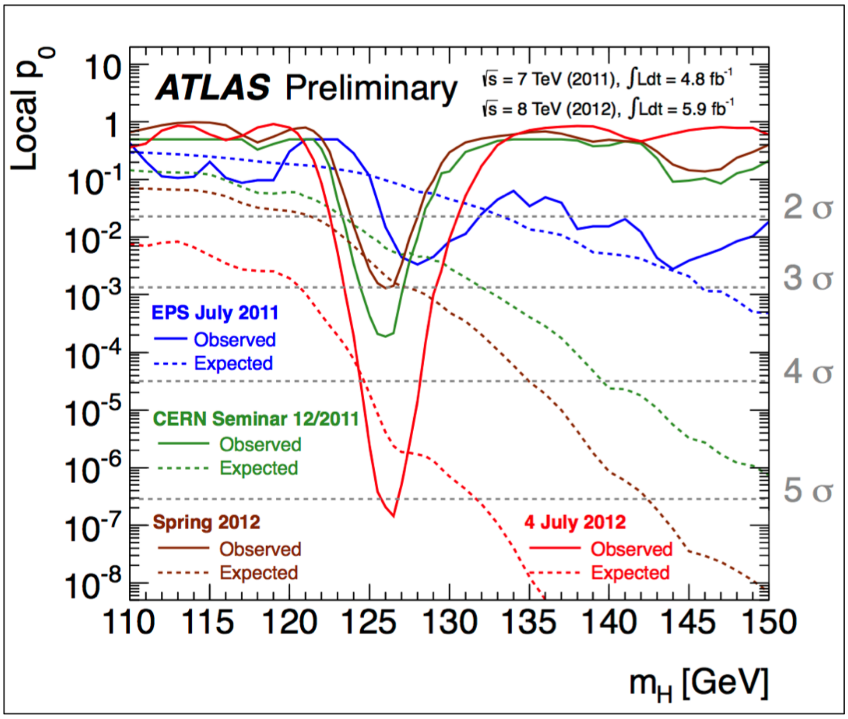

Figure 1.9. Evolution of the p-value measured in the combined Higgs boson search by the ATLAS experiment as a function of time. The dashed lines represent the expected results, while the solid lines represent the observed results. 2012 results include the full 2011 data sample combined with the amount of data collected in 2012 (at $\sqrt{s} = 8$ TeV) up to the closure for the reference public document.

introduced in section 1.2. The discovery of this new particle has been made public with a press conference held at CERN on July 4th 2012, and it is based on the analysis and the combination of both the 2011 and 2012 datasets, studied independently by the two collaborations. The decay channels which played a major role in this discovery are the $H \to ZZ^* \to \ell^+\ell^-\ell^+\ell^-$, the $H \to \gamma\gamma$ and the $H \to WW^* \to \ell\nu\ell\nu$ (this channel has been used only by CMS together with the $H \to b\bar{b}$ with associate production), and their combination showed a discrepancy between the data and the background-only hypothesis greater than 5σ, thus allowing to claim for a discovery. The new particle seems to be consistent with the Standard Model Higgs boson, which means that the measured production cross section and couplings are compatible with what expected from the mechanism explained in section 1.2.

Figure 1.9 shows the evolution of the p-value [59] of the combined Higgs search in the ATLAS experiment as a function of time (i.e. available integrated luminosity): the dashed lines stand for the expected p-value distributions while the solid lines represent the observed ones.

The p-value is basically the probability that, given a certain hypothesis (e.g. the background-only hypotesis), the data have fluctuations greater than the observed ones. The aim of such a measurement is to exclude at 5σ the background-only hypothesis.

From fig. 1.9 is is possible to see that with the full 2011 dataset combining the most powerful Higgs searches a p_0 between 3 and 4 σ's is reached. The study shown in this thesis started when the first hint of the Higgs excess was shown by ATLAS at the EPS conference in 2011 [20], that is the blue line in fig. 1.9, with the aim of extending for the first time in ATLAS the $H \to ZZ \to \ell^+\ell^- q\bar{q}$ search, usually performed in the $m_H > 200$ GeV/c^2 range, to the low mass region. This extension has been the first attempt of such an analysis within the ATLAS experiment, and it turned out that several innovation were needed in order to have a good result in this particular final state and mass region. Details about the new tools and techniques introduced in this study are given throughout the thesis.

The bulk of this analysis has been completed before the announcement given on July 4th 2012, and the results are under the approval procedure by the ATLAS collaboration in order to make them public.

Moreover the discovery of an Higgs-like particle does not represent an arrival point, but it is a starting point: we need to understand whether this new particle is the Standard Model Higgs boson, as theorized in mid-sixties or if it is something else. In order to understand this, the new particle has to be deeply studied in order to point out all its intrinsic features, which means also study all its possible final states.

Chapter 2

The Large Hadron Collider and the ATLAS Experiment

In this chapter the experimental apparatus used to measure the processes explained in the previous chapter is presented. The Large Hadron Collider is the particle collider which is operational at CERN since 2009. It collided protons at $\sqrt{s} = 7$ TeV in 2010 and 2011, while since March 2012 the center of mass energy has been raised to $\sqrt{s} = 8$ TeV. The data used in this thesis were collected in 2011 by the ATLAS detector, which is going to be explained in all its sub-components.

2.1 The Large Hadron Collider

The Large Hadron Collider (LHC) [21] is the largest and most energetic particle collider ever built. It is 27 *km* long and it is hosted in the same tunnel where the LEP collider was, about 100 meters underneath the Swiss-French national border near Geneva. It is a proton-proton (pp) collider, and the collision were delivered at $\sqrt{s} = 7$ TeV in 2010 and 2011, while they are being collected at $\sqrt{s} = 8$ TeV during 2012. One of the crucial parameters for the discovery power of a particle collider is the *instantaneous luminosity* since it is proportional to the event rate $\frac{dN}{dt}$:

$$\frac{dN}{dt} = \mathcal{L} \times \sigma \tag{2.1}$$

where σ is the cross section of the considered process. The instantaneous luminosity of a particle accelerator depends on its intrinsic features:

$$\mathcal{L} = \frac{N_p^2 f k}{4\pi R^2} \tag{2.2}$$

where N_p is the number of protons in each bunch, f is the revolution frequency of the protons in the accelerating ring, k is the number of bunches circulating in the beam and R is the mean radius of the proton distribution on the plane orthogonal to the beam direction. With formula 2.2 it is possible to understand the choice of colliding two protons beams instead of a proton and an antiproton beam: in principle $p\bar{p}$ collisions would be more convenient, since the valence quarks and anti quarks in the proton and the antiproton respectively can be exploited. When colliding protons with protons, instead, the interesting interactions come from the sea partons, and therefore the interaction cross section should be lower. This is not a real problem since at the energies reached by the LHC the cross sections of the two cases are similar for particles at the Electroweak scale. Moreover the use of antiprotons is very limited by their low production efficiency and the long accumulation time, that make very hard to produce an antiproton beam at the needed luminosity. The instantaneous luminosity delivered by the LHC in 2011 reached the value of $3.65 \times 10^{33}\ cm^{-2}s^{-1}$ (see fig. 2.1) at its maximum, where the design peak luminosity was $10^{34}\ cm^{-2}s^{-1}$. This high luminosity is reached with 1380 (2808 from the design) bunches per beam, each of them containing 10^{11} protons. The bunches have very small transverse spread, about 15μm in the transverse direction, and the longitudinal length is about 7 cm. In the design of the LHC the bunches should have crossed every 25 ns, giving a collision rate of 40 MHz, while the actual bunch spacing reached in 2011 and 2012 is of 50 ns. These parameters achieved in 2011 allowed an integrated luminosity of about 4.7 fb^{-1} collected in 2011 (see fig. 2.1).

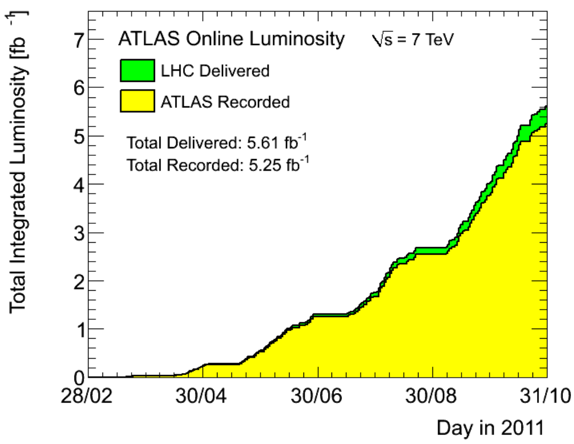

(a) Integrated luminosity recorded in 2011

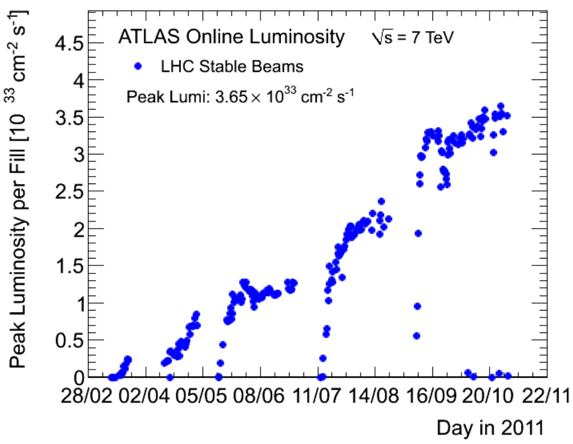

(b) Peak luminosity reached in 2011

Figure 2.1. The integrated luminosity as a function of time delivered by LHC (green) and recorded by ATLAS (yellow) in 2011 and the peak luminosity reached in 2011 run as a function of time

The high intensity of the proton beams gives rise to another important aspect to be taken in account: when the beam are intense there is the possibility to have more than one hard interaction per bunch crossing. This phenomenon is called *pile up*, and it strongly depends on the beam conditions (i.e. on the machine parameters), and may affect the data taking in many ways, as explained in section 4.1.2. As an example for the design machine parameters ($\sqrt{s} = 14$ TeV, $\mathcal{L} = 10^{34}$) the expected mean number of interaction per bunch crossing is ~ 23, while with the machine parameters of 2011 it is ~ 9, obtained with an instantaneous luminosity which is about a factor 10 lower.

The acceleration chain is showed in fig. 2.2: after their production, the protons are accelerated by the LINAC2 machine up to 50 MeV, then the Proton Synchrotron (PS) accelerates them up to 1.4 GeV and the Super Proton Synchrotron raises their energy up to 450 GeV before injecting them into the LHC. Into the LHC the protons are accelerated in the two opposite directions up to the colliding energy (3.5 TeV per beam).

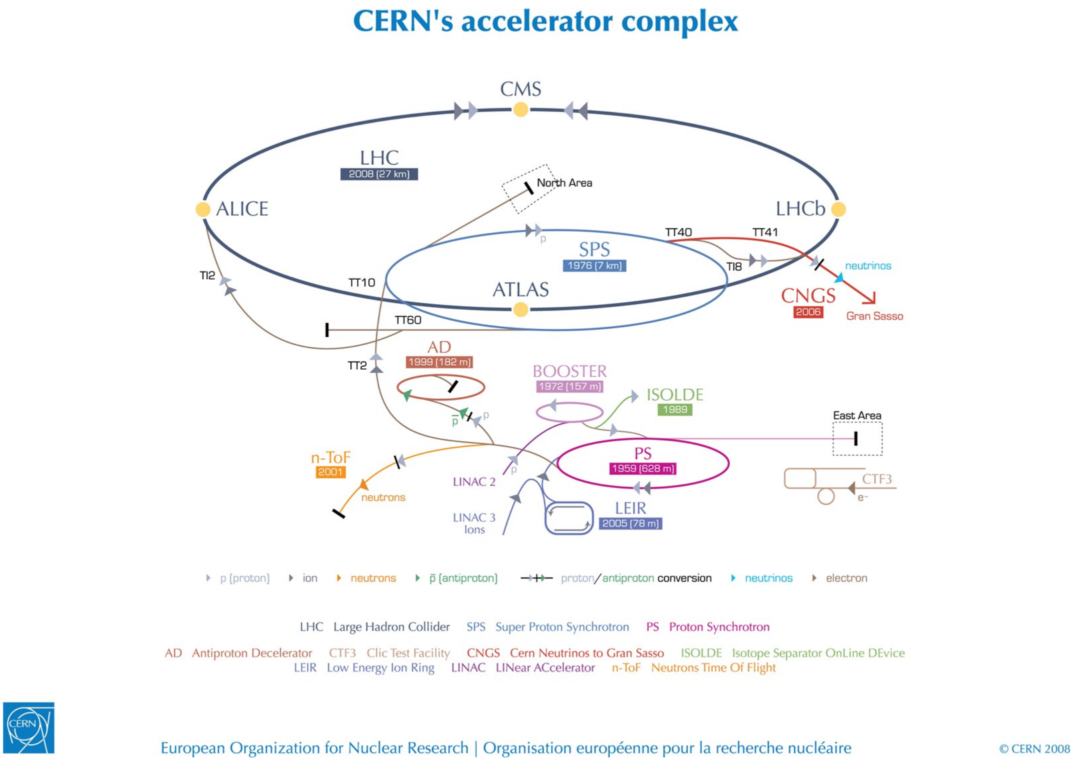

Figure 2.2. The CERN particles accelerators, in which it is possible to see the LHC injection chain: LINAC2, PS, SPS and LHC

Since LHC accelerates two beams of same sign particles, two separate accelerating cavities and two different magnetic fields are needed: LHC is equipped with 1232 superconducting magnets and 16 radiofrequency cavities which bend and accelerate the proton beams in the two parallel beam lines in the machine. The magnetic field used to bend such energetic proton beams is of 8.3 T and to reach such a magnetic fields the superconducting magnets are cooled down to 1.9 K and a 13 kA current circulates inside them.

The LHC provides collisions in four collision points along its circumference where

Feature	design value	actual value
beam energy [TeV]	7	4
bunch spacing [ns]	25	50
peak luminosity [$cm^{-2}s^{-1}$]	10^{34}	8×10^{33}
mean number of interaction per bunch crossing	23	20
number of buches	2808	1380
protons per bunch	1.15×10^{11}	1.67×10^{11}
bunch transverse dimentions [μm]	15	~ 30

Table 2.1. Main features of the LHC. The first column contains the values as in the LHC design, the second column contains the actual value of the features. The actual features include both 2011 and 2012 runs

detector experiments located: ALICE (*A Large Ion ColliderExperiment*), ATLAS (*A Toroidal Lhc ApparatuS*), CMS (*Compact Muon Solenoid*) and LHCb (*Large Hadron Collider beauty*). ATLAS and CMS are multi-purpose detectors, while ALICE and LHCb are focused on more specific studies: ALICE focuses on the quark-gluon plasma produced in heavy-ions collisions[1], while LHCb focuses on the study of CP violation processes occurring in b and c hadron decays.

2.2 The ATLAS Experiment

The ATLAS detector is one of the four main experiments recording the collisions provided by the LHC. It is 20 meters tall and 45 meters long and weights more than 7000 tons. It has the typical structure of a detector recording the collisions of a particle accelerator: it has a cylindrical shape centered at the interaction point with its axis along the beam line, and it is composed of several concentric subdeterctors which measure different features of the particles generated in the pp collision as they fly from the center of the detector to the outer part, as shown in fig. 2.4. From the innermost to the outermost layer, the ATLAS experiment is composed of (see fig. 2.3):

- an inner tracking system to detect charged particles and measure their momentum and direction;
- a solenoidal superconducting magnet providing a uniform magnetic field along the beam axis in which the inner detector is immerged;
- an electromagnetic calorimeter to measure the energy deposited by electrons and photons;
- an hadronic calorimeter to measure the energy deposited by hadrons;
- a muon spectrometer, that is a tracking system for the measurement of muons as they travel throughout all the detector and are the only particles reaching the outer part

[1] The LHC is able to accelerate and collide lead ions at $\sqrt{s} = 2.76$ TeV per nucleon, and ions collisions are foreseen each year in the LHC program. However this is not relevant for this thesis and no more details will be given.

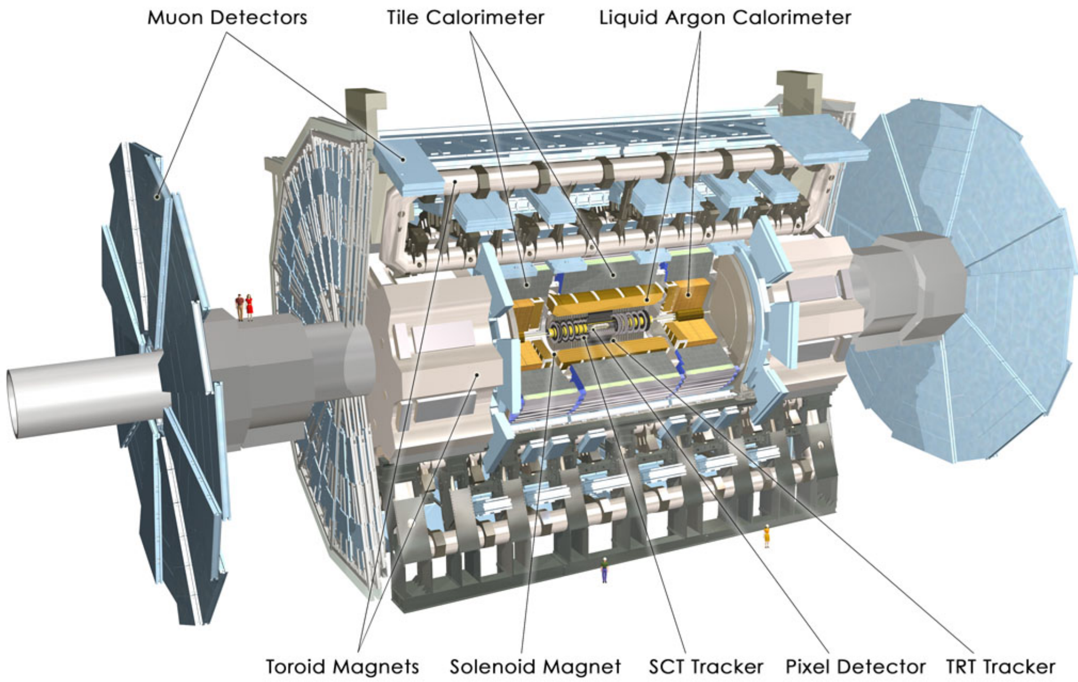

Figure 2.3. The ATLAS detector: all the subdetectors it is composed of are shown

- an air-cored superconducting toroidal magnet system which provide the magnetic field to the muon spectrometer

In the following sections details about the structure of the subdetectrors are be given, as well as some insight about how they work and their performances.

2.2.1 ATLAS Reference System

An important thing to define before starting with any specific information about ATLAS is the reference system used in this experiment, since it will be very important and many references to it will be made in the rest of this thesis. The ATLAS reference system in shown in fig. 2.5: the origin of the system is at the interaction point, the z axis is along the beam line and the $x - y$ plane is the plane perpendicular to the beam line. The x axis points to the center of the LHC ring, while the y axis goes upwards. The azimuthal angle ϕ is defined around the beam axis, while the polar angle θ is the angle from the z axis in the $y - z$ plane. The θ variable is not invariant under boosts along the z axis, and so instead of the θ angle the *pseudorapidity*[2] η is used:

$$\eta = -\ln\left[\tan\left(\frac{\theta}{2}\right)\right] \tag{2.3}$$

The relation between η and θ is shown in fig. 2.6.

Since at an hadronic collider the real colliding particles are the partons inside the protons, we can say that the actual center of mass energy in unknown in each

[2]Actually the real boost-invariant variable is the *rapidity* y: $y = \frac{1}{2}\ln\frac{E+p\cos\theta}{E-p\cos\theta}$. In the ultra-relativistic limit the rapidity y can be substituted with the pseudorapidity η

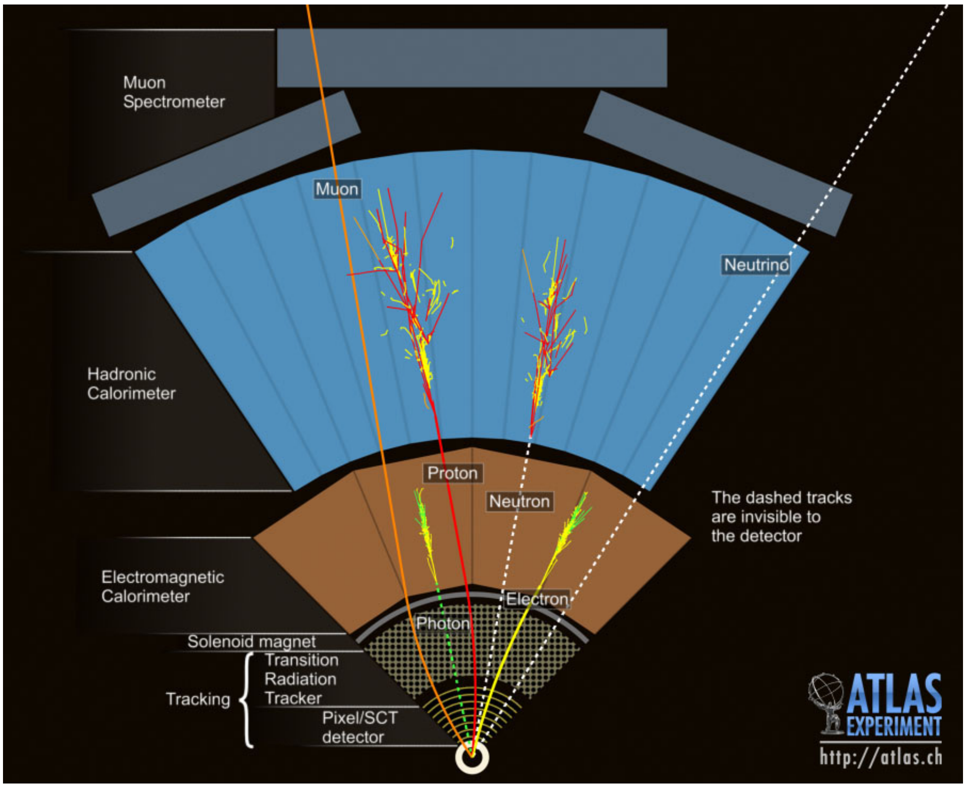

Figure 2.4. Schema of the detection of the particles produced in a proton collision while they travel through the several layers of the ATLAS detector

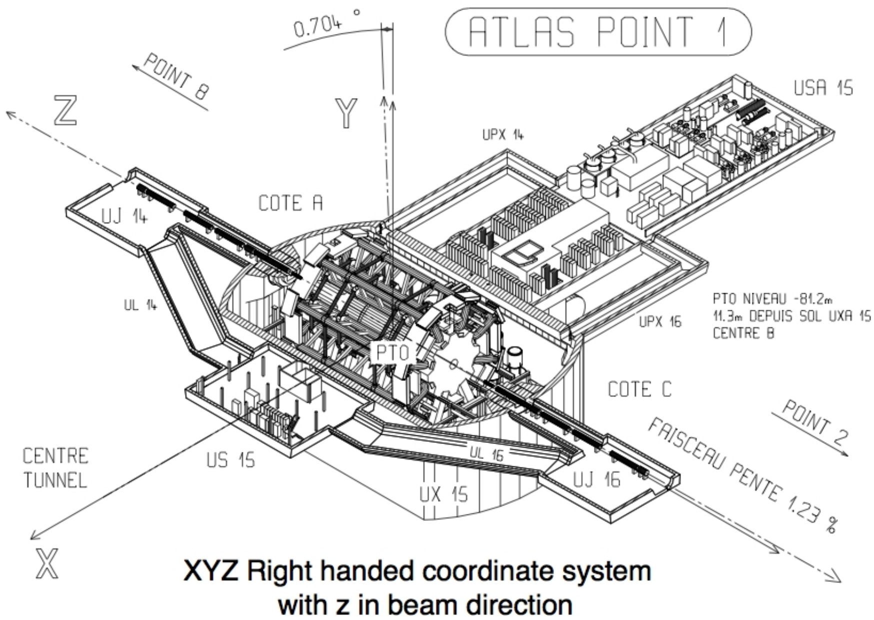

Figure 2.5. Reference system used in ATLAS

collision: $\hat{s} = x_1 \cdot x_2 \cdot s$, where $\hat{s}$ is the effective collision energy, x_1 and x_2 are the

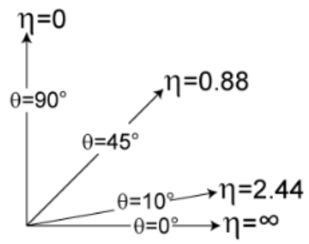

Figure 2.6. The relation between the pseudorapidity η and the polar angle θ

fractions of momentum carried by the two collinding partons and s is the colliding energy of the two protons. Because of this, the total momentum along the beam axis before the collision is unknown, while the total momentum in the transverse plane (i.e. the $x-y$ plane) is known to be zero (the Fermi momentum of the partons inside the proton is negligible with respect to the longitudinal momentum due to the acceleration), and hence we can apply the momentum and energy conservation laws only on the transverse plane (because we know what is the initial total momentum). For this reason from now on, we will consider only transverse quantities, and they will be denoted with the "T" sub-script (e.g. p_T stands for transverse momentum, that is the projection of the momentum on the $x-y$ plane).

2.2.2 ATLAS Magnets

The ATLAS detector is equipped with two magnetic systems: a superconducting solenoid [22], providing a magnetic field to the inner tracking system, and a system of air-core superconducting toroidal magnets [23, 24] located in the outer part of the detector as shown in fig. 2.7.

The solenoid covers the central region region of the detector, provides an uniform magnetic field of approximately 2 T along the z axis bending particles' tracks in the transverse plane in order to let the inner tracking system measure their transverse momentum. The solenoid is located between the inner detector and the electromagnetic calorimeter and its dimensions (its width, particularly) have been optimized in order to minimize the amount of dead material (only 0.83 radiation lengths) in front of the calorimetric system.

The toroid is one of the peculiarities of the ATLAS detector: it is located outside of the calorimetric system covers the region $|\eta| < 3$ (considering all its subparts), and provides a magnetic field whose peak intensities are 3.9 T in the central region of the detector and 4.1 T in the forward region. The aim of such a toroid is to have a large lever arm to improve the measurement of the muon transverse momentum (more details in section 2.2.5), and it is built "in air" in order to minimize the muon multiple scattering within the detector.

The ATLAS double magnetic system has been designed to provide two independent measurements of the muon transverse momentum in the inner detector and in the muon spectrometer, thus ensuring good muon momentum resolution from few GeV up to the TeV scale.

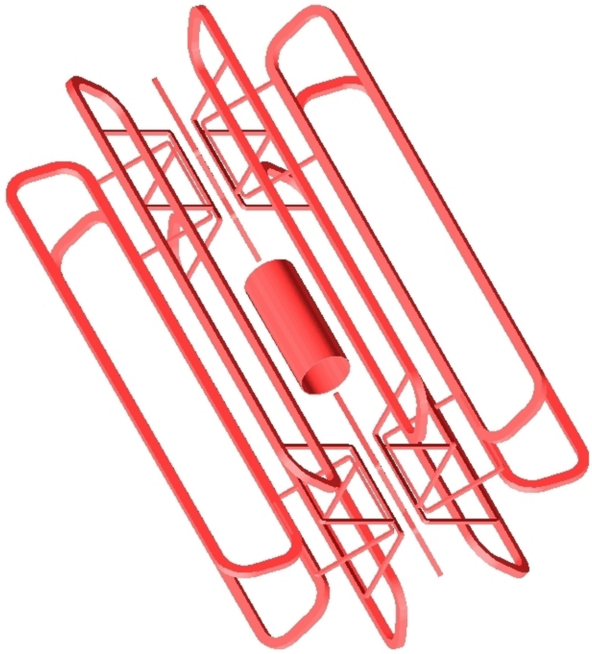

Figure 2.7. The magnetic system of the ATLAS detector: the inner cylinder is the superconducting solenoid, while the external parts are the coils of the toroid

2.2.3 The Inner Detector

The ATLAS Inner Detector tracker (ID), shown in fig. 2.8, is composed by three concentric cylindrical subdetectors. Its axis is centered on the z axis and it is approximately 6 meters long and its diameter 2.30 meters, covering the region ($|\eta| < 2.5$). The three detector composing the ID are:

- **Pixel Detector:** it is composed of three layers of silicon pixels. It provides high-precision track measurement, since the spatial resolution on the single hit is ~ 10 μm in the ϕ coordinate and ~ 115 μm along the z coordinate.
- **Semiconductor Tracker (SCT):** it is the second high-precision detector of the ATLAS inner tracker. It is composed of eight layers of silicon strips with a spatial resolution on the single hit of 17 μm in ϕ and 580 μm along z. The Pixel Detector and the Semiconductor Tracker together provide on average eight high-precision hits per track.
- **Trasition Radiation Tracker (TRT):** it is composed of straw tubes chambers. The resolution of such a detector is lower than the previous one (~ 130 μm per straw), but it is compensated by the high number of points per track (36 on average) that it can provide.

Figure 2.9 shows the number of hits left by the charged tracks in the three inner subdetectors as a function of η.

The aim of the ATLAS ID is to measure the tracks of the charged particles produced in the pp collision and all the related features: p_T, η, ϕ, the eventual

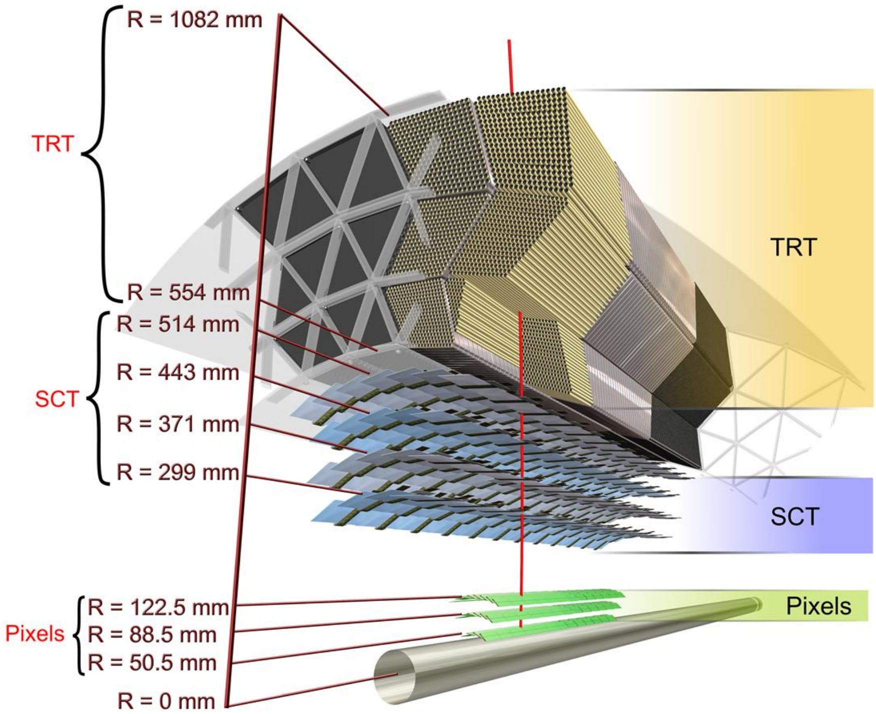

Figure 2.8. The ATLAS Inner Detector tracker: the three subdetectors (the Pixel Detector, the Semiconductor Tracker and the Transition Radiation Tracker) are shown as well as their radial dimensions

secondary vertexes due to long-lived particles. The momentum is measured by measuring the track curvature in the magnetic field provided by the superconducting solenoid described in sec. 2.2.2. To estimate the expected resolution the *sagitta method* can be used: the magnetic field bends the trajectory of the charged particles in the ϕ coordinate because of Lorentz's force:

$$\vec{F}_L = q\vec{v} \times \vec{B} \tag{2.4}$$

where q is the charge of the particle, $\vec{v}$ is its velocity and $\vec{B}$ is the magnetic field. The resolution of the momentum measurement depends on many detector-related parameters:

$$\frac{\Delta p}{p^2} = \frac{8}{0.3 \cdot B \cdot L^2}\Delta s \tag{2.5}$$

where B is the magnetic field expressed in Tesla, L is the lenght of the reconstructed track expressed in meters, while Δs is (see fig. 2.10):

$$\Delta s = \frac{\epsilon}{8}\sqrt{\frac{720}{N+4}} \tag{2.6}$$

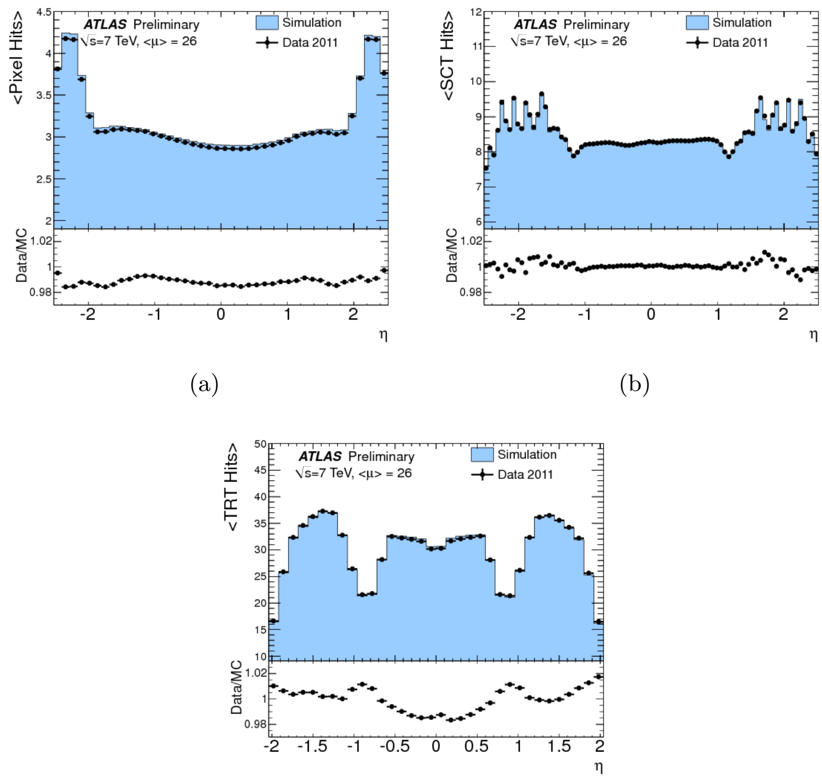

(a) (b)

(c)

Figure 2.9. Number of hits recorded in the ID as a function of the η of the track. 2.9(a) shows the Pixel detector, 2.9(b) shows the SCT and 2.9(c) shows the TRT

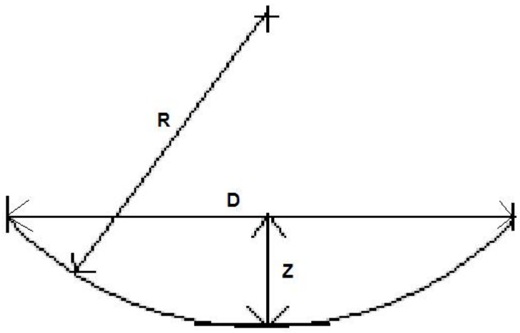

Figure 2.10. The sagitta of a track is the maximum distance between the track itself (that is an arc of a circle) and the straight segment having the same starting and ending points

where N is the number of measured points on the track and ϵ is the resolution on the measurement of the points. From formulas 2.6 and 2.5 it is possible to see how it is crucial to have a strong magnetic filed, an high number of points per track and a good spatial resolution on these points in order to have a good resolution on the track p_T.

The performance of the ID are shown in the next chapter, where also the tracking algorithm are explained.

2.2.4 The Calorimetric System

In an high-energy physics experiment the calorimeters are used to measure the energy of photons, electrons (the electromagnetic calorimeter), hadronic jets (hadronic calorimeter) and the missing E_T (due to undetected particles like neutrinos) which is measured thanks to the tightness of the calorimetric system. The ATLAS calorimeter has a cylindrical shape centered around the interaction point with its axis lying on the ATLAS z axis. It is long about 13 meters and the external radii of the electromagnetic and hadronic calorimeters are 2.25 and 4.25 meters respectively. The ATLAS calorimeters are represented in fig. 2.11 and the absorption lengths as a function of η are shown in fig. 2.12.

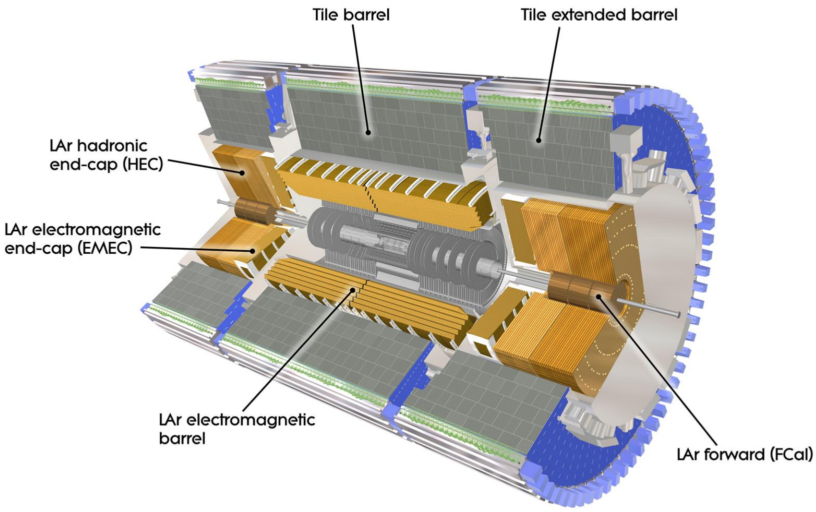

Figure 2.11. The ATLAS calorimetric system: the electromagnetic calorimeter made of liquid Argon and Lead and the hadronic caloimeter, whose composition varies as a function of η

The Electromagnetic Calorimeter

The Electromagnetic Calorimeter of the ATLAS experiment covers the region up to $|\eta| < 3.2$. The structure of the Electromagnetic Calorimeter is very peculiar (see fig. 2.13): it has an accordion structure made of lead (whose thickness varies as a function of η in order to maximise the energy resolution) which is immersed in liquid Argon, which is the active material of the calorimeter. This structure confers to the calorimeter very high acceptance and symmetry in the ϕ coordinate. In the central region $|\eta| < 2.5$ the radial coordinate the electromagnetic calorimeter has three sampling channels in order to maximize particle identification power (see fig. 2.13). The calorimeter is segmented in cells of variable dimensions as a function of η as well as its thickness ($> 24X_0$ in the central region and $> 26X_0$ in the forward region): in the central region the segmentation is $\Delta\eta \times \Delta\phi = 0.025 \times 0.025$.

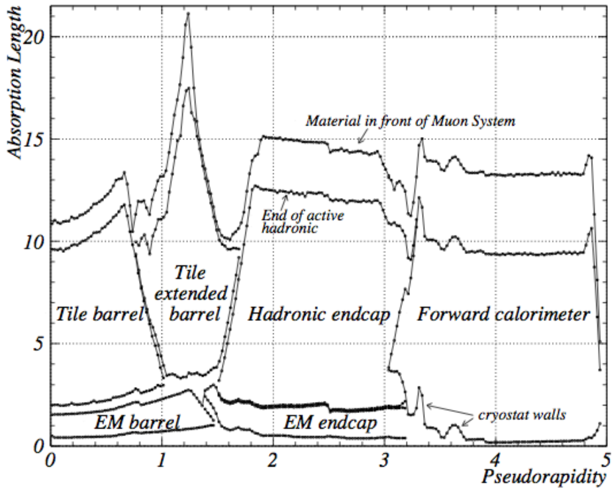

Figure 2.12. Amount of material in terms of absorption length in the ATLAS calorimetric system as a function of η

The ATLAS EM calorimeter energy resolution is parametized as

$$\frac{\Delta E}{E} = \frac{10\%}{\sqrt{E[\text{GeV}]}} \oplus 1\% \tag{2.7}$$

where 10% si the sampling term and 1% is the constant (intercalibration) term. The η resolution is:

$$\frac{40\text{mrad}}{\sqrt{E[\text{GeV}]}} \tag{2.8}$$

Figure 2.14 shows the reconstructed invariant mass of photon pairs collected with the ATLAS electromagnetic calorimeter. The resolution on the π^0 peak is extracted from the fit and it is 24 MeV.

The Hadronic Calorimeter

The Hadronic Calorimeter covers the region $|\eta| < 4.5$, and it is realized with a variety of techniques as a function of η (see fig. 2.11). The central region ($|\eta| < 1.7$) it is made of alternating layers of iron (used as absorber) and scintillating tiles as active material, and its thickness offers about 10 interactions lengths λ at $\eta = 0$. It is segmented in $\Delta\eta \times \Delta\phi = 0.1 \times 0.1$ pseudo-projective towers pointing to the interaction point.

The "endcap" region ($1.7 < |\eta| < 3.1$) is equipped with a liquid Argon and lead, as the Electromagnetic calorimeter, while the forward region ($3.1 < |\eta| < 4.5$) is equipped with liquid Argon, but the accordion structure is replaced by a concentric rods and tubes made of copper. This variety of materials and structures is due to the different radiation hardness required in the different parts of the detector.

2.2.5 The Muon Spectrometer

The ATLAS Muon Spectrometer is shown in fig. 2.15. It is instrumented with both trigger and high-precision chambers immersed in the magnetic field provided by the

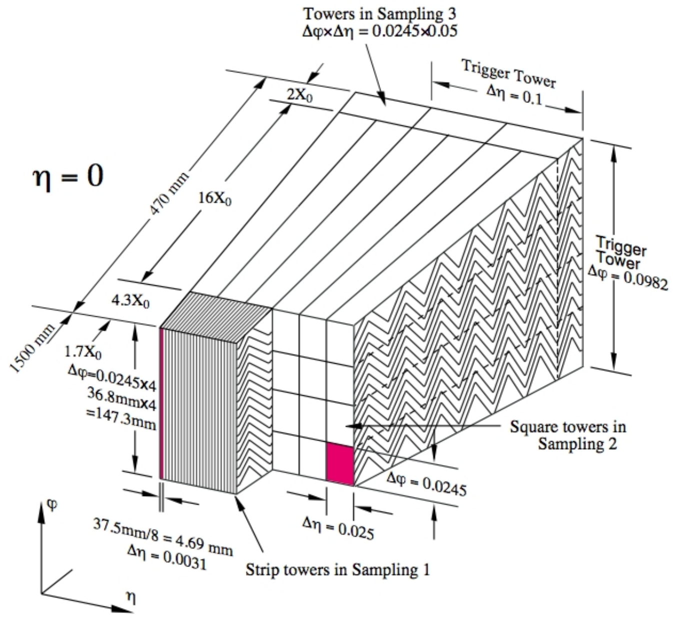

Figure 2.13. The accordion structure of the electromagnetic calorimeter and its radial segmentation

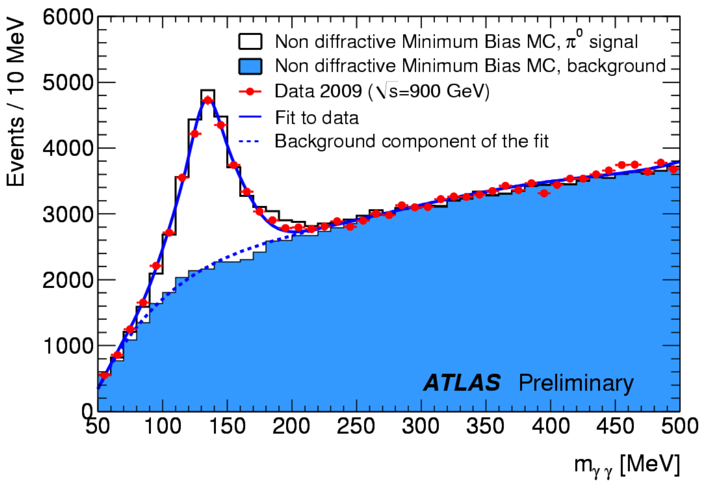

Figure 2.14. The reconstructed $\pi^0 \to \gamma\gamma$ decay is a good indicator of the performance of an electromagnetic calorimeter

toroidal magnets (sec. 2.2.2) which bends the particles along the η coordinate, and it allows to measure the muons p_T in the region $|\eta| < 2.7$ using the sagitta method described in section 2.2.3. Here the lenght of the lever arm plays a leading role on the p_T resolution. The chambers used to reconstruct the muon track are of several types depending on the η region, in order to face the different rate conditions present in the different parts of the detector. In the central region ($|\eta| < 2$) Monitored Drift Tubes (MDTs) are used. The MTD chambers are composed of aluminium tubes of 30 mm diameter and 400 μm thickness, with a 50 μm diameter central wire. The tubes are filled with a mixture of Argon and CO_2 at high pressure (3 bars), and

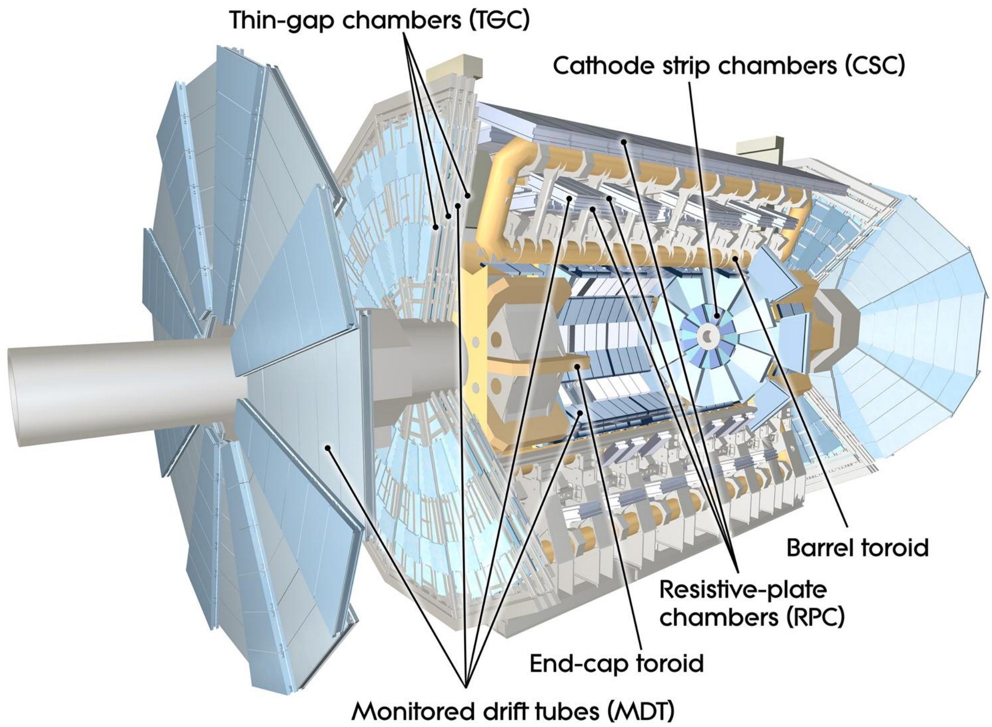

Figure 2.15. The ATLAS muon spectrometer

each tube has a spatial resolution of 80 μm.

At higher pseudo-rapidity ($2 < |\eta| < 2.7$) the higher granularity Cathode Strip Chambers (CSC) are used. CSC chambers are multiwire proportional chambers in which the readout is performed using strips forming a grid on the cathode plane in both orthogonal and parallel direction with respect to the wire. The spatial resolution of the CSC is about 60 μm.

As shown in fig. 2.15, in the central region the Muon Spectrometer is arranged on a three layer (or stations) cylindrical structure which radii are 5, 7.5 and 10 meters; while in the forward region the detectors are arranged vertically, forming four disks at 7, 10, 14 and $21-23$ meters from the interaction point.

The other chambers installed on the spectrometer are used for the trigger (see next section for details). The chambers used for the muon trigger are Resistive Plate Chambers (RPC) in the central region ($|\eta| < 1.05$) and Thin Gas Chambers (TGC) in the forward region. These detectors provide very high time resolution ($\mathcal{O}$(ns)) even if the spatial resolution is not so high ($\mathcal{O}$(cm)).

2.2.6 The ATLAS Trigger

The LHC is designed to provide collisions at a frequency of $40MHz$ and, since the average dimension of an ATLAS event is ~ 1.5 MB, a recording rate of ~ 60 TB per second would be needed, while the current technology allows to record data at about 300 MB/s. This is not a huge problem, since the interesting physics at LHC does not occurs at that rate but at lower ones, as shown in fig. 2.16, so the events to be recorded can be selected without loosing the relevant informations. This selection

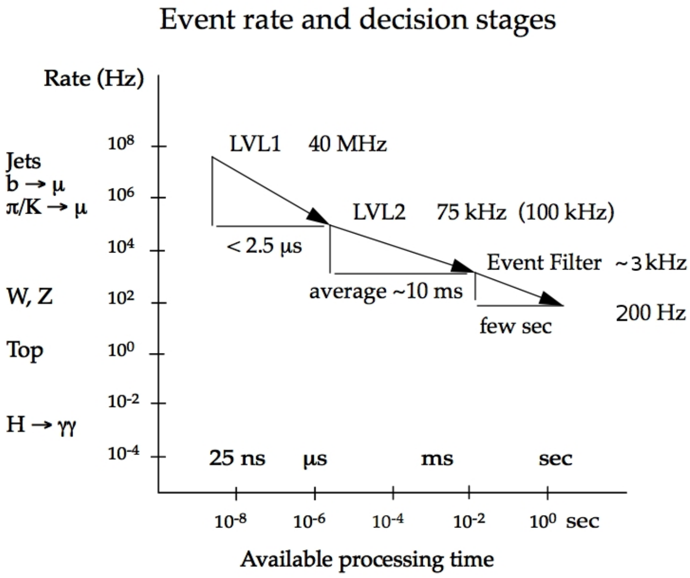

Figure 2.16. The event rate at which interesting physics occur (referred to LHC design parameters) and the processing time of each trigger level

is performed online by the ATLAS trigger and data acquisition system [25]. The ATLAS trigger is designed to rapidly inspect the events detected by the ATLAS detector and choose whether record or discard the event after having compared its main features with a set of predefined thresholds contained in the trigger menu.

The ATLAS trigger system has a three level structure: each level refines the measurements of the previous level introducing also new selection criteria and combining the information from different subdetectors, as shown in fig. 2.17.

The first level of the ATLAS trigger (L1 or LVL1) is completely hardware-based and it makes use of only the data collected by the calorimetric system and the muon spectrometer: the L1 trigger only looks for high-p_T muons candidates or calorimetric objects (electrons/photons, jets) by means of fast and rough measurements performed by ad-hoc detectors in the Muon Spectrometer (RPC, TGC) and simplified object identification in the calorimeter. The L1 is designed to take a decision on the event in 2.5 μs and its output is a list of so-called *Regions of Interest* (RoI), which are $\eta - \phi$ regions of the detector in which interesting activity has been detected, and the output rate is about $100 kHz$.

The second level of the ATLAS trigger (L2 or LVL2) is completely software-based. It takes as input the RoIs provided by the L1, and refines the measurement into these regions: data of the precision chambers are used in the Muon Spectrometer (MDT, CSC) as well as the data from the ID, while the measurement of the calorimetric objects is refined using higher level algorithms. Moreover the data of the different subdetectors are combined together in order to obtained better object reconstruction/identification (e.g. the ID and the MS tracks are combined for the muons, ID and calorimetric informations are combined to discriminate between electrons and photons). The L2 takes its decision in $\mathcal{O}$(10ms) and its output rate is about 3 kHz.

The third level of the ATLAS trigger (Event Filter, EF) is completely software-based and forms, together with the L2, the High Level Trigger (HLT). At this stage

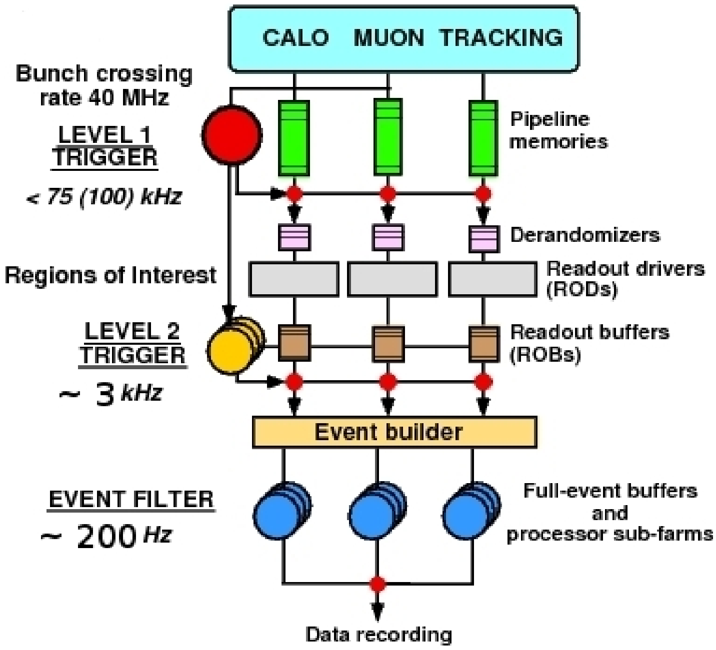

Figure 2.17. Main structure of the ATLAS trigger system: it is made of three levels, each improving the measurement of the previous levels also combining informations from different subdetectors

a full reconstruction of the detector is performed (the measurement is not restricted to the RoIs), and the algorithms run at the EF are mostly the offline reconstruction algorithms adapted to the online environment. The decision of the EF is taken in $\mathcal{O}(1\text{s})$ and the output rate is about 400 Hz. Figure 2.18 shows the total trigger

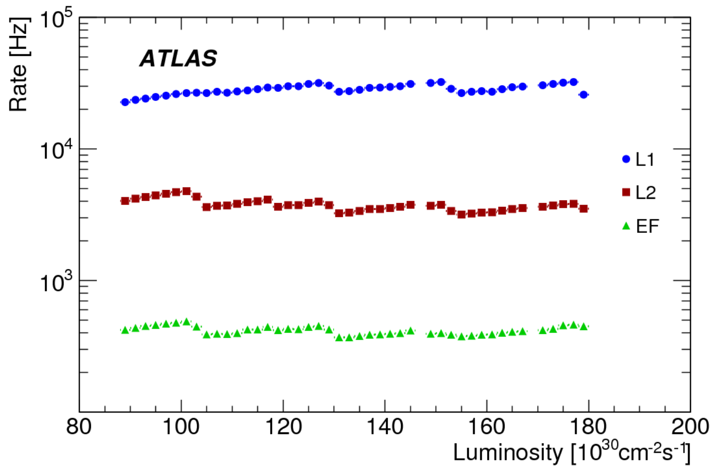

Figure 2.18. Total trigger rates at each level of the ATLAS trigger

rate for all the three levels as a function of the instantaneous luminosity: how can be seen the trigger rates are kept stable. This happens thanks to changes in the prescales and in the trigger menu, where higher thresholds or quality criteria on the

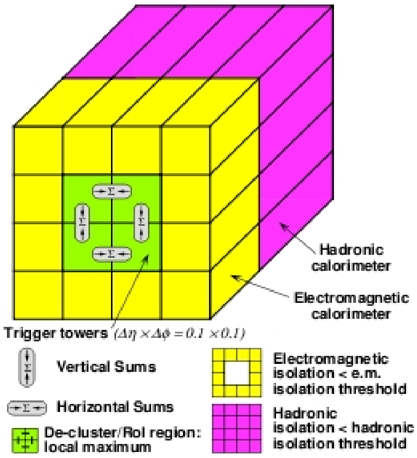

Figure 2.19. The L1 trigger for calorimetric objects in the Electromagnetic calorimeter: the green area represents the RoI cluster, the yellow area is the region used for the isolation requirements, and the pink area is the region used for the hadronic isolation

trigger objects are required as the luminosity increases.

Since the analysis presented is this thesis relies on data selected with triggers requiring the presence of leptons, more details are given about electrons and muons triggers in the following sections.

Electron Trigger

The electron trigger follows the three level ATLAS trigger structure, in which the measurements and the selections are refined at each stage.

At the first level the electron trigger makes use only of the calorimeters, and hence no distinction between electrons and photons is possible since they are both identified as "calorimetric objects". In particular the L1 trigger measurement is a real calorimetric measurement even if it is done with reduced granularity (see fig. 2.19): once a relevant amount of energy is detected, the total energy in a little 2×2 cluster is measured (green area), and the isolation with respect to electromagnetic (yellow area) and hadronic activity (pink area, e.g. due to electrons coming from heavy quark decay) is computed. If the these three parameters (E_T, electromagnetic and hadronic isolation) fulfil the requirements, then the electromagnetic calorimeter is accepted as a good calorimetric object and its RoI is propagated to the L2.

The L2 trigger basically refines the calorimetric measurement, accessing the full granularity of the calorimeters and studying the shape of the energy deposit (e.g. π^0/γ separation), and includes the data of the inner tracking system. At this level a "calorimetric object" may become an electron if an ID track consistent with it is found. Since the measurements are more precise at this level, tighter conditions on the quality and the kinematic features of the electron candidates can be required.

At the end of the chain the EF further refines the measurements performed at the L2 on the electron candidates, running algorithms very similar to the offline ones and having access to the data of all the subdetectors with full granularity.

Figure 2.20 shows the distribution of the difference between the offline and the

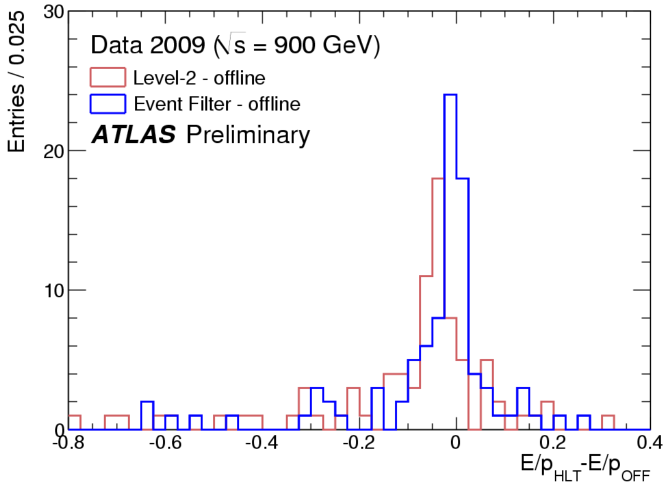

Figure 2.20. E/p distribution found by the HLT and the offline for the electron trigger. The distributions are shown for L2 and EF separately

value measured at different trigger levels of the E/p variables for electrons. This shows how the EF measurement (blue line) is better than the L2 measurement (red line), since the former is allowed to use reconstruction algorithms very similar to the offline ones thanks to the large processing time available (see fig. 2.16), while the latter has to rely on simplified algorithms.

Muon Trigger

The L1 muon trigger relies on the temporal and geometric correlation of the hits left by a muon on the different layers of RPC detectors installed in the muon spectrometer, as shown in fig. 2.21. When a muon coming from the interaction point crosses the RPC detectors, it leaves hits on each of them: starting from the hit on the central station (also known as *pivot* plane, RPC2 in fig. 2.21) a "correlation window" (several windows are opened for several p_T thresholds) is opened on the RPC1 layer. If a good hit (i.e. hits in both η and ϕ and in time with the hit on the pivot plane) is found on the RPC1 layer then a low-p_T muon candidate is found. The same algorithm is applied using the RPC3 plane to look for high-p_T muon candidates. Once a muon candidate is found, the RoI is propagated to the L2.

At the L2 the muon track is reconstructed for the first time: there are algorithms which reconstruct the muon tracks in the ID and in the MS separately and then combine them in order to determine of p_T, η and phi. At this level the p_T measurement is not done by a fit, but *look-up tables* are used: the p_T estimation is done starting from the relation

$$\frac{1}{s} = A_0 \cdot p_T + A_1 \tag{2.9}$$

where s is the sagitta of the muon track and A_0 and A_1 are two constant values needed to take into account the magnetic field and the energy loss in the calorimeters respectively. A look-up table is basically a table whose columns and rows represent the $\eta - \phi$ segmentation of the ATLAS detector, and in each cell a (A_0, A_1) pair is

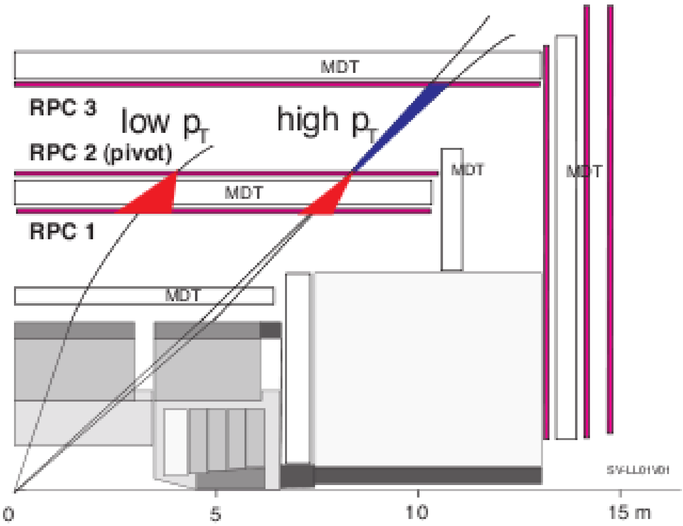

Figure 2.21. L1 muon trigger algorithm: a muon coming from the interaction point leaves hits on the three layers of RPC detectors installed in the muon spectrometer. The position of the different hits is correlated as a function of the muon p_T

contained. For each muon candidate, given η, ϕ and s, a fast estimation of the p_T is possible. This method is used since at the L2 there is not enough time to perform a real fit to precisely measure the track p_T. Once the full track is reconstructed (from the ID to the MS), the calorimetric activity around it is measured, in order to apply the isolation requirements.

At the EF the muon reconstruction algorithms perform again the operations performed by the L2 algorithms, but now the full detector with its full granularity can be accessed, and a real fit of the muon track is performed.

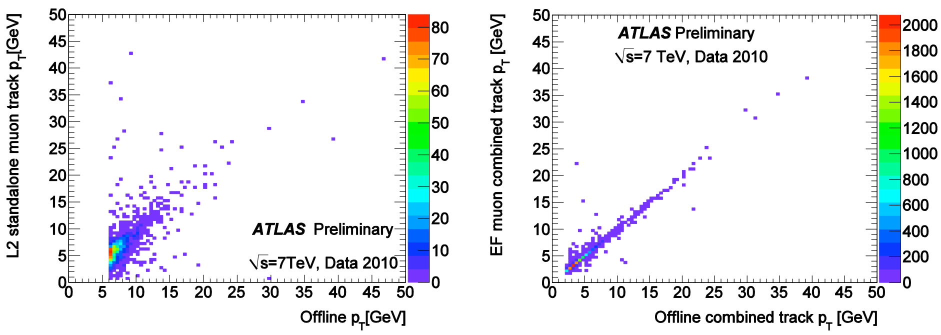

(a) (b)

Figure 2.22. Correlation between the muon p_T reconstructed at several trigger levels (level 2 in 2.22(a) and event filter in 2.22(b)) and the offline reconstruction

Figure 5.8(a) shows the correlation between the muon p_T reconstructed at different trigger levels and the offline reconstruction: in fig. 2.22(a) the correlation between the L2 stand alone p_T is shown, while in fig. 2.22(b) the correlation between the EF combined p_T measurement and the offline one is shown. As can be seen the

EF measurement is much more accurate and precise compared to the one performed at L2. The corresponding plot for L1 is not shown since at L1 the muon p_T is not really measured, but, as explained above, only a threshold is available.

Chapter 3

Reconstruction

The analysis presented in this thesis relies on the identification and reconstruction of electrons, muons, jets and b-jets produced in the pp collision provided by LHC and collected by the ATLAS detector. In this chapter general reconstruction criteria and algorithms used in ATLAS are presented, while specific selection criteria to select the physical objects used in this thesis are shown in sections 5.2 and 5.3.

3.1 Track Reconstruction

The track reconstruction [26] in ATLAS makes use of information collected by the Pixel, SCT and TRT subdetectors described in section 2.2.3. The tracking algorithm foresees two different stages:

- *Pre-processing*: the raw data from the three subdetectors are converted in three kind of data, depending on the subdetector: clusters for the Pixels, space-points for the SCT and calibrated drift circles for the TRT.

- *Track finding*: different algorithms are used at this stage. The default one finds track seed combining space-points in the three pixel layers and in the first SCT layer. These seeds are extended to all the SCT layers (see fig. 3.1) to form a track candidate. The selected track candidates are then extended to the TRT and refitted using the full ID information. If some TRT hit worsening the fit quality is found, this is not included in the final fit, but is kept and labelled as *outlier* for offline studies.

The track reconstruction performances on data have been measured first using test beam [27] and cosmic rays [28], and further studies have been carried out with the pp collision [29]: beside the distribution of hits in each subdetector of the ID shown in figure 2.9, figure 3.2(a) shows the data-Monte Carlo (data taken at $\sqrt{s} = 7$ TeV) comparison for the reconstruction of the d_0 variable, that is the distance od minimum approach of a track to the primary vertex in the transverse plane, while fig. 3.2(b) shows the data-Monte Carlo comparison for the longitudinal impact parameter z_0 multiplied by the sine of the polar angle θ. The striking agreement between data and MC distributions highlights the very good understanding of the ID material and efficiencies, of the track reconstruction and its very good performances.

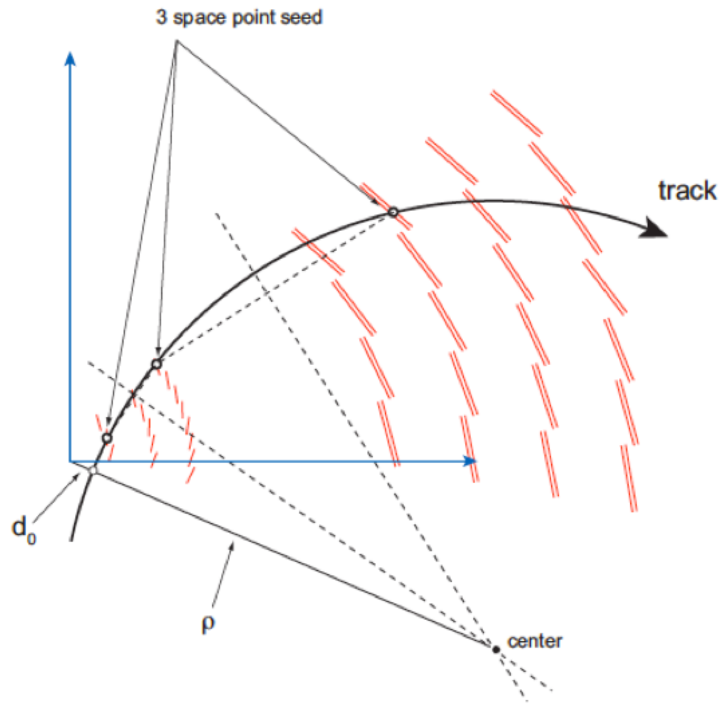

Figure 3.1. Schematic representation of the ID track reconstruction in ATLAS

3.2 Muon Reconstruction

The reconstruction of muons relies on informations coming from the MS, the ID and the calorimeters. Its aim is to reconstruct muons with high efficiency in a wide p_T spectrum (from few GeV to the TeV scale). In ATLAS four muon categories are used, each optimized for a different need:

- *Stand-Alone Muons*: to build Stand-Alone (SA) muons only the informations collected by the MS are used: the hits left in the three MDT stations are combined to form three segments, and the three segments are used as input to a fitter to reconstruct the track. Once the track is reconstructed it is back-extrapolated to the interaction point taking into account the energy loss in the calorimeter by means of a parametrization. The SA muons are reconstructed in a wide η region ($|\eta| < 2.7$), but suffer of the spectrometer inefficient regions at $\eta = 0$ and $\eta \sim 1.2$.

- *Combined Muons*: Combined (CB) muons are obtained combining SA muons with an ID tracks in terms of η, ϕ and p_T. The CB muons have the best resolution on the muons parameters: the p_T resolutions benefits of the long lever arm and of the precision of the two independent measurements used as input (SA and ID tracks), while the vertex parameters are provided by the ID track. The reconstruction efficiency of CB muons is $\sim 92\%$.

- *Tagged Muons*: The Tagged muon (ST) category is aimed at maximize the muon reconstruction efficiency in the low-p_T region: a low-p_T muon may not

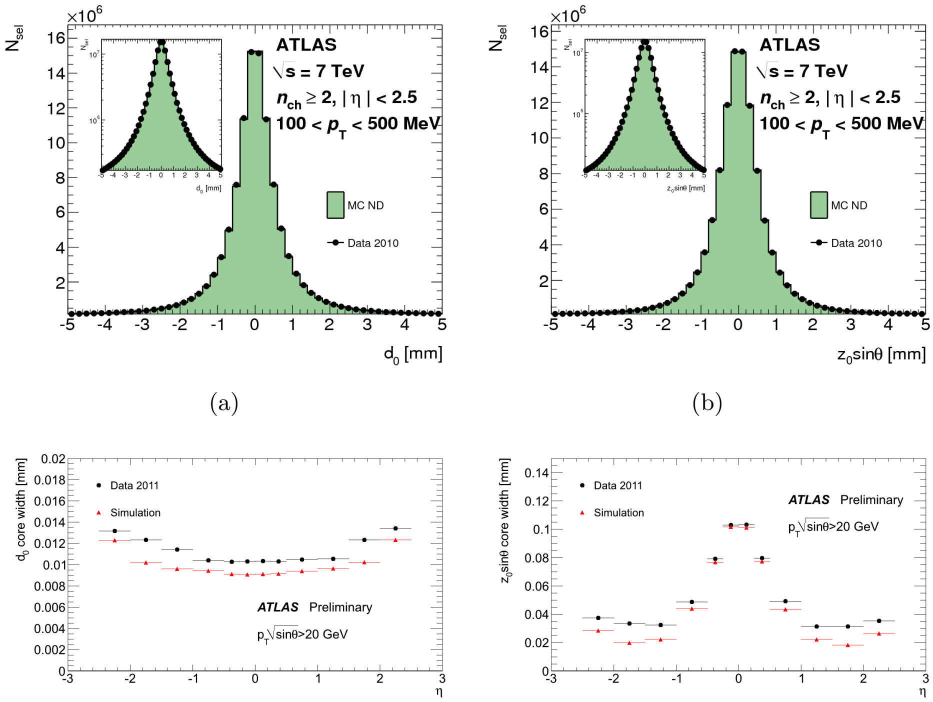

(a) (b) (c) (d)

Figure 3.2. Data-Monte Carlo comparison for the transverse impact parameter d_0 3.2(a) and for the longitudinal impact parameter z_0 multiplied by $\sin(\theta)$ 3.2(b). Figures 3.2(c) and 3.2(d) show the performances on the d_0 and z_0 for high p_T tracks

reach the spectrometer middle station because of magnetic field or might not penetrate the outermost calorimeter layers, and thus might not be reconstructed by the SA or CB algorithms. This muon category is build with an inside-out method which extrapolates an ID track to the entrance of the MS, and look for nearby hits in the first layer of the muon chambers. The reconstruction efficiency for ST muons is $\sim 98\%$.

- *Calorimeter Muons*: The Calorimeter muons also are reconstructed using an inside-out algorithm: here the ID track is matched with a calorimetric deposit compatible with a muon signature.

In ATLAS muons can be reconstructed using two independent algorithms: STACO [31] and MUID [32], and each of them provides algorithms to reconstruct all the four muon categories. The two families use different approaches to reconstruct the tracks starting from the hit in the detectors, and it has been proven that they have vey similar performances [31, 32]. Anyway the default algorithm used for physics analyses is STACO, its performances are shown in fig. 3.3, and all the efficiencies listed above are for STACO muons. As can be seen from fig. 3.3, there is a good agreement between data and Monte Carlo in both the p_T and the η spectra (any disagreement is accounted for with a scale factor, as explained in section 4.3). The two plateaus have a very flat and stable value along the two coordinates and the slightly inefficient regions at $|\eta| \sim 1$ and $|\eta| \sim 2$ seen in fig 3.3(b) are due to the

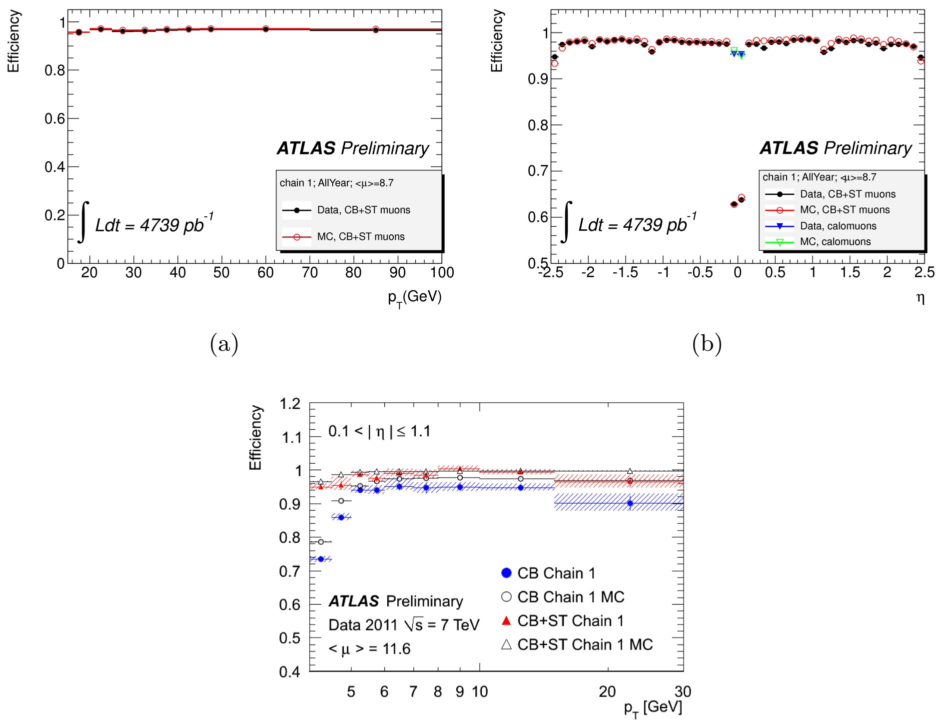

(c)

Figure 3.3. Muon reconstruction efficiency as a function of η 3.3(b) and p_T 3.3(a), 3.3(c) in 2011 pp collisions for the STACO (chain 1) family

presence of the structures on which the ATLAS is leant, the so called feet; while the $\eta = 0$ region is where the two halves of the ATLAS muon spectrometer (lying in the $|\eta| > 0$ and $|\eta| < 0$ regions) come close. In this region the coverage of the muon spectrometer is not optimal.

3.3 Electron Reconstruction

The electron reconstruction algorithms are designed to reconstruct electrons in a wide E_T range (from few GeV up to the TeV scale) using the informations collected by the ID and the calorimetric system.

Starting from an energy deposit in the EM calorimeter, a sliding window algorithm [33] is applied in order to identify the best rectangular cluster (of fixed size) which contains the deposit. Once the cluster is identified, the reconstruction algorithm search for an ID track matching the energy deposit in a $\Delta\eta \times \Delta\phi$ range of 0.05×0.10 and with momentum p compatible with the cluster energy E: $E/p < 10$. If a matching track is found, then the algorithm searches for associated conversions. If no conversions are found, then a candidate electron is created. On top of this basic selection many other request can be done, thus creating three electron categories of different quality (and hence purity):

- *Loose++*: To build this category a very simple electron identification based on limited informations from the calorimeter is performed: cuts are applied

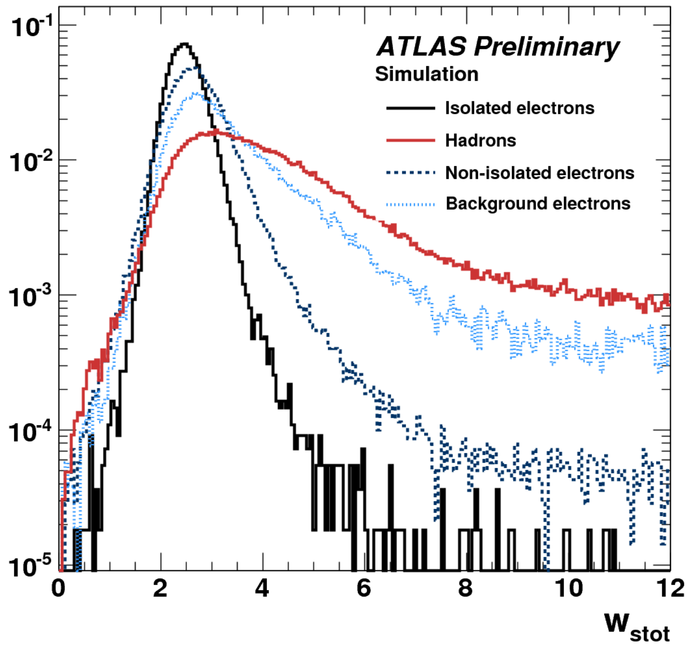

Figure 3.4. Width of the electromagnetic shower for electrons (red line) and for the main backgrounds

on the hadronic leakage (i.e. the fraction of the cluster energy in measured in the hadronic calorimeter) and on the shower-shape variables (see fig. 3.4), computed using only the middle layer of the calorimeter. This category has very high identification efficiency ($\sim 97\%$), but provides poor background rejection.

- *Medium++*: This category offers a better background rejection as it includes information from the first layer of the EM calorimeter, aimed at improve the $e - \pi$ separation. In addition to this, higher quality on the ID track is requested too: cuts on the total number of pixel plus SCT hits are applied. This category improves the background rejection of a factor of $3 - 4$ with respect to the *loose++* category, while the identification efficiency is reduced by about 10%.

- *Tight++*: This category makes use of all the particle identification tools currently available fo electrons. Starting from a *medium++* electron, the following additional cuts are applied:

  - on the number of vertexing layer hits to reject electrons from conversions
  - on the number of TRT hits
  - on the ratio of the high-threshold hits to the number of TRT hits, in order to reject the background from charged hadrons
  - on the difference between the cluster and the extrapolated track position in η and ϕ

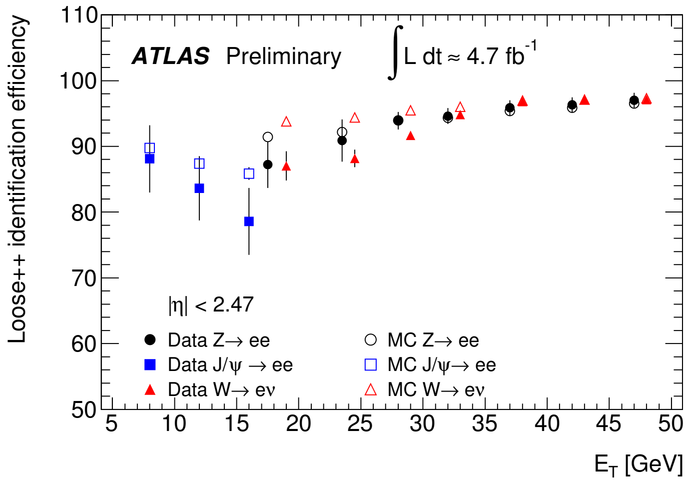

Figure 3.5. Electron reconstruction efficiency vs. E_T **??** for the different electron qualities measured with the tag and probe method on a $Z \to e^+e^-$ sample

In this category the background rejection is $\sim 10^5$, while the identification efficiency is $\sim 80\%$.

The *++* in the above names derive from an historical reason: these categories come from an update of the previous categories which were named *Loose*, *Medium* and *Tight*. Performances of the electron reconstruction are shown in fig. 3.5. The measurement has been performed on a sample of $Z \to e^+e^-$ events and the *tag and probe* method has been used.

3.4 Jet Reconstruction

When an hadronic particle (a quark or a gluon) is produced, it does not propagate in the space as leptons do, but, because of QCD intrinsic features (*quark confinement* [5]), they "hadronize" into a shower of hadronic particles called jet. As for the electrons, the hadronic jets reconstruction is seeded by calorimetric informations: given an energy deposit in the calorimetric system, two different methods can be used in ATLAS to convert that energy deposit into an input to the jet reconstruction chain.

- *Calorimeter towers*: in this case the calorimetric cells containing the energy deposit are projected into a 0.1×0.1 granularity $\eta \times \phi$ grid. The tower signal thus comes from the sum of the cell signal, weighted by the fraction of the cell overlapping the tower area

- *Topological clusters*: the topological cluster method basically attempts to reconstruct the three-dimensional energy deposit representing the shower due to a particle entering the calorimeter. The clustering starts with a seed cell having a signal significance, $\Gamma = E_{cell}/\sigma_{noise,cell}$, above a fixed threshold S, i.e. $|\Gamma| > S = 4$. All the neighbour cells with respect to the seed cell are collected into the cluster if Γ is above a secondary threshold N, $|\Gamma| > N = 2$. Finally a

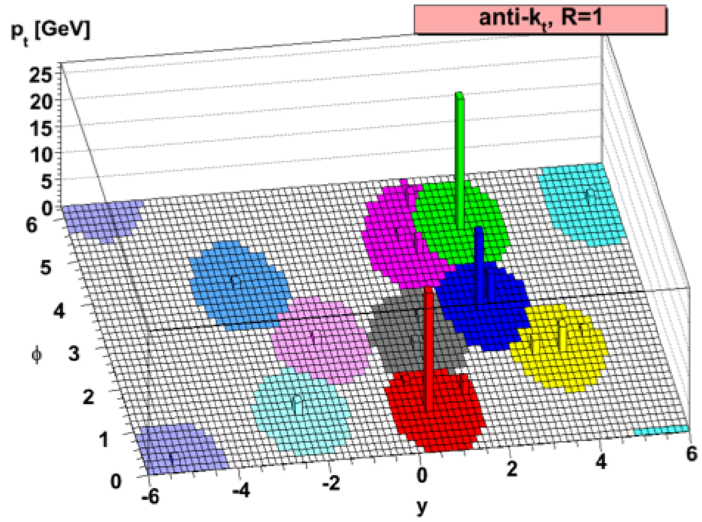

Figure 3.6. A sample parton-level event (generated with HERWIG), clustered with anti-kt algorithm. Areas of the resulting hard jets are shown

ring of cells with Γ above the basic threshold P, $|\Gamma| > P = 0$, is added to the cluster, as shown in fig. 3.6.

Once the topological clusters or the calorimeter towers have been identified, the real jet construction takes place. Many methods have been proposed and used to define a jet, and a detailed discussion of these methods goes beyond the aim of this thesis. In the following the default *anti-k_T* algorithm adopted in ATLAS is presented.

The *anti-k_T* algorithm belongs to the category of the *Cluster Algorithms* which build jets by clustering them with a pair-wise procedure[1]. In this category two distances are introduced: d_{ij} between entities (particles, jet candidates) i and j, and d_{iB} between the entity i and the beam B. The algorithm proceeds identifying the smallest distance:

- if it is a d_{ij} distance, i and j are combined together in a single jet
- if it is a d_{iB} distance, i is considered as a single complete jet and is removed from the list

This procedure is iterative, so the distances are recalculated and the procedure is repeated until no entities are left. The quantities d_{ij} and d_{iB} are defined as follows:

$$d_{ij} = min(k_{Ti}^{2p}, k_{Tj}^{2p})\frac{\Delta R_{ij}^2}{R^2} \tag{3.1}$$

$$d_{iB} = k_{Ti}^{2p} \tag{3.2}$$

where

$$\Delta R_{ij}^2 = (\eta_i - \eta_j)^2 + (\phi_i - \phi_j)^2 \tag{3.3}$$

[1]The other jet algorithm category is the *Cone Algorithm*, in which jets are reconstructed starting by a cone which is optimized to contain the most of the jet energy

and k_{Ti}, η_i and ϕ_i are the transverse momentum, the pseudorapidity and the azimuth of particle i respectively, and R is the reference jet width. Depending on the value of the parameter p several clustering algorithms are defined, and for the *anti-k_T* algorithm $p = -1$. This means that objects with high transverse momentum k_T are merged first and the reconstructed jets have low sensitivity to soft radiation. The choice of the R parameter is analysis dependent, and in ATLAS two default R values are used: $R = 0.4$ and $R = 0.6$.

In ATLAS jets can be reconstructed with different quality criteria: *Looser*, *Loose*, *Medium* and *Tight* [35]. Since the noisy channels of the calorimeter and its electronics can lead to fake energy deposits not due to particles going through the calorimeter (which can be reconstructed as fake jets), many quality criteria on the features of the recorded pulse are applied in order to discriminate between real and fake jets candidates. The four jet categories differ for the cuts applied on the calorimetric variables of the signal. The Looser selection was designed to provide an efficiency above 99.8% with a fake rejection as high as possible while the Tight selection was designed to provide a much higher fake rate jet rejection with an inefficiency not larger than a few percent. The two other sets of cuts correspond to intermediate fake rejections and jet selection efficiencies. Efficiencies of the four jet reconstruction categories are shown in fig. 3.7 as a function of the jet p_T.

As explained above the jets in ATLAS are reconstructed using solely the calorimeter, however tracks reconstructed in the ID can be associated to a jet. Tracks are associated to jets using a simple geometrical matching criterion: the radial distance

$$\Delta R = \sqrt{(\eta_{\text{jet}}^{\text{PV}} - \eta_{\text{track}}^{\text{PV}})^2 + (\phi_{\text{jet}}^{\text{PV}} - \phi_{\text{track}}^{\text{PV}})^2} \tag{3.4}$$

is calculated for each track, where $\eta_{\text{jet}}^{\text{PV}}$ and $\phi_{\text{jet}}^{\text{PV}}$ are the pseudorapidity and the azimuthal angle of the jet with respect to the primary vertex, and $\eta_{\text{track}}^{\text{PV}}$ and $\phi_{\text{track}}^{\text{PV}}$ are the pseudorapidity and the azimuthal angle of the track at the perigee[2] with respect to the primary vertex. Any track for which the condition

$$\Delta R < 0.4 \tag{3.5}$$

is satisfied are considered as matching the jet, and therefore are associated to it.

3.4.1 Jet energy resolution

The jet energy resolution is a crucial ingredient of the analysis presented in this thesis, since it is used in the jet pairing procedure explained in detail in 5.3.3. The procedure adopted to measure the jet energy resolution is explained in detail in [36]. It basically relies on the assumption that in events containing only two jets, the p_T's of the two jets shall be balanced because of the momentum conservation in the transverse plane (see section 2.2.1 for details). Starting from this assumption the jet energy resolution can be measured studying the asymmetry observed between the jet p_T's in such a configuration. To perform this measurement, jets in the same rapidity y region are chosen in order to minimize additional detector effects that may introduce secondary effects. The jet energy resolution is thus obtained in $p_T \times \eta$

[2] The perigee of a track is defined as point of closest approach to the beam axis

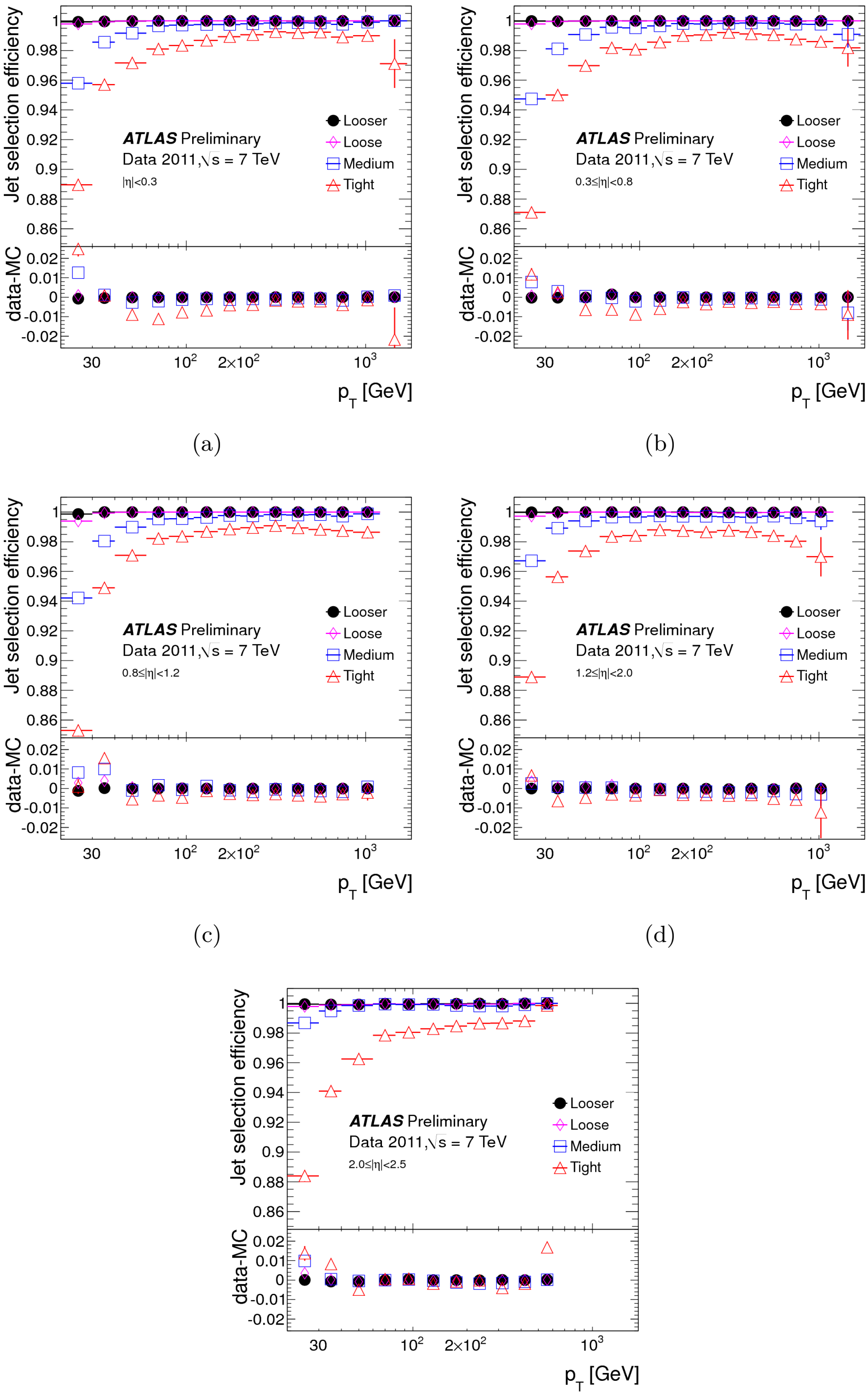

(e)

Figure 3.7. Jet quality selection efficiency for *anti-*k_T jets with $R = 0.4$ as a function of p_T in η ranges, for the four sets of selection criteria

bins. Given the above, the fractional jet energy resolution can be parametrized as (following the parametrization of the energy resolution for the calorimeter):

$$\frac{\sigma_{p_T}}{p_T} = \frac{N}{p_T} \oplus \frac{S}{\sqrt{p_T}} \oplus C \tag{3.6}$$

where N, S, and C are the noise, stochastic and constant terms respectively. Once the measurement according to the method mentioned above is performed (and validated with Monte Carlo simulations), the distribution of the results can be built in each η bin and a fit with the functional form in eq. 3.6 can be done. The results of such a measurement is shown in fig. 3.8 for a specific rapidity bin. In the rapidity bin

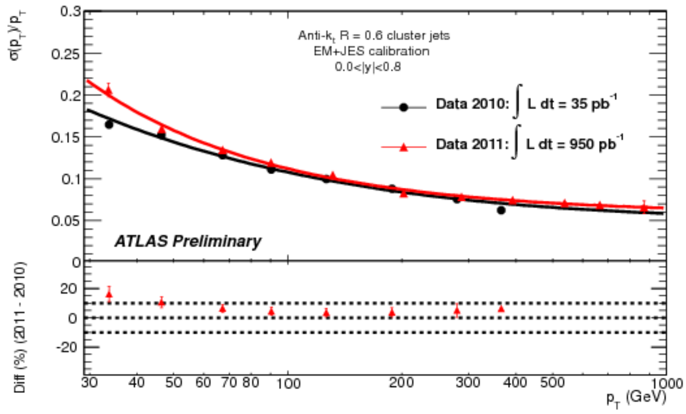

Figure 3.8. Measurement of the jet energy resolution in 2010 and 2011 data in a given y (i.e. η) bin

$0.0 < |y| < 0.8$ shown in figure, a $\sigma(p_T)/p_T$ of about 18% is reached for jets having $p_T = 40$ GeV/c, while at $p_T = 500$ GeV/c $\sigma(p_T)/p_T \sim 7\%$ Once a measurement of the jet energy resolution is obtained, it is possible to link any measured jet falling in a given $\eta - p_T$ region to its corresponding resolution. This is used as an ingredient of the jet pairing algorithm explained in section 5.3.3.

3.4.2 b-jets Identification

A very important item of many physics analyses is to identify the jets coming from the hadronization of a b quark among the other jets. To do this b-*tagging* algorithms have been developed to exploit the features and the peculiarities of the b-jets in order to identify them.

It is possible to distinguish jets originating from b-quarks exploiting handles coming from the peculiar features characterizing them:

- the long mean lifetime of th b flavoured hadrons produced in the hadronization of the b-quark (~ 1.6 ps) makes it possible to reconstruct a displaced secondary vertex which can be distinguished from the primary vertex
- high-track multiplicity
- high p_T of the decay products

Various b-tagging algorithms can be defined, based on these discriminating variables, on secondary vertex properties and on the presence of leptons within b-jets, and for each jet they usually give as output a weight reflecting the probability that the input jet originates from a b-quark. The one used in this analysis is based on the measurement of the *impact parameter* (see, fig. 3.9), and on the reconstruction of the secondary vertex. The tranverse impact parameter d_0 is the distance in the

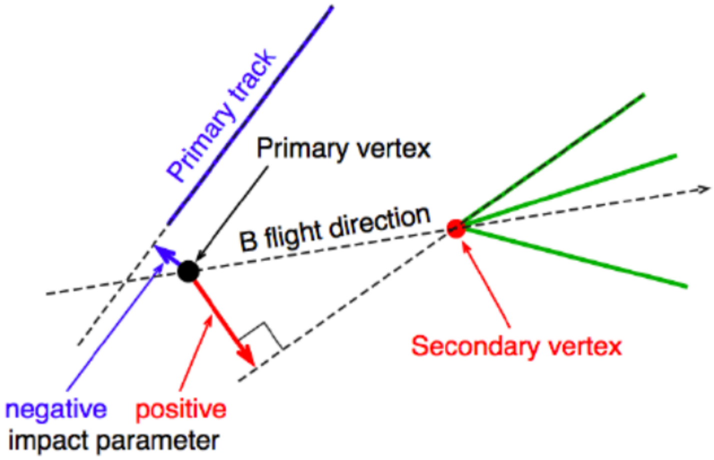

Figure 3.9. Schematic representation of a b-hadron decay and definition of the impact parameter

transverse plane $x - y$ between the point of closest approach of a track and primary vertex, while the longitudinal impact parameter is the z-coordinate of this point (z_0). The b-tagging algorithm used is called *MV1* (MultiVariate tagger) [38]: it is based on a neural network, and takes as input the output weights of three simpler tagging algorithms:

- IP3D [37], based on the d_0 significance
- SV1 [37], based on the reconstruction of secondary vertexes
- JetFitterCombNN [37], which performs a fit on the flight direction of the b-hadrons and then combines the result with the output weights of IP3D and SV1.

Figures 3.10(a)-3.10(b) shows the data-Monte Carlo comparison for the three taggers used as input to the MV1 algorithm. The output of the MV1 tagger is a continuous value w_{MV1}, and it is possible to choose a threshold value $\bar{w}$ to tag a jet as a b-jet: if $w_{MV1} > \bar{w}$ then the jet will be considered a b-jet, otherwise it will be considered a light-flavor jet. The data-Monte Carlo comparison on the output weight of the MV1 algorithm is shown in fig. 3.10(c). As can be seen the data-Monte Carlo agreement is good for the considered taggers. In particular the output weight of the MV1 tagger clusters to 0 for light jets, while assumes values near to 1 for b-jets. Moreover in figure 3.10(c) it can be seen that the output weight of the MV1 tagger has a peak at $w \sim 0.15$. It is due to jets coming from the hadronization of the c-quark. The choice of the value of $\bar{w}$ depends on the desired b-tagging efficiency and on the desired mistag rate one wants to have in the analysis as shown in fig. 5.7.

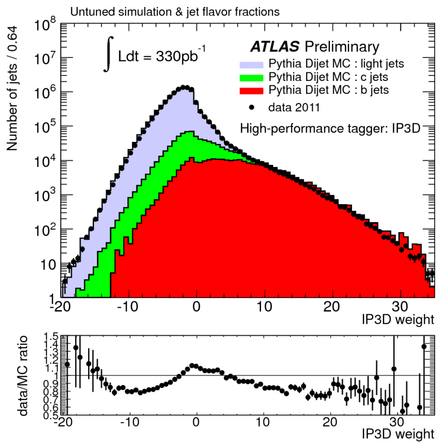

(a)

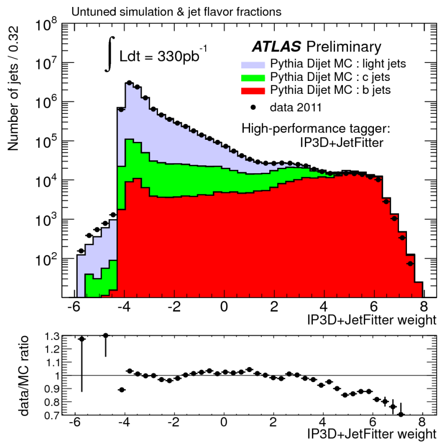

(b)

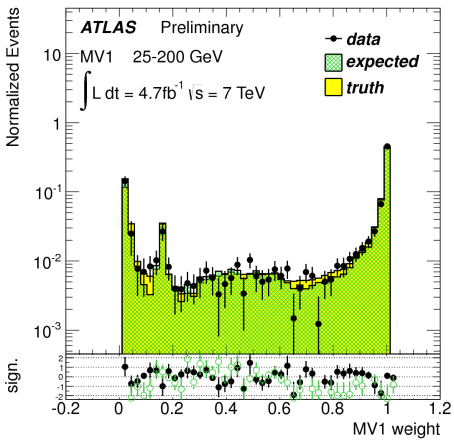

(c)

Figure 3.10. Data-MC comparison of the output of the input taggers: IP3D 3.10(a), JetFitterCombNN 3.10(b) (also known as *JetFitter+IP3D*). The data-Monte Carlo comparison for the output of the MV1 tagger is also shown 3.10(c)

Even if the data-Monte Carlo agreement shown in fig. 3.10 is good, some differences can be seen. These differences are taken into account with a jet by jet scale factor. Details on the b-tagging scale factor are given in section 4.3.

3.5 Missing transverse energy

The missing transverse energy, E_T^{miss}, in a collider experiment is the energy imbalance in the transverse plane, where the energy conservation is expected (see chapter 2 for details). The physical source of such an imbalance is the presence of unseen particles such as neutrinos which go through all the detector without leaving any signal, and it is measured thanks to the tightness of the calorimetric system. In addition many detector-related effect (such as mismeasurements of energy) can give rise to E_T^{miss}. The E_T^{miss} reconstruction algorithm starts from all the calorimetric cells belonging to

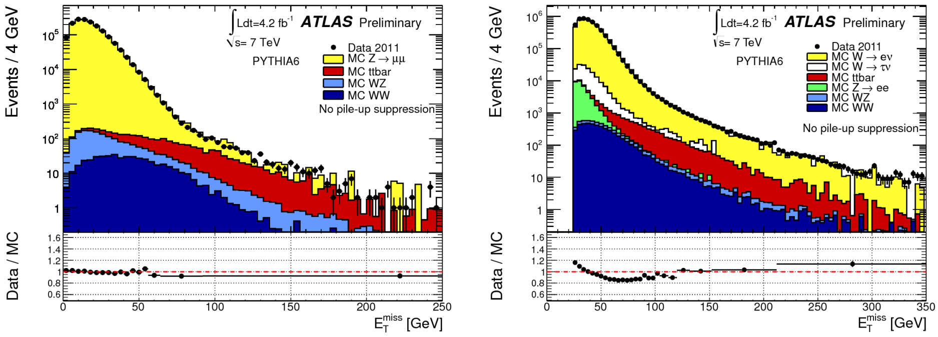

(a) (b)

Figure 3.11. Distribution of E_T^{miss} measured in $Z \to \mu^+\mu^-$ 3.11(a) and $W \to e\nu$ 3.11(b) events for data and Monte Carlo

topological clusters (see section 3.7) in the $|\eta| < 4.9$ range, considering their energy and also their position in θ and ϕ, as shown in eq. 3.10. The final E_T^{miss} calculation is defined as

$$E_T^{\text{miss}} = \sqrt{(E_x^{\text{miss}})^2 + (E_y^{\text{miss}})^2} \tag{3.7}$$

where the $E_{x(y)}^{\text{miss}}$ contain contribution from both calorimetric energy deposits and corrections for the muons in the event in each transverse direction x and y.

$$E_{x(y)}^{\text{miss}} = E_{x(y)}^{\text{miss, Calo}} + E_{x(y)}^{\text{miss, Muon}} \tag{3.8}$$

where

$$E_x^{\text{miss, Calo}} = -\sum_{i=1}^{N_{\text{cell}}} E_i \sin\theta_i \cos\phi_i \tag{3.9}$$

$$E_y^{\text{miss, Calo}} = -\sum_{i=1}^{N_{\text{cell}}} E_i \sin\theta_i \sin\phi_i \tag{3.10}$$

and the $E_{x(y)}^{\text{miss, Muon}}$ takes into account the energy muon energy deposit as it goes through the calorimetric system. The $E_{x(y)}^{\text{miss, Calo}}$ terms contain all the energy deposits in the calorimeter: all the energy deposits associated to reconstructed physics objects (electrons, photons, taus, jets) are considered as well as those that are not associate to any reconstructed object. This last contribution may suffer of contamination from noisy channels, but this is avoided by means of quality requirement on any energy deposit contributing to the E_T^{miss} calculation [39]. Figure 3.11 shows the reconstruction of E_T^{miss} in $Z \to \mu^+\mu^-$ (fig. 3.11(a)) and $W \to e\nu$ (fig. 3.11(b)) for both data and Monte Carlo. The very good agreement between data and Monte Carlo highlights the very good performances of the ATLAS detector and its good understanding. Figure 3.12 the E_T^{miss} resolution as a function of the reconstructed primary vertexes in each event. This shows how pileup affects calorimetric measurements and the effect of pileup suppression methods (blue empty markers in the figure).

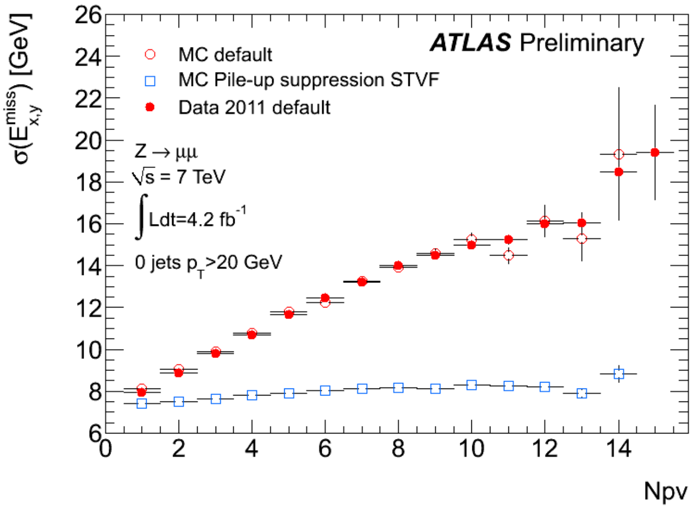

Figure 3.12. $E_T^{\rm miss}$ resolution as a function of the number of reconstructed primary vertexes (i.e. as a function of the pileup). The effect of the pileup suppression is shown too

Chapter 4

Details on Monte Carlo samples

In this analysis many Monte Carlo programs are used to model several aspects that need to be taken into account in such a study, from the detector, the physics processes occurring in the proton collision and those happening after the collision (final state particles interacting with the detector, quark hadronization, etc). In this chapter some relevant details about the Monte Carlo programs used to simulate signal and background processes are given, and the main correction needed to make them properly reproduce the data are illustrated.

4.1 General details about Monte Carlo

As usual in particle physics experiments (and in other fields too), the propagation of the generated particles through the ATLAS detector and their interaction with the detector material is simulated using the GEANT4 software toolkit [43]. This program offers a comprehensive set of physics processes to model the behaviour of particles and their interaction with matters on a wide range of energies (from $\mathcal{O}(100)$ MeV up to the TeV scale). The GEANT4 program is interfaced to the ATLAS simulation framework [44] which provides the geometry and the properties of the ATLAS detector.

4.1.1 Luminosity

In general an arbitrary number of events can be generated for each Monte Carlo sample, and since the generated events have an intrinsic production cross section σ, the integrated luminosity of the Monte Carlo sample taken into account can be defined as:

$$L = \frac{N}{\sigma} \tag{4.1}$$

which is arbitrary as well since it depends on the number of generated events N. The production cross section of the Monte Carlo samples depends on the intrinsic cuts (e.g. minimum p_T) applied to the relevant variables of the simulated processes. Details on each Monte Carlo program are given in the next sections.

The integrated luminosity of the Monte Carlo samples in principle does not correspond to the integrated luminosity recorded in data, but is usually much larger in order to reduce statistical uncertainties on the templates used to model the processes involved in the analysis. Because of this, once a template is obtained applying the analysis selection, it has to be scaled to the recorded luminosity in order to be able to coherently compare data to Monte Carlo predictions. Each Monte Carlo template is thus scaled by a scale factor obtained as the ratio of the recorded luminosity to the Monte Carlo luminosity:

$$\mathrm{SF} = \frac{L_{\mathrm{data}}}{L_{\mathrm{MC}}} = \frac{L_{\mathrm{data}}}{N} \times \sigma \tag{4.2}$$

This scale factor is used for each Monte Carlo sample included in the plots shown in the next chapters.

4.1.2 Pileup reweight

Pileup (introduced in section 2.1) affects physics analysis in two main ways. Firstly and most importantly, additional proton-proton interactions may occur in the same bunch crossing as the hard interaction of interest. Such interactions produce extra soft particles and potentially reduce the efficiency for selecting signal events. During the 2011 LHC running, the number of interactions occurring per bunch crossing varied with time due to the changing machine parameters, including the beam intensity and the transverse size and number of bunches, as shown in fig. 4.1. This effect is referred to as *in-time pileup*, and it may have an effect on the analysis: extra jets from pileup events, i.e. real additional interactions, may be mistaken for signal jets. In addition to this, because of the additional QCD activity due to multiple interactions, jets arising from the primary event and the missing E_T may gain extra energy from pileup events.

In addition to the in-time pileup there is also the *out-of-time pileup*, which depends on the beam intensity in bunches preceding the one during which a recorded event occurs. This effect is accounted for in the Monte Carlo samples, which assume a 50 ns bunch spacing, as was the case for the vast majority of the data used in this search (12 pb^{-1}of data at the beginning of 2011 were taken with a 75 ns bunch spacing). As the out-of-time pileup effects depend on the intensity of several prior bunches, the position of a bunch within the bunch train is also important.

To model the effects of pileup, the Monte Carlo samples for the above processes were simulated with a fixed distribution of additional minimum-bias interactions. This is subsequently reweighted to the distribution observed in the data taking into account the mean number of interaction per bunch crossing in both data and Monte Carlo as a function of the data-taking period (i.e. as a function of the machine parameters). This gives a weight that has to be applied to the Monte Carlo events in order to reproduce the distributions measured in data. Therefore the weight varies event by event on the basis of the actual number of interactions of each event, ensuring in the end to reproduce the data distribution of the number of reconstructed vertices and other pile-up related quantities.

4.2 Monte Carlo samples used in this analysis

In the analysis presented in this thesis the signal processes as well as all the background processes but multijet production arising from QCD processes are modelled with Monte Carlo simulations, and some of them are cross checked with data in ad hoc control regions (a detailed explanation is in chapter 5). In this section

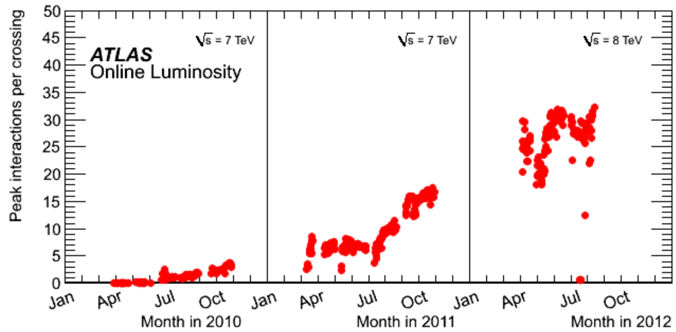

(a) Peak number of interaction per bunch crossing in the three years of LHC run

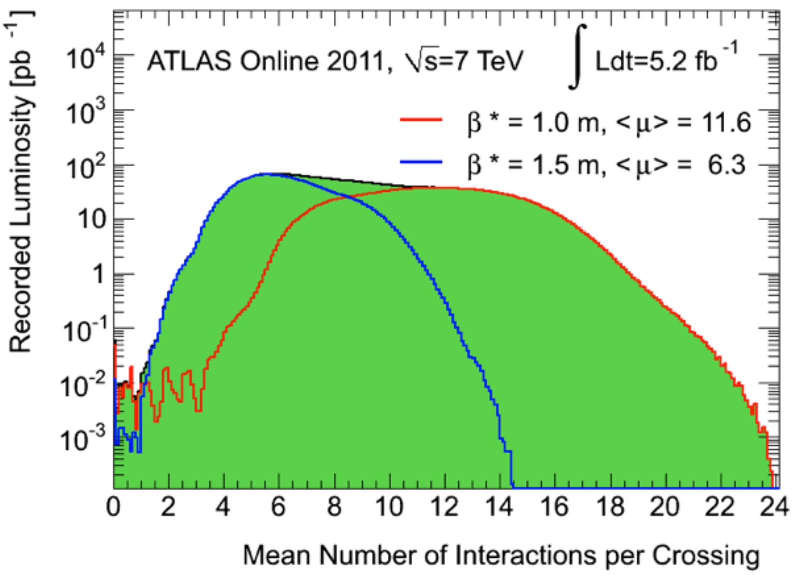

(b) Mean number of interaction per bunch crossing in the 2011 LHC run

Figure 4.1. Pileup: the peak and the mean numbers of interactions per bunch crossing

an overview of the Monte Carlo programs used in this analysis is given, as well as a comparison with other available programs and with data.

4.2.1 Alpgen

The ALPGEN [45] program is used to model one of the dominant background of this analysis which is the Drell-Yan/Z boson production with additional jets in the final state. As explained in the next sections (in particular in section 5.3.1) an ad hoc Drell-Yan simulation is needed since the searched signal process spreads over a wide range of dilepton invariant mass. The ALPGEN program provides calculation of the exact matrix element of the simulated processes performed ad the LO for both QCD and Electro-weak interactions. On top of that the cross sections of the samples can be scaled with so called *k-factor* to take into account NLO calculations. This is indeed what is done in this analysis, and the applied *k-factor* is 1.22. Both the Drell-Yan and $Z+$jets processes are composed of several independent samples, depending on the number of additional partons generated in the hard scattering: the samples are labelled with the NpX, where X indicates the number of additional partons which ranges from 0 to 5. While generating the events, minimal cut are applied to the event kinematic variables. A selection of the relevant cuts follows.

$$p_{T_q} > 20 \text{ GeV}/c \tag{4.3}$$

$$\Delta R(q, q') > 0.4 \tag{4.4}$$

$$m_{\ell\ell} > 40 \text{ GeV}/c^2 \tag{4.5}$$

$$10 < m_{\ell\ell} < 40 \text{ GeV}/c^2 \tag{4.6}$$

where q stands for the generic parton generated in the hard scattering, eq. 4.5 refers to the $Z+$jets samples and eq. 4.6 refers to the Drell-Yan samples.

Since in the Drell-Yan/$Z+$jets samples the production of heavy flavor quarks is not taken into account in the matrix element but arises only from the hadronization process (e.g. gluon splitting), additional samples for Drell-Yan and Z boson production processes in addition to b quarks are needed. In these DY/$Z+$ heavy jets samples the heavy flavor production takes place in the matrix element. Since some overlap may occur in the event generation between the DY/$Z+$jets and the DY/$Z+b$-jets samples, an overlap removal procedure have been developed, as described in [46]. This is based on looking at the opening angle between pairs of heavy-flavour quarks. In the DY/$Z+$ light flavour samples, events containing heavy-flavour pairs generated via parton showering are removed if $\Delta R > 0.4$; conversely, in the heavy-flavour sample, events containing pairs with $\Delta R < 0.4$ produced directly from the matrix element are removed. Cross sections for the DY/$Z+b$-jets samples are calculated at the LO for both the QCD and the Electro-weak processes. As for the DY/$Z+$ light jets they can be scaled by a factor of 1.22 to take into account he NLO calculation. Actually this is not enough for the DY/$Z+b$-jets samples who need a further scaling by a 1.4 factor to match the latest calculation including NLO QCD processes. This is explained in detail in [41] and in [42]. The kinematic cuts used in the generation of the DY/$Z+b$-jets events are the same used for the DY/$Z+$ light jets and listed in formulae 4.3-4.4, while the invariant mass ranges are:

$$m_{\ell\ell} > 30 \text{ GeV}/c^2 \tag{4.7}$$

$$10 < m_{\ell\ell} < 30 \text{ GeV}/c^2 \tag{4.8}$$

where eq. 4.7 holds for the $Z + b$-jets sample and eq. 4.8 holds for the Drell-Yan $+b$-jets.

In principle many Monte Carlo programs are available to model the production of a Z boson in association with jets. Figure 4.2 shows the comparison between the

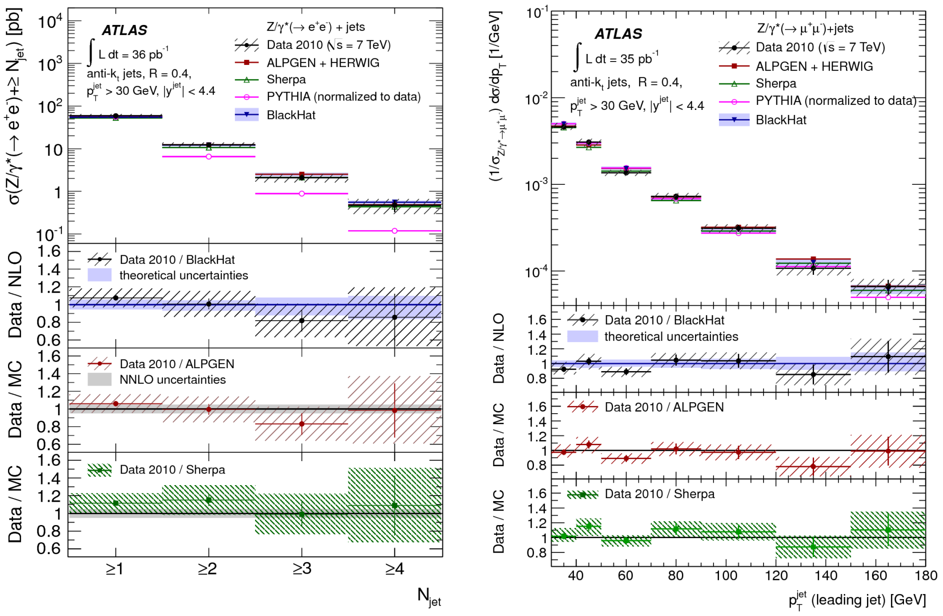

(a) (b)

Figure 4.2. $Z \to e^+e^- +$ jets cross section production as a function of the number of additional jets 4.2(a) and $Z \to \mu^+\mu^- +$ jets production cross section as a function of the leading jet p_T4.2(b) in data and corresponding results obtained with several Monte Carlo programs

production rate of a Z boson with an increasing number of additional jets measured in data and several Monte Carlo generators, as well as the normalized Z boson production cross section as a function of the leading jet p_T. As can be seen a very good agreement is found between data and the ALPGEN program for any number of additional jets considered in the plot.

4.2.2 MC@NLO

The MC@NLO program [47] is used to model the Standard Model diboson production which constitutes an irreducible background to the searched signal process, as well as the top background which is instead one of the main processes contributing to the final analysis sample. Within this program a matching between NLO matrix elements and parton shower generators is provided. This matching is based on the so called *subtraction method*, which provides a proper matching between NLO calculations and parton-showers without introducing great approximations, and thanks to which event weights can be controlled properly. This provides the possibility to have a Monte Carlo generator which includes calculation up to the NLO.

As said above MC@NLO is used for Standard Model diboson production processes, namely W^+W^-, ZW^+, ZW^- and ZZ with all the possible final states that can contribute to the final sample used in this analysis (see section 5.1.3 for details).

4.2.3 PowHeg

The POWHEG program [48, 49, 50] is used to model the signal samples in the Higgs boson mass range $120 - 180$ GeV/c^2 for both the gluon fusion ($gg \to H$) and the vector boson fusion ($qq \to qqH$) production mechanisms for the $H \to ZZ^* \to \ell^+\ell^- q\bar{q}$ process (with $\ell = e, \mu, \tau$). The cross sections of the Higgs boson production mechanisms include NNLO contributions for the gluon fusion process, while for the vector boson fusion process calculations are performed up to the NLO. These cross sections are shown in table 5.1. For both the production mechanisms the POWHEG event generator is interfaced to PYTHIA for hadronization, which is interfaced to PHOTOS [52] for final state radiation and to TAUOLA [51] for the simulation of τ decays. The gluon fusion sample does not include the specific sum of all the logarithmic terms up to the NLL contribution for very low transverse momentum of the Higgs boson. A detailed study of the impact of this feature is shown in ref. [49]. To recover the discrepancy that is found, the events generated for the gluon fusion production mechanism can be reweighted in order to match latest calculations performed with the `HqT` program [60]. This is achieved applying a weight to the events generated in the gluon fusion sample which depends on the true Higgs boson p_T.

4.3 Monte Carlo samples compared to data

After the generation of the events occurring in the hard scattering, the interface with the hadronization programs and the detector simulation, the Monte Carlo events can be compared to data. The comparison may occur at several levels, and many checks have to be done in order to have a simulation which properly reproduces the data generated by known processes. Once a reliable agreement is found, the search for new phenomena arising as discrepancy between the observed data and the simulation of known processes can be performed. In this section the corrections needed in order to have a good agreement between the Monte Carlo samples and the data are discussed.

The first correction that we take into account is related to the accuracy of the measurement of kinematic variables. These are measured in the same way in data and Monte Carlo simulation but anyway some differences may arise. In particular differences may arise because of peculiar features of the detector which are not properly reproduced in the detector simulation: as an example if a muon chamber or a module of the ID is sightly misaligned and this is not included in the MC, it would introduce a little bias in the muon p_T reconstruction, resulting in a difference between the p_T scale and resolution measured in data and MC, as shown in figure 4.3. The same holds for electrons and jets. This difference is recovered applying the so called *smearing* to the kinematic variables measured in Monte Carlo, and the correction is applied to each reconstructed object. The smearing is applied introducing a gaussian correction to both the p_T scale and resolution, and the width of the two gaussian functions is evaluated from the entity of the data-Monte Carlo discrepancy. The central value μ of the gaussian function used to quantify the

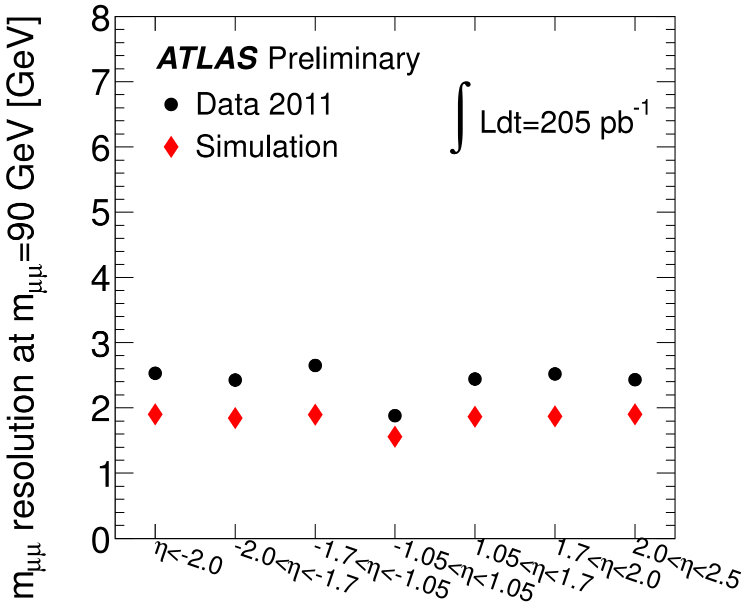

Figure 4.3. Dimuon mass resolution of combined muons in different pseudorapidity regions for data and simulation. The differences between the experimental and predicted resolutions are caused by inert material and residual misalignment not included in the Monte Carlo simulation

correction is used for the central value of the correction itself, while systematic uncertainties are evaluated varying the correction within -1σ and 1σ.

In addition to the above smearing, tiny differences between data and Monte Carlo simulations can be seen in other aspects. Figures 3.3, 3.5 and 3.7 show the reconstruction efficiency of muon, electrons and jets respectively for both data and Monte Carlo. It can be seen that the efficiencies measured in data and Monte Carlo are slightly different. This difference can be taken into account applying a weight to the Monte Carlo events which depends on the kinematic variables (p_T, η) of the reconstructed physics objects in the event. The weight is indeed the scale factor between the efficiency measured in data and the one measured in Monte Carlo. As for the reconstruction efficiency, scale factor can be evaluated for any efficiency taken into account: figure 5.8 shows the trigger efficiencies for the triggers used in this analysis. As can be seen, the triggers may have different performances in data and Monte Carlo. This is recovered with a scale factor given by the ratio of the efficiency on data to the efficiency in Monte Carlo, and is computed for each event as a function of the kinematic variables (p_T and η) of the triggered leptons.

Another aspect of the discrepancy between data and Monte Carlo is the b-tagging efficiency: figure 5.7 shows the output weight of the b-tagging algorithm used in this analysis and the tagging efficiency as a function of the jet p_T for a given working point of the tagger. As can be seen different performances are obtained for data and Monte Carlo. This discrepancy can be taken into account by means of a scale factor. The scale factor receives contribution from all the reconstructed jets in the Monte Carlo event: for each a scale factor is calculated as a function of the jet p_T, η, the jet true flavor and the output of the tagger for that single jet (i.e. whether the jet is tagged or not). To compute the global b-tagging scale factor, all the single

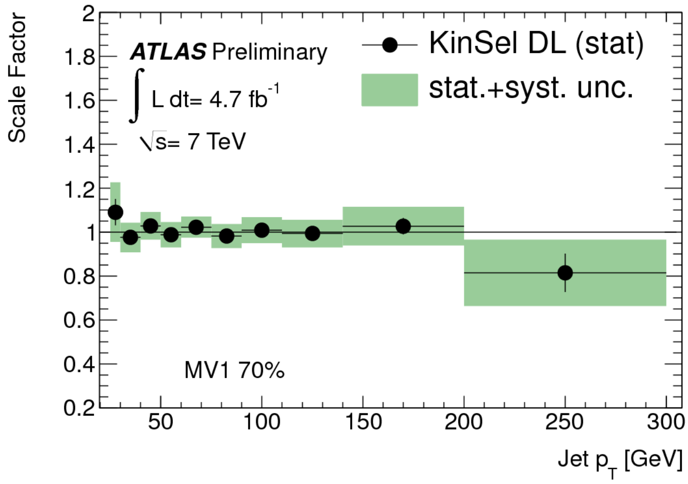

Figure 4.4. The b-tagging scale factor as a function of the jet p_T

scale factors computed for each jet in the event are multiplied together. Figure 4.4 shows the jet by jet scale factor for a given working point of the tagger obtained as described above.

As explained in section 4.1.2 an additional event-weight is used to take into account the effect of the pileup: this depends on the average number of primary vertexes reconstructed in data and Monte Carlo.

The combination of all these scale factors and weights in order to obtain a global weight for each event is explained in section 5.4.

Chapter 5

The $H \to ZZ^* \to \ell^+\ell^- q\bar{q}$ Analysis

After having explained the theoretical background that leads to the introduction of the Higgs boson in chapter 1, the experimental setup used to perform the search of such a particle in the $H \to ZZ^* \to \ell^+\ell^- q\bar{q}$ channel in chapter 2 and how the physical objects (electrons, muon and jets) produced in the pp collision are reconstructed and measured in ATLAS (chapter 3), a detailed explanation of how the measurement of this process has been carried out is given in this chapter: the first section is about the Data and Monte Carlo samples used in this analysis, then a section follows explaining which kind of reconstructed particles have been used among the available possibilities offered by the ATLAS reconstruction categories (see chapter 3). Then the selection of the events is explained and a detailed treatment of all the background sources follows. At the end details on the systematic uncertainties affecting the measurements is given.

5.1 Data and Monte Carlo samples

This section describes the data sample used in this analysis along with the relevant signal and background processes and the Monte Carlo generators used to model them.

5.1.1 Data sample

The data used in this analysis were recorded by the ATLAS detector during the 2011 LHC proton run, in which the protons have been collided at $\sqrt{s} = 7$ TeV. The data are subsequently required to satisfy a number of conditions ensuring that ATLAS detector was fully operational with good efficiency while the data were collected. The total integrated luminosity after these quality requirements is approximately 4.71 fb^{-1}. It is known with an accuracy of 3.9%.

5.1.2 Signal samples

Simulated signal samples of $H \to ZZ^* \to \ell^+\ell^- q\bar{q}$, where $\ell = e, \mu, \tau$ and $q = d, u, s, c, b$, have been generated for Higgs boson masses $m_H = 120$–180 GeV/c^2. As said in chapter 4, the POWHEG program is used to generate the simulated samples for both gluon fusion and vector boson fusion production mechanisms. In the same

m_H (GeV)	Gluon fusion σ (pb)	Vector-boson fusion σ (pb)	$\Gamma_{\ell\ell qq}/\Gamma_H$ (%)	Total $\sigma\cdot$ BR (fb)
120	16.65	1.269	0.222	39.8
125	15.32	1.211	0.370	61.2
130	14.16	1.154	0.559	85.6
135	13.11	1.100	0.789	112
140	12.18	1.052	0.965	128
145	11.33	1.004	1.11	137
150	10.58	0.9617	1.16	134
160	9.202	0.8787	0.583	59.8
170	7.786	0.8173	0.332	28.6
180	6.869	0.7480	0.847	64.5

Table 5.1. Cross sections in fb for the $H \to ZZ \to \ell\ell qq$ signal Monte Carlo samples shown for a range of Higgs boson masses. The cross sections are evaluated from theoretical calculations [53] for H production and Higgs boson branching fractions from [53].

chapter the additional scaling and reweight applied on top of the default cross sections are indicated too.

Table 5.1 contains the cross sections and the branching ratios for the signal samples for all the mass hypotheses considered in this analysis.

5.1.3 Background samples

Several background processes give rise to final states with signatures similar to the above signal processes which consists of two opposite sign leptons and two high-p_T jets. These background processes are described in the following.

Z+jets production

As said in chapter 4 the $Z \to ee$, $Z \to \mu\mu$, and $Z \to \tau\tau$ background processes are simulated witht the ALPGEN program, which generates hard matrix elements for Z boson production with with additional numbers of partons p in the final state, where p runs from 0 to 5. The cross sections listed in table 5.2 include a k-factor of 1.22, in order to take into account NLO calculation. Ad hoc samples are used for the Z production in association with heavy-flavor jets, in which the b-quark production happens in the hard interaction and not only in the hadronization process. The possible overlapping events between the $Z+$ light jets and the $Z+$ heavy flavor samples are removed following the procedure described in section 4.2.1 which is based on the angular distance between the heavy quarks. The cross sections listed in table 5.2 include an further scaling of 1.4 for the $Z + b$-jets samples in order to take into account NLO corrections (details in section 4.2.1 and in [41] and in [42]).

Low mass Drell–Yan + jets production

Since in this analysis relatively low–mass same–flavor opposite–sign charged lepton pairs (see section 5.3) are selected, a significant background arises from Drell–Yan $\ell\ell$ hadro-production accompanied by multiple jets. As mentioned in chapter 4, the

Process	σ(fb)
$Z + 0p, Z \to \ell\ell$	836 000
$Z + 1p, Z \to \ell\ell$	168 000
$Z + 2p, Z \to \ell\ell$	50 500
$Z + 3p, Z \to \ell\ell$	14 000
$Z + 4p, Z \to \ell\ell$	3 510
$Z + 5p, Z \to \ell\ell$	988
$Zb\bar{b} + 0p, Z \to \ell\ell$	8 208
$Zb\bar{b} + 1p, Z \to \ell\ell$	3 100
$Zb\bar{b} + 2p, Z \to \ell\ell$	1 113
$Zb\bar{b} + 3p, Z \to \ell\ell$	488

Table 5.2. Cross sections for the $Z+$jets samples generated using the ALPGEN Monte Carlo program, where p refers to the number of additional partons generated in the matrix element. The cross sections listed include a k-factor of 1.22. The cross sections for $Z \to ee$, $Z \to \mu\mu$, and $Z \to \tau\tau$ production are assumed to be the same. The cross sections for the $Z + b$-jets are further scaled up by a factor 1.4 following [41]

ALPGEN Monte Carlo program is also used for the simulation of the Drell-Yan + jets process, where the dilepton mass is required to be in the range $10 < m_{\ell\ell} < 40$ GeV/c^2, with the same setting as for the minimum parton transverse momentum, parton shower, matching algorithm, as for the regular Z+jet (see section 4.2.1 for details). Cross sections are tabulated in Table 5.3, and, as for the $Z+$jets, include a 1.2 k-factor to include NLO calculations. The Drell-Yan dilepton production in association with heavy flavor jets is simulated in a similar way as the $Z + b$-jets process: a dedicated ALPGEN Drell-Yan $+b$-jets sample is used to describe events in which the heavy flavor jets are generated from the matrix element, and the overlapping events are removed with the same procedure described above. In addition, as for the $Z+b$, the cross sections for the Drell-Yan+b-jets are further scaled up by a factor 1.4.

Process	σ(fb)
$DY + 0p$	3 723 000
$DY + 1p$	107 000
$DY + 2p$	50 500
$DY + 3p$	10 200
$DY + 4p$	2 260
$DY + 5p$	561
$DYb\bar{b} + 0p$	20 260
$DYb\bar{b} + 1p$	3 160
$DYb\bar{b} + 2p$	1 180
$DYb\bar{b} + 3p$	566

Table 5.3. Cross sections for the Drell-Yan process +jets samples generated using the ALPGEN Monte Carlo program, where p refers to the number of additional partons generated in the matrix element. The cross sections listed include a k-factor of 1.22. The cross sections for ee, $\mu\mu$, and $\tau\tau$ production are assumed to be the same

Top pair and single top production

Background samples of $t\bar{t}$, single top, and Wt production are simulated using the MC@NLO event generator [47] interfaced to JIMMY 4.31 [54] for simulation of the underlying event. The $t\bar{t}$ sample is filtered at generator level by requiring at least one lepton originating from a W boson with $p_T > 1$ GeV/c. This ensures that only events with at least one leptonic (e, μ, τ) W boson decay are retained; i.e., the case where both W bosons decay hadronically is not considered. Cross sections for the samples are given in Table 5.4.

channel	σ (fb)	filter	σ_{filtered} (fb)
$t\bar{t}$	164 600	0.5562	91 551
single t (s-chan, $W \to e\nu$)	462	–	–
single t (s-chan, $W \to \mu\nu$)	455	–	–
single t (s-chan, $W \to \tau\nu$)	484	–	–
single t (t-chan, $W \to e\nu$)	7 117	–	–
single t (t-chan, $W \to \mu\nu$)	6 997	–	–
single t (t-chan, $W \to \tau\nu$)	7 448	–	–
Wt	14 600	–	–

Table 5.4. Cross sections for the $t\bar{t}$ sample in the lepton-hadron (ℓh) or lepton-lepton ($\ell\ell$) decay mode and for the single top and Wt samples, all generated using the MC@NLO Monte Carlo program. The cross sections are to NLO accuracy taken from [55]. The cross sections are convoluted with branching fractions taken from the Particle Data Book [19]

Diboson production

Background from ZZ production is irreducible, albeit very small within the selection applied for this analysis, since it gives rise to the same final state as the signal process. There is also some contribution from WZ production, since when the Z boson decays into leptons it is not possible to distinguish between the W and the Z bosons decaying hadronically because of the available resolution on jets (more details are given in the following sections). The contribution to the background from WW production is very small.

Contribution from all the diboson final states (WW, WZ and ZZ) are taken into account and are modelled using the MC@NLO event generator [47] interfaced to JIMMY 4.31 [54] for simulation of the underlying event as done for the top samples.

Inclusive W boson production

Background samples for $W \to e\nu$, $W \to \mu\nu$, and $W \to \tau\nu$ produced in association with jets are simulated using the ALPGEN Monte Carlo program [45]. As for the other samples simulated using ALPGEN (Drell-Yann/Z with additional light and heavy flavor jets) separate samples are used to simulate hard matrix elements for W, $W + c$, and $W + b$ production with additional numbers of partons p in the final state, where p runs from 0 to 5. Again, to remove double counting between the inclusive and the specific c/b-jet samples, the overlap removal procedure based on

Channel	σ (fb)
$ZZ \to \ell\ell qq$	841.5
$ZZ \to \ell\ell\nu\nu$	160.4
$ZZ \to \ell\ell\ell\ell$	27.0
$ZZ \to \ell\ell\tau\tau$	27.0
$ZZ \to \tau\tau\tau\tau$	6.8
$ZZ \to \tau\tau\nu\nu$	80.3
$WW \to \ell\nu\ell\nu$	2012
$WW \to \ell\nu\tau\nu$	2012
$WW \to \tau\nu\tau\nu$	503.0
$WW \to \ell\nu qq$	
$WW \to \tau\nu qq$	
$W^+Z \to \ell\nu qq$	1688.9
$W^+Z \to \ell\nu\ell\ell$	159.2
$W^+Z \to qq\ell\ell$	489.4
$W^+Z \to \tau\nu\ell\ell$	79.6
$W^+Z \to \ell\nu\tau\tau$	79.6
$W^+Z \to \tau\nu\tau\tau$	39.8
$W^+Z \to qq\tau\tau$	249.2
$W^-Z \to \ell\nu qq$	912.6
$W^-Z \to \ell\nu\ell\ell$	86.1
$W^-Z \to qq\ell\ell$	269.3
$W^-Z \to \tau\nu\ell\ell$	43.0
$W^-Z \to \ell\nu\tau\tau$	43.0
$W^-Z \to \tau\nu\tau\tau$	21.5
$W^-Z \to qq\tau\tau$	134.7

Table 5.5. Cross sections for the ZZ samples (where $\ell = e, \mu, \tau$) generated using the MC@NLO Monte Carlo program. The cross section is evaluated in the range $66 < m_{\ell\ell} < 116$ GeV/c^2 from theoretical calculations for ZZ production [55] convoluted with the Z boson branching fractions from [19].

the angular distribution of the heavy-flavor quarks, described in [46] is used. The cross sections, listed in Table 5.6, include a k-factor of 1.20 to make the inclusive W boson production cross section agree with NLO calculations [55].

QCD multijet production

The background from QCD multijet production in both the electron and muon channels is evaluated from the data and is discussed in 5.5.4, since its estimation takes advantage of many selection-related aspects in order to have QCD-enriched samples. This is done since the available Monte Carlo samples may not be very precise in describing the QCD activity, which is expected to be a relevant background for this analysis.

Process	σ(fb)
$W + 0p, W \to e\nu$	8 300 000
$W + 1p, W \to e\nu$	1 560 000
$W + 2p, W \to e\nu$	453 000
$W + 3p, W \to e\nu$	122 000
$W + 4p, W \to e\nu$	30 900
$W + 5p, W \to e\nu$	8 380
$Wb\bar{b} + 0p$	56 800
$Wb\bar{b} + 1p$	42 900
$Wb\bar{b} + 2p$	20 800
$Wb\bar{b} + 3p$	7 960
$Wc\bar{c} + 0p$	153 000
$Wc\bar{c} + 1p$	126 000
$Wc\bar{c} + 2p$	62 500
$Wc\bar{c} + 3p$	20 400
$Wc + 0p$	518 000
$Wc + 1p$	192 000
$Wc + 2p$	51 000
$Wc + 3p$	11 900

Table 5.6. Cross sections for the $W+$jets samples generated using the ALPGEN Monte Carlo program, where p refers to the number of additional partons generated in the matrix element. The cross sections listed include a k-factor of 1.20. The cross sections for $W \to e\nu$, $W \to \mu\nu$, and $W \to \tau\nu$ production are assumed to be the same.

5.2 Object selection

The basic reconstruction of final state particles is explained in the previous chapter. In addition to the ATLAS reconstruction, further cuts and requirements may be applied to take into account the detector conditions and features in order to have good selection efficiency and good quality of the selected objects, as well as to face the requirements imposed by the physical process under study.

The corrections applied to the Monte Carlo samples in order to properly reproduce the data distributions are explained in chapter 4.

In this section the selection requirements are explained and calibration and smearing corrections to be applied to these objects as well as efficiency corrections applied to the Monte Carlo that are directly related to the object selection are discussed.

5.2.1 Muons

In this analysis STACO muons are used, as they are the standard for physics analyses in ATLAS (details are given in chapter 3). Among the muon categories available, combined and segment-tagged muons are chosen in order to have a good background rejection as well as a good reconstruction efficiency over all the p_T spectrum. All muon candidates are required to have $|\eta| < 2.5$ to keep them within the acceptance of the muon spectrometer as well as of the inner detector, and $p_T > 7$ GeV/c.

To ensure high-quality muons and good reconstruction efficiency, additional cuts are imposed on top of the Combined and Segment-Tagged requirements: the inner detector track associated to the muon is required to pass a series of additional cuts based on the number of hits and holes (absence of hits) in the several layers of the inner detector. These requirements are shown in detail in table 5.7. Muons from cosmic rays are suppressed by requiring the impact parameter with respect to the primary vertex satisfy $|d_0| < 1$ mm and $|z_0| < 10$ mm, where d_0 and z_0 are the transverse and longitudinal impact parameters extrapolated at the primary vertex, respectively. To avoid muons associated with jets, such as those originating from semi-leptonic decays of b-hadrons, the candidates are required to be isolated by demanding that the sum of the inner detector track transverse momenta in a cone $\Delta R = \sqrt{\Delta\eta^2 + \Delta\phi^2} < 0.2$ around the muon (ignoring the track associated to the muon itself) be less than 10% of the that of the muon.

Since the background from QCD processes (mostly $b\bar{b}$-pair production) is significant compared to the Drell-Yan pairs even after requiring the muon to be isolated a further rejection of background is obtained by requiring a small impact parameter significance for both muons, $|d_0|/|\sigma_{d_0}| < 3.5$, which maintains a very high efficiency for signal but significantly reduce muons from semi-leptonic b decays. The muon selection is summarized in table 5.7.

As explained in section 4.3, muons p_T is smeared to take into account tiny detector effects by means of a gaussian function whose width is derived from data.

Identification	Combined or segment-tagged STACO muons
Kinematic cuts	$p_T > 7$ GeV/c $\|\eta\| < 2.5$
Inner Detector	$N_{\text{hits}}^{\text{b-layer}} > 0$ (except where the muon passes an uninstrumented/dead area) $N_{\text{hits}}^{\text{pixel}} + N_{\text{dead}}^{\text{pixel}} > 1$ $N_{\text{hits}}^{\text{SCT}} + N_{\text{dead}}^{\text{SCT}} \geq 6$ $N_{\text{holes}}^{\text{pixel}} + N_{\text{holes}}^{\text{SCT}} < 3$ $\|\eta\| < 1.9$: $N_{\text{tot}}^{\text{TRT}} > 5$ and $N_{\text{outliers}}^{\text{TRT}} < 0.9 \times N_{\text{tot}}^{\text{TRT}}$ $\|\eta\| \geq 1.9$: If $N_{\text{tot}}^{\text{TRT}} > 5$, require $N_{\text{outliers}}^{\text{TRT}} < 0.9 \times N_{\text{tot}}^{\text{TRT}}$ where $N_{\text{tot}}^{\text{TRT}} = N_{\text{hits}}^{\text{TRT}} + N_{\text{outliers}}^{\text{TRT}}$
Cosmic rejection	$\|d_0\| < 1$ mm $\|z_0\| < 10$ mm
Track isolation	$\sum_{\text{tracks}} p_T(\Delta R < 0.2)/p_T^{\mu} < 0.1$
Additional QCD suppression	$\|d_0\|/\|\sigma_{d_0}\| < 3.5$

Table 5.7. Summary of muon selection. N_{hits} (N_{holes}) represents the number of hits (missing hits) in a particular subdetector of the inner tracker, while N_{dead} refers to the number of dead sensors crossed by the muon in a particular subdetector

As said above, additional cuts are needed to further reject the QCD multijet events. In the case of muons a substantial component from c- and b-jet is expected due to semileptonic decays of heavy flavor hadrons. In particular a cut on the d_0 significance is applied. Figure 5.1 shows the distribution of the $|d_0|/|\sigma_{d_0}|$ variable

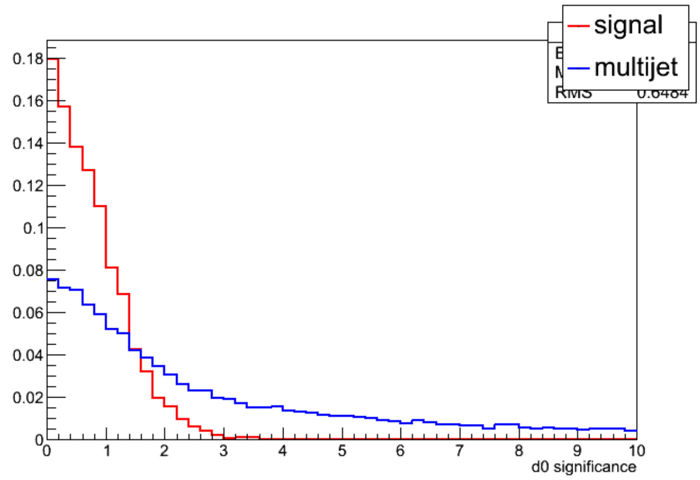

Figure 5.1. Distribution of the d_0 significance of the muons selected applying all the requirements described in tab. 5.7 but the d_0 significance cut. The red line represents the signal sample for $m_H = 130$ GeV/c^2 and the blue line represents the QCD distribution selected as described in 5.5.4

for the signal sample with $m_H = 130$ GeV/c^2 and for the QCD sample selected as described in section 5.5.4. The muons are selected according to the criteria described in table 5.7 with the exception of the $|d_0|/|\sigma_{d_0}|$ cut. The two distribution are normalized to the same area, and it is possible to see how a cut at $|d_0|/|\sigma_{d_0}| < 3.5$ reduces the QCD background without affecting relevantly the signal selection.

The p_T and η distributions of the muons with the selection described below are shown in fig. 5.2. It can be seen that the simulation provides a reasonable description of the data distribution. An absolute normalization of the background components based on the integrated luminosity collected by ATLAS and the generation cross section of the MC samples is used for these plots for all the components except the QCD mutijets. The latter is estimated with data-driven methods described in Sec. 5.5.4. A slight discrepancy in the η distribution, which is more central in the data than in the Monte Carlo, however this is a known feature of the η distribution of leptons from the ALPGEN Z boson production simulation. Moreover, fig. 5.12 demonstrates that in the most relevant sub-sample where the dilepton pair is accompanied by at least two jets the difference between data and simulation is significantly reduced.

5.2.2 Electrons

Among the electron categories available in ATLAS (as explained in 3) in this analysis tight++ electrons are chosen in order to have the maximum background rejection, since the QCD background is expected to give a significant contribution to the final state, as said in chapter 1. Throughout this analysis, the electron's transverse momentum is reconstructed using the energy from the cluster measured in the calorimeter and the direction of the track. The pseudorapidity, η, of the electron is taken from the cluster whenever the candidate's position with respect to the calorimeter is required (for example, in the acceptance selection or in the inputs to

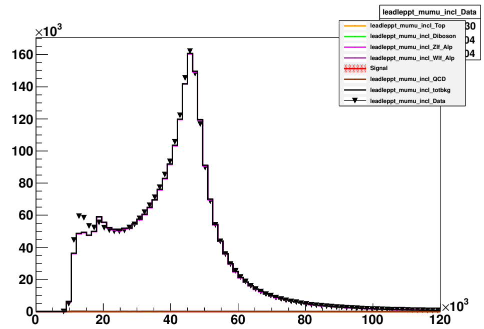

(a)

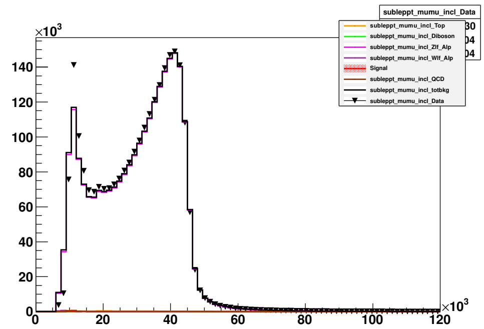

(b)

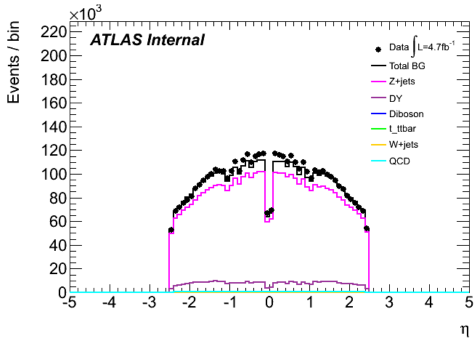

(c)

Figure 5.2. The p_T of the leading 5.2(a) and subleading muon 5.2(b) and η distribution of muon candidates 5.2(c)

the smearing and correction procedure described below) but from the track in all other cases (such as in calculating invariant masses). To ensure a high reconstruction and trigger efficiency, the candidates are required to lie within the pseudorapidity range $|\eta_{\text{cluster}}| < 2.47$, to keep within the region of precision EM measurement, and have a transverse momentum (after energy correction/smearing) $p_T > 7$ GeV/c.

To ensure the electrons are isolated, it is required that the sum of the inner detector track transverse momenta in a cone of $\Delta R < 0.2$ around the electron (excluding the track associated to the electron itself) is less that 10% that of the electron itself.

To avoid double counting and removing some fake electron from muon final state radiations electron candidates that lie within $\Delta R < 0.2$ of a selected muon (as defined above) are rejected.

The selected electrons are required to satisfy all the quality requirements assuring high selection efficiency: differently from muons no additional cuts are needed since all the quality requirements are included into the tight++ selection.

Electrons reconstruction involves both the ID and the calorimetric system, and hence the smearing and the other detector-related corrections should take into account also the measurement of the energy deposit in the calorimeter. In order to do this the standard ATLAS reconstruction includes cell-level energy corrections derived from data. However, residual corrections derived from the entire 2011 data set are available, to be applied at cluster level in order to have a proper energy measurement. These corrections are applied to the electron candidate energies in data and Monte Carlo, and in addition to this, further smearing is applied to reproduce the electron energy resolution and the electron identification efficiency.

Since the background from QCD processes (fakes, conversions and $b\bar{b}$-pair production) is significant compared to the Drell-Yan pairs even after requiring the electrons to be isolated a further rejection of background is obtained by requiring a small impact parameter significance for both electrons, $|d_0|/|\sigma_{d_0}| < 6.5$, which maintain a very high efficiency for signal but reduce electrons background from both semi-leptonic b decays and fakes. The electron selection is summarized in Table 5.8.

Identification	Author: Electron IsEM: tight++
Kinematic cuts	$p_T > 7$ GeV/c $\lvert\eta_{\text{cluster}}\rvert < 2.47$
Track isolation	$\sum_{\text{tracks}} p_T(\Delta R < 0.2)/p_T^e < 0.1$
Additional QCD suppression	$\lvert d_0\rvert/\lvert\sigma_{d_0}\rvert < 6.5$

Table 5.8. Summary of electron selection. The requirements on the intrinsic electron quality are included into the tight++ quality requirement.

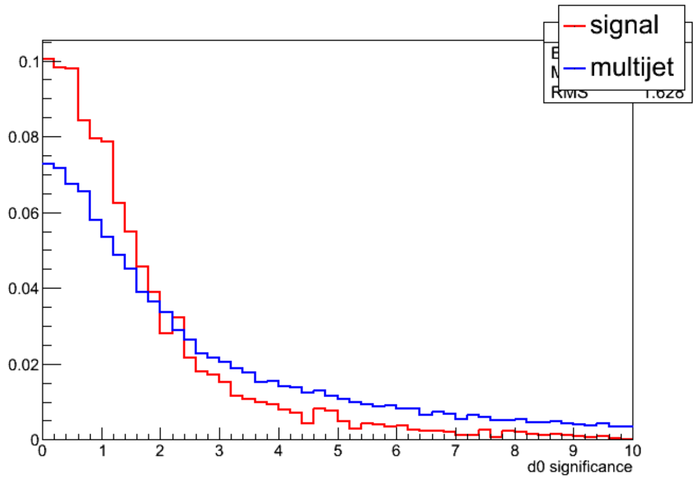

Figure 5.3. Distribution of the d_0 significance of the electrons selected applying all the requirements described in tab. 5.8 but the d_0 significance cut. The red line represents the signal sample for $m_H = 130$ GeV/c^2 and the blue line represents the QCD distribution selected as described in 5.5.4

As for the muons, also for electrons dedicated cuts against the QCD background are needed. In addition to the isolation requirement also in this case a d_0 significance cut is applied. Figure 5.3 shows the distribution of the $|d_0|/|\sigma_{d_0}|$ variable for electrons selected as described above in the signal sample (with $m_H = 130$ GeV/c^2) and in the QCD sample (selected as described in section 5.5.4). It is possible to see how the $|d_0|/|\sigma_{d_0}| < 6.5$ requirement rejects the long tail due to the QCD background saving the most part of the signal.

As it is possible to see comparing fig. 5.3 and 5.1, the distribution of the $|d_0|/|\sigma_{d_0}|$ variable is much broader in the electron channel than in the muon channel. This feature is due to the bremsstrahlung: if an electron radiates a photon, its trajectory is no more circular since part of its energy is carried away from the radiated photon (see fig. 5.4). This effect has an impact on the d_0 significance distribution since the

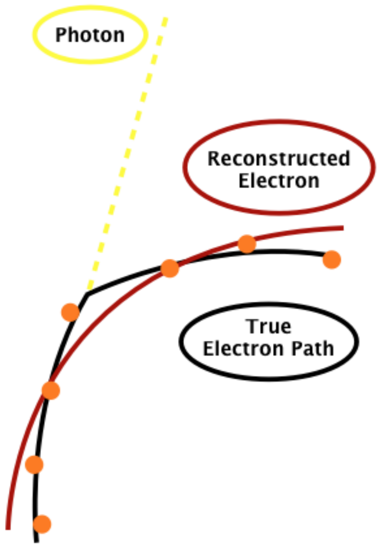

Figure 5.4. Effect of bremsstrahlung on the reconstruction of the electron track: the black line represents the real electron path, which receives a knink from the radiation of a photon (yellow dashed line). The burgundy line represents the reconstructed electron, and the orange markers represent the hits of the electron in the ATLAS Inner Detector

fit on the electron track does not take into account corrections for the bremstrahlung, resulting in a long tail in the distribution shown in fig. 5.3. In ATLAS there is the possibility to use an electron menu which takes into account the correction for the bremsstrahlung, but at the time that the selection for this analysis was optimized there was no possibility to use it, and the expected performances of this analysis in terms of expected limit on the Higgs boson production cross section (see chapter 6 for details) wouldn't have gained so much to justify the introduction of such a correction. Therefore it was decided to use the standard electron menu which does not include corrections for bremsstrahlung.

The bremstrahlung effect is not important in the muon channel (see fig. 5.1) since the cross section for this process is proportional to $1/m^2$, where m is the mass of the particle radiating the photon. So, since $m_\mu \sim 200 \times m_e$ this effect is negligible for muons. A further component populating the high impact parameter tail is of course due to heavy flavor decays as in the muon case, but this component is relatively less important in the electron case than it is in the muon case.

The p_T and η distributions of the electrons selected according to the criteria explained above are shown in figure 5.5. It can be seen that in general the simulation after the corrections provides a reasonable description of the data, although, as in the muon case, there is a mild discrepancy in the η distribution in the central region.

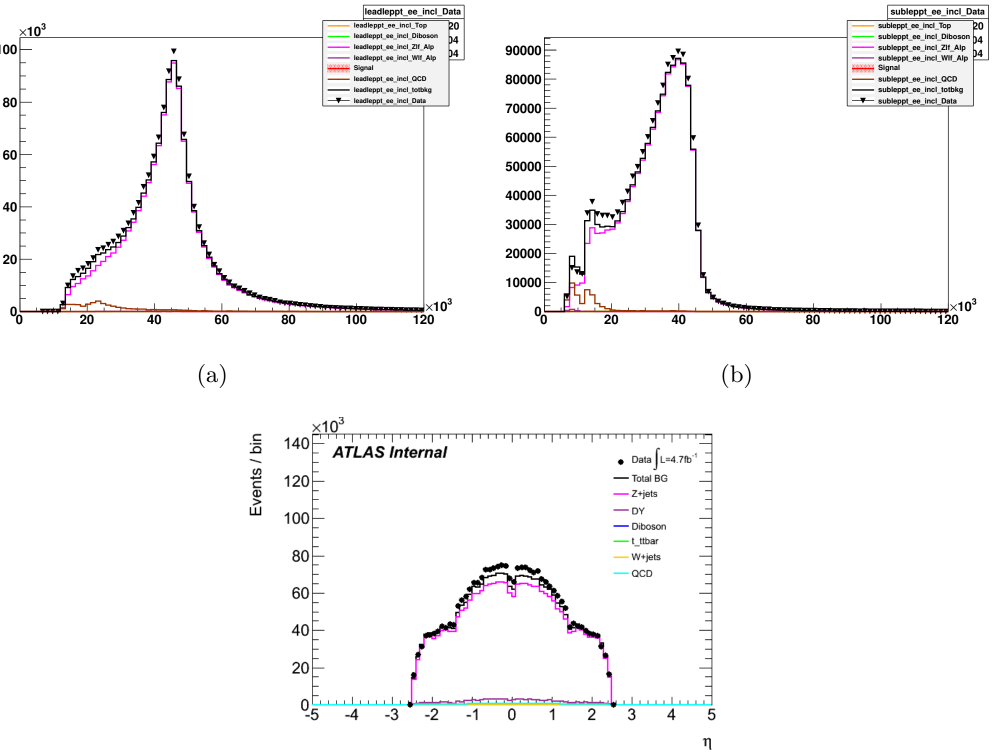

(a) (b)

(c)

Figure 5.5. The p_T of the leading (left) and subleading electron (right) and η distribution of electron candidates (bottom).

5.2.3 Jets

As explained in chapter 3, jets are reconstructed from topological clusters [56] using an anti-k_T algorithm [57] with a distance parameter $R = 0.4$. The jets are required to have $p_T > 20$ GeV/c, and are restricted to $|\eta| < 2.5$, corresponding to the coverage of the ATLAS tracking detector. The jets are required to pass the "looser" quality cuts, which include requirements on the quality of the calorimetric cluster (see chapter 3).

As explained in section 4.1.2 the pileup may affect the jet reconstruction and the selection of the jets. In order to avoid these effects, some handles can be used to favor the selection of jets coming from the real hard interaction identified in the event: since, as explained in section 3.4, tracks reconstructed in the ID are associated to jets according to geometrical closeness, it is possible to apply some requirements on these tracks. For each jet a cut is imposed on the fraction of track momentum associated to it, requiring that at least 75% of these tracks must originate from the primary vertex. This is implemented as a cut on the absolute value of the "jet vertex fraction", $|\mathrm{JVF}| > 0.75$, defined as the fraction of track momentum coming from vertex with respect to the total track momentum. Other than the values between 0 and 1 the JVF variable can also be -1: this is the value it assumes when the jet it refers to has no tracks. Jets with zero tracks may arise from real jets composed of solely neutral particles (which don't leave hits in the ID, and hence have no reconstructed track) or from jets falling in regions where the tracking efficiency is not optimal. Such a region may be the high-η region ($|\eta| \sim 2.5$) which is near to the boundary of the acceptance of the ID. In order not to loose the information carried by jets with zero tracks (which may arise from hadronization of quarks coming from the signal process), also jets having JVF $= -1$ are included in the analysis.

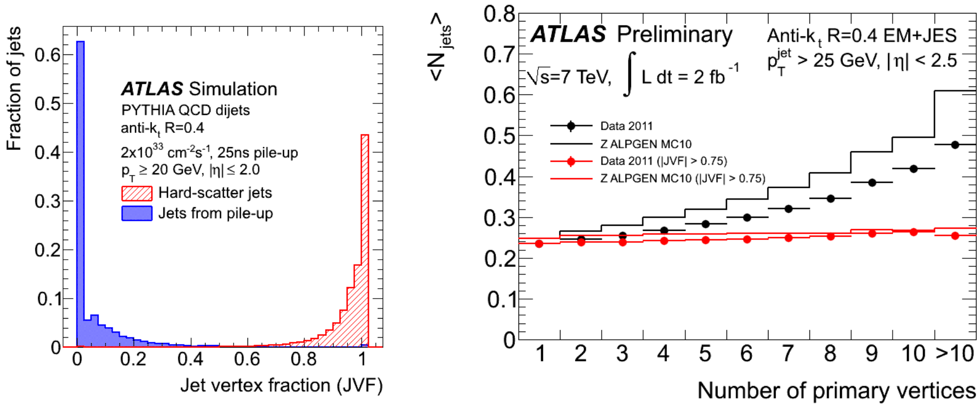

(a) (b)

Figure 5.6. Distribution of the jet vertex fraction (JVF) variable for signal for jets produced in the hard scattering and those produced in the additional pileup interactions 5.6(a) and the impact of the $|\text{JVF}| > 0.75$ cut on jet selection as a function of the number of reconstructed primary vertices 5.6(b)

Figure 5.6(a) shows the distribution of the JVF variable for jets coming from the primary hard scattering and for jets coming from additional interactions coming from pileup, while fig. 5.6(b) shows the impact of the cut we apply on the JVF variable on the mean number of selected jets: if the cut is applied, the number of selected jets remains the same when the number of reconstructed primary vertices increases. This means that the jets arising from the additional vertices due to the pileup are efficiently rejected.

Identification	Anti-k_T $R = 0.4$ topological jets
Kinematic cuts	$p_T > 20$ GeV/c $\|\eta\| < 2.5$
Quality	Looser quality cuts
Pileup	$\|\text{JVF}\| > 0.75$

Table 5.9. Summary of jet selection: the quality cuts are included into the Looser requirement.

To avoid double-counting objects in the event, a jet is removed if an electron satisfying the criteria explained in section 5.2.2 is found within $\Delta R < 0.4$ around the jet axis. The jet selection is summarized in Table 5.9.

The identification of b-jets

As explained in chapter 3, the b-tagging algorithm used in this analysis is MV1, and it is based on three other taggers which rely on the measurement of the d_0 significance, the reconstruction of secondary vertexes and on other features of the b-hadrons.

The working point of the tagger can be chosen by applying a cut on the continuous output value w_{MV1} as shown in fig. 5.7. The chosen value of the cut on the output of the MV1 tagger ensures a b-tagging efficiency of 70% for $t\bar{t}$ events while providing a light jet rejection of $\sim$ 140.

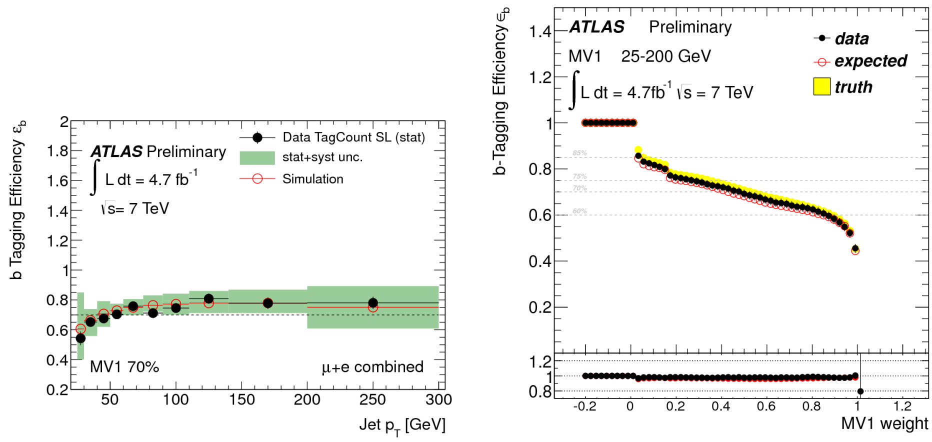

(a) (b)

Figure 5.7. Efficiency of the MV1 tagger as a function of the jet p_T when the 70% efficiency working point is chosen 5.7(a) and the MV1 efficiency as a function of the cut applied on its output value 5.7(b)

Figure 5.7 shows the efficiency of the MV1 tagger as a function of the jet p_T when the 70% efficiency working point is chosen, that is exactly the condition used in this analysis. The efficiency shown in this plot has been measured on a $t\bar{t}$ sample selected in 2011 data sample [38].

Once that the working point is defined (i.e. the nominal efficiency), it is possible to evaluate the scale factors needed in order to have the b-tagging rate in Monte Carlo corresponding to the one observed in data. Fig. 4.4 shows the data-Monte Carlo scale factor as a function of the jet p_T obtained for the 70% efficiency working point used in this analysis.

5.2.4 Missing transverse energy

Missing transverse energy, $E_T^{\rm miss}$, caused by the presence of neutrinos in an event, is an important characteristic to help separate signal from background. Since the $H \to ZZ^* \to \ell^+\ell^- q\bar{q}$ signal has little genuine $E_T^{\rm miss}$, an upper limit on the $E_T^{\rm miss}$ is applied to reduce the background from $t\bar{t}$, single t and Wt events, which are characterized by large $E_T^{\rm miss}$ due to the presence of neutrinos generated in the top quark (or W) decay. Because of this the $E_T^{\rm miss}$ distribution in fig. 5.13 is dominated by top events at high values, and this feature is used to generate a top-enriched sample in order to check the modelization of this background, as explained in detail il section 5.5.2.

The official recommendation in ATLAS for the reconstruction of E_T^{miss} is to use the *RefFinal* algorithm illustrated in section 3.5.

5.3 Event Selection

After having explained how the single final state objects are defined and which additional cuts are applied in this analysis, the full event selection is described in this section. At the beginning specific triggers are required to have fired, then a sample of two leptons and at least two jets is selected with cuts aimed at reducing the background contribution, and a constraint to the Z boson mass is applied to select the jets used to build the $m_{\ell\ell jj}$ distribution is applied.

cut	explanation
Event quality	require that the detector is fully operational and that the reconstructed objects are of good quality
Trigger	lowest-p_T unprescaled triggers are required for both single- and double- lepton configurations
Vertex	require the presence of at least one reconstructed vertex
Lepton selection	exactly two same flavor-opposite sign leptons as defined in sections 5.2.1 and 5.2.2 are required. Their p_T has to be consistent with the trigger thresholds
Missing transverse energy	$E_T^{\text{miss}} < 30$ GeV
Jet selection	at least two jets as defined in section 5.2.3 are required
Dilepton mass	$20 < m_{\ell\ell} < 76\text{GeV}/c^2$
Dijet mass	$66 < m_{jj} < 115\ \text{GeV}/c^2$

Table 5.10. Summary of the cuts applied to select the events used for the final study. Details are given in the following sections

The full event selection is summarized in table 5.10, and details are given throughout the following sections.

5.3.1 Dilepton event selection

The triggers used to select the events among all the recorded ones are single and di-lepton triggers with the lowest unprescaled transverse momentum threshold: the prescales of the triggers change as a function instantaneous luminosity provided by the LHC because the recording rate is fixed by the technology used in the TDAQ system (see chapter 2) while the event rate is expected to increase according to the luminosity. For this reason different trigger thresholds have been used in the different data taking periods in 2011. For single electron triggers the required transverse energy thresholds are 20 GeV in the first period of the data taking (corresponding to $\sim 36\%$ of the total data sample), then raised to 22 GeV ($\sim 13\%$ of the total data sample) and then 22 GeV with stronger quality requirements in the last part of 2011 ($\sim$ 51% of the total data sample). The di-electron trigger used requires two electrons with $E_T > 12$ GeV for all the 2011, but three different quality requirements were implemented during the data taking period (corresponding to $\sim$ 23%, $\sim$ 26% and $\sim$ 51% of the total data sample respectively). The single muon trigger required a p_T threshold of 18 GeV/c for all the 2011 and harsher quality requirements have been asked in the second part of 2011 ($\sim$ 30% and $\sim$ 70% of the total data sample), while the di-muon trigger requires two muons with p_T above 10 GeV/c for all the 2011 without any variation. This trigger combination gives nearly 100% efficiency relative to the offline selection. It is important to remark that the introduction of the dilepton trigger allows to extend the acceptance of the analysis to events containing low-pt leptons. As expained in the following, this is a crucial aspect of this analysis. In particular the choice of using the dilepton triggers in addition to the single-lepton ones brings a relevant increase of the final signal yield: once the full selection described in this chapter is applied, the selected events are increased of $\sim$ 30% in the muon channel and $\sim$ 23% in the electron channel for an Higgs signal with $m_H = 130$ GeV/c^2. Figure 5.8 shows some performances of the triggers used

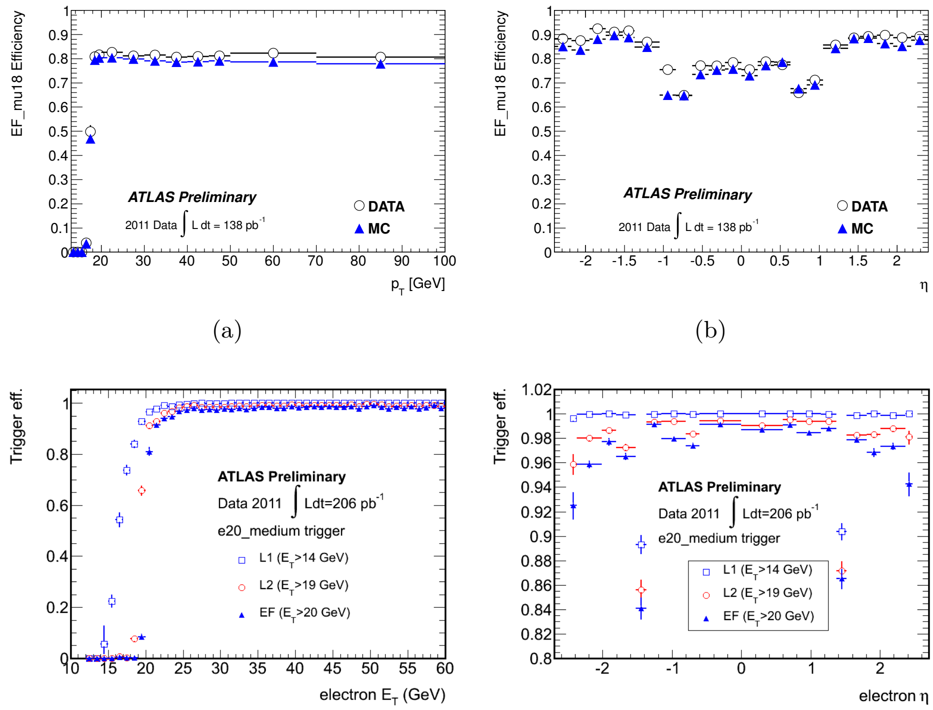

(a) (b) (c) (d)

Figure 5.8. Efficiency of the single lepton trigger used for the analysis: the signle muon trigger efficiency as a function of p_T 5.8(a) and η 5.8(b) and single electron trigger efficiency as a function of E_T 5.8(c) and η 5.8(d). For the electron trigger the efficiencies of the L1 and L2 triggers used to seed the final Event Filter chain are shown too

in this analysis: fig. 5.8(a) shows the efficiency of the single muon trigger which requires the muon p_T to be above 18 GeV/c as a function of the muon p_T, comparing the results obtained for data and Monte Carlo, while fig. 5.8(b) shows the efficiency of the same trigger as a function of η. The two slightly inefficient regions around $|\eta| \sim 1$ correspond to the region where the transition between the central and the forward parts of the ATLAS muon trigger (and spectrometer). Figures 5.8(c) and 5.8(d) show the efficiency of the single electron trigger requiring $E_T > 20$ GeV as a function of electron E_T and η respectively. Also for electrons a slightly inefficient region is found at the transition between the central and the forward calorimeter at $|\eta| \sim 1.5$. In both channels the efficiency is measured with the tag and probe method using events in which a Z bosons decays to leptons (i.e. e and μ).

All triggered events are required to contain at least a reconstructed primary vertex formed from at least three tracks ($p_T > 150$ MeV/c). To remove jets not originating from real in-time energy deposits, which arise from hardware problems, cosmic-ray showers and LHC beam conditions, a jet cleaning cut is applied. In particular, these jets can give rise to fake missing transverse energy leading to undescribed tails in the E_T^{miss} distribution. To avoid this, any event containing a jet with $p_T > 20$ GeV/c which does not satisfy the Looser cleaning criteria explained in chapter 3 is rejected (this is done for both data and Monte Carlo).

Events are required to contain exactly two electrons or muons satisfying the conditions listed in section 5.2. Lepton transverse momenta are required to be consistent with the actual trigger firing in the events: to ensure that the trigger is approximately on the efficiency plateau, minimum lepton p_T is required to be greater than 12(14) GeV/c for both the muons (electrons) in case only the dilepton trigger fired in the event. On the other hand, at least one lepton with p_T greater than 20 GeV/c is required if only the single lepton trigger fired, while the requirement on the second lepton is the minimal 7 GeV/c requirement.

Additional QCD multijet reduction is obtained by requiring that $\Delta R > 0.3$ between any of the selected muons and any of the selected jets, while the ΔR between electrons and jets is required to be greater than 0.4.

The two leptons are required to be oppositely charged in both the muon and electron cases in order to reduce multijet background which produces both same sign and opposite sign pairs. The opposite sign requirement introduce an additional inefficiency ($\sim 1.5\%$) due to charge misidentification, but reduces significantly the QCD multi-jet background. Any event with additional selected (i.e., passing the criteria described in 5.2) leptons of either type is rejected to reduce background from e.g. WZ production.

Since this search is restricted to the low Higgs mass region ($m_H < 200$ GeV/c^2) at least one of the two Z bosons produced in the Higgs decay is expected to be off mass-shell (see fig. 5.9). This implies that the the constraint stemming from the Z boson mass can be employed on just one of the pair (either $\ell\ell$ or $q\bar{q}$). In order to reduce the dominant background coming from Z boson production in association with jets, the $Z \to q\bar{q}$ is chosen to be on mass-shell and the $Z \to \ell\ell$ is chosen to be off mass shell. This requirement makes the Drell-Yan dilepton production in association with jets a relevant background for this analysis, but to reject this contamination the same method used to reject the $Z+$ jets background can be used. This method is explained in the following sections, and it is based on constraining the dijet mass to the Z boson mass minimizing a χ^2 function (more details are given in the following sections).

Given the above, the invariant mass of the lepton pair is chosen to be within the range $20 < m_{\ell\ell} < 76$ GeV/c^2. This suppresses background from events with a real

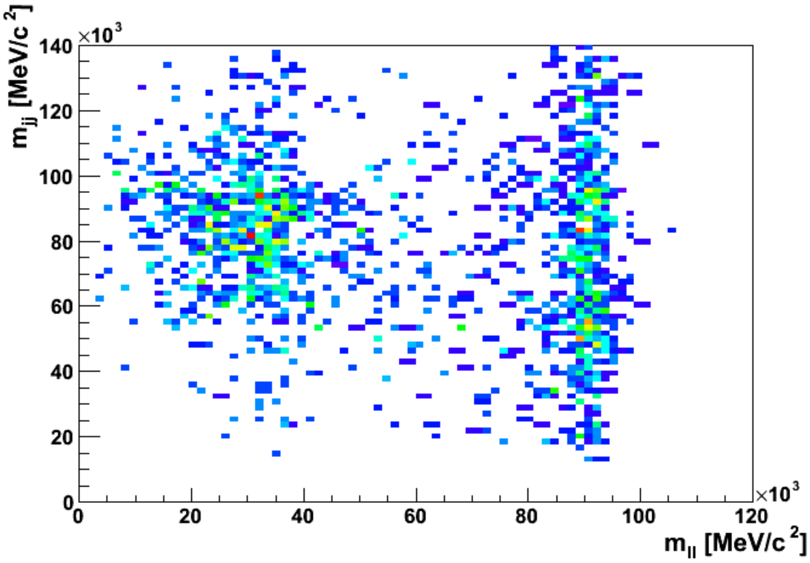

Figure 5.9. Invariant mass of the two leptons and of the two selected jets (see section 5.3.2 for details) in the event for $m_H = 130$ GeV/c^2: at least one of the two Z bosons is expected to be off mass-shell

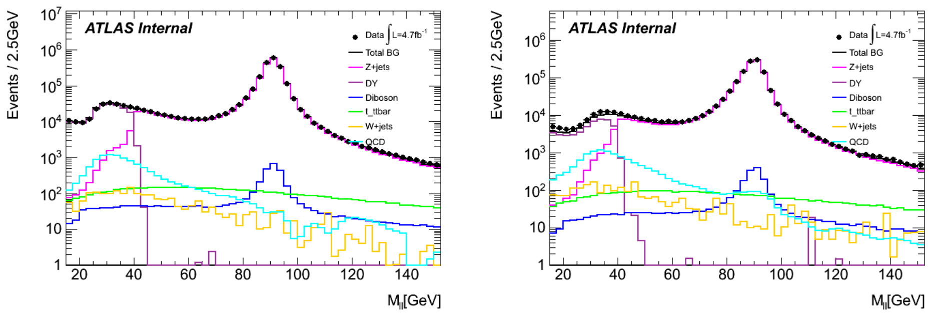

(a) (b)

Figure 5.10. The dilepton invariant mass in the muon 5.10(a) and electron 5.10(b) channels.

Z boson decaying leptonically. The dilepton invariant mass distributions for the electron and muon channels are shown in Fig. 5.10, where the lepton pair is obtained applying the complete selection described above up to the dilepton mass cut. As can be seen, the agreement between data and Monte Carlo is very good over the whole mass spectrum, from few GeV/c^2 up to the Z boson peak and even beyond it. At this stage of the analysis the background estimation is purely Monte Carlo-based for all the samples but QCD: the latter is estimated with data-driven techniques explained in detail in section 5.5.4. This nice agreement is a good starting point for the subsequent event selection.

5.3.2 $H \to ZZ^* \to \ell^+\ell^- q\bar{q}$ selection

Beside the presence of a pair of lepton, $H \to ZZ^* \to \ell^+\ell^- q\bar{q}$ candidates are further characterized by pair of jets resulting from $Z \to q\bar{q}$ decay, hence the presence of at least two jets as defined in section 5.2.3 is required. The jet multiplicities and jet p_T distribution after the dilepton selection are presented in fig. 5.11.

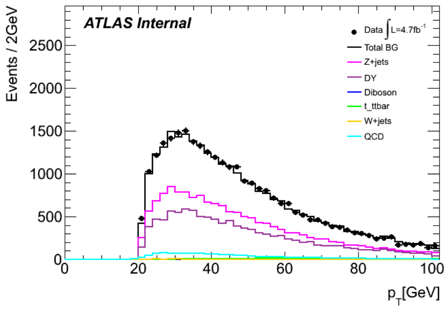

(a)

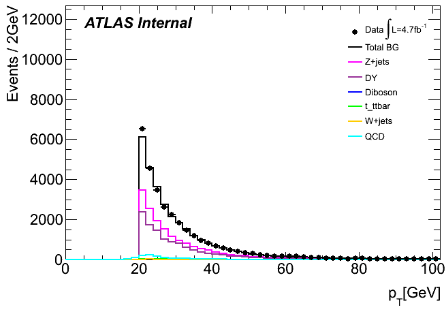

(b)

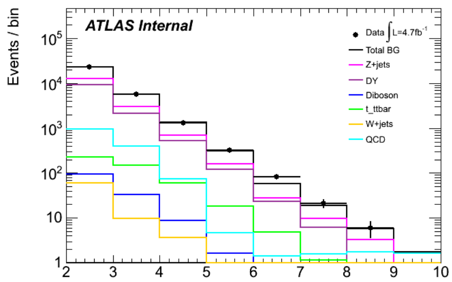

(c)

Figure 5.11. Distribution of the leading jet p_T 5.11(a), subleading jet p_T 5.11(b), and jet multiplicity after dilepton selection 5.11(c) for the combined electron and muon samples.

The lepton kinematic distributions after the dijet selection are displayed in fig. 5.12, showing a good consistency in both p_T and η distributions, thus giving confidence that a proper modelling of the Drell-Yan pairs kinematic can be obtained via the ALPGEN Monte Carlo program.

A missing transverse energy requirement, $E_T^{\text{miss}} < 30$ GeV, is then applied against the background from $t\bar{t}$: this requirement has a limited impact on the signal sample (the $\sim 15\%$ of the signal is discarded) but $\sim 87\%$ of the $t\bar{t}$ events are discarded. The E_T^{miss} distribution is shown in fig. 5.13 after the $m_{\ell\ell}$ and the dijet requirement.

Since about 22% of our signal events contain b-jets coming from $Z \to b\bar{b}$ decay, while b-jets are produced in Drell-Yan/Z processes at a much lower rate ($\mathcal{O}(1\%)$), a big gain in sensitivity is achieved dividing the analysis into a "tagged" subchannel, containing events with exactly two b-tags, and an "untagged" subchannel, containing events with less than two b-tags, while any event with more than two b-tags is rejected. A comparison of the observed distribution of the b-tag discriminant (MV1) to Monte Carlo expectations is shown in fig. 5.15(a) for the leading jet and in fig.

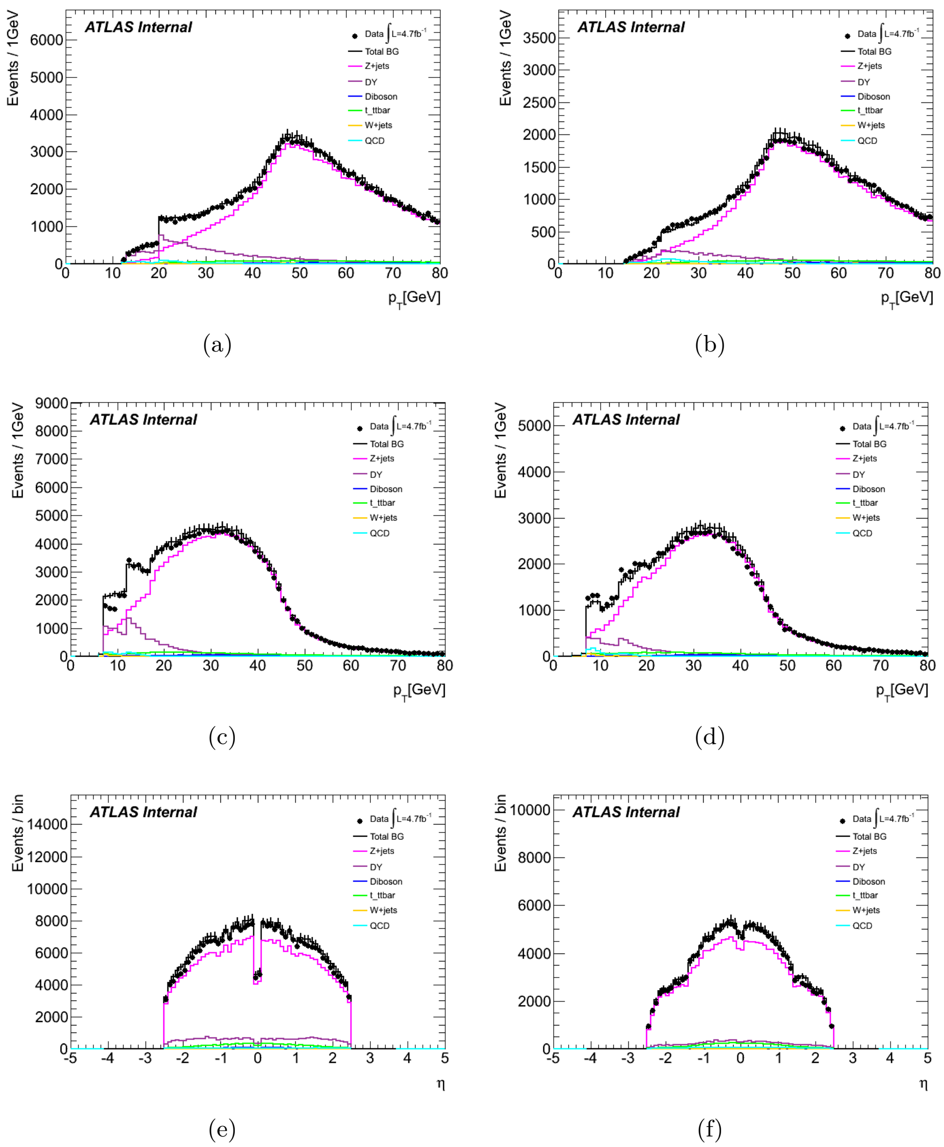

Figure 5.12. The p_T of the leading muon 5.12(a) and electron 5.12(b), subleading muon 5.12(c) and electrons 5.12(d) and the η distribution of muon candidates 5.12(e) and electron candidates 5.12(f) after the ≥ 2 jets requirement

5.15(b) for the subleading one. The multiplicity of the b-tagged jets in the sample selected after the E_T^{miss} requirement is shown too. Di-jet invariant mass are presented in figures 5.16(a) and 5.16(b) for the untagged case and the tagged case respectively.

Since, as shown in fig. 5.14, it is observed that the dijet mass distribution for the tagged jets has a shift with respect to the one of the untagged sample, an additional 5% correction on the jets p_T is applied in order to make the dijet mass for $Z \to b\bar{b}$ events peak at the same value as for the light flavor dominated untagged case [63]. The origin of this mismeasurement of the energy of b-jets is twofold: the semileptonic

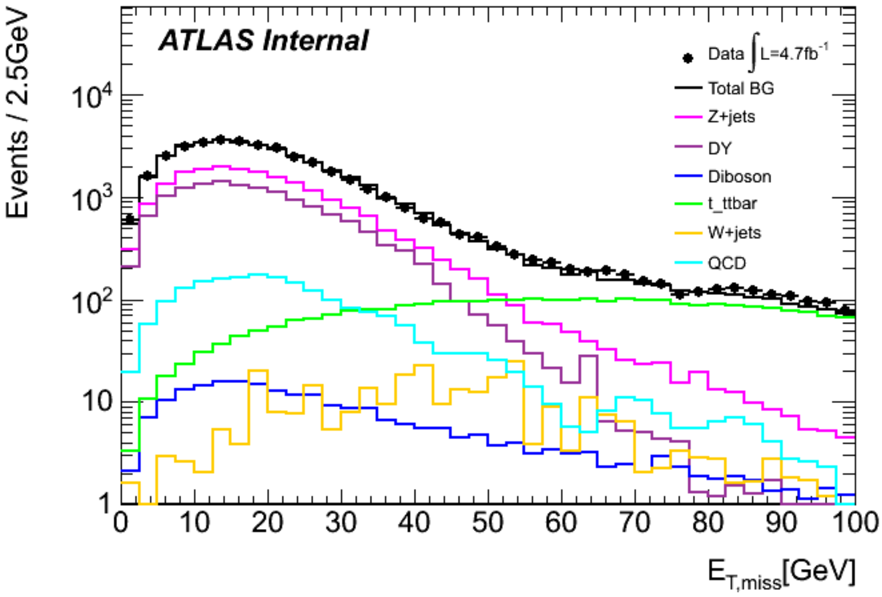

Figure 5.13. Distribution of the E_T^{miss} observed in data compared to Monte Carlo expectations for electrons and muons together

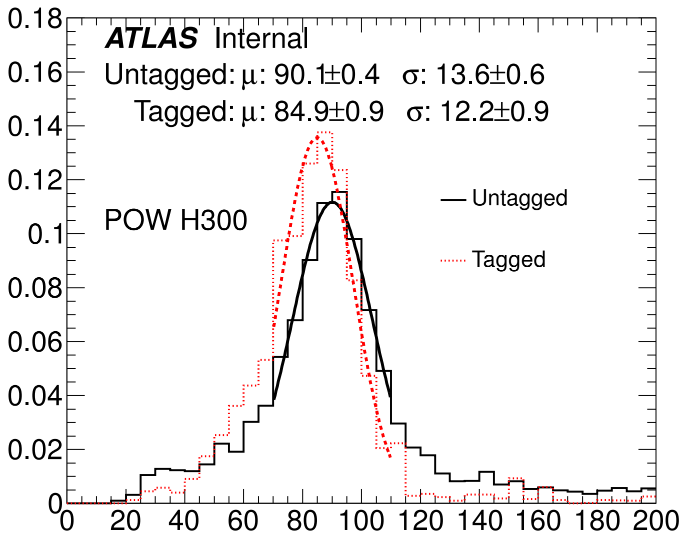

Figure 5.14. Reconstructed mass of the $Z \to b\bar{b}$ process compared to the invariant mass of the $Z \to q\bar{q}$ process. The $Z \to q\bar{q}$ and the $Z \to b\bar{b}$ processes used to build this plot are taken from a sample of Higgs boson with $m_H = 130$ GeV/c^2

decay of the b quark is characterized by the presence of a neutrino coming from the process:

$$b \to q_u + W^- \to q_u + \ell^- + \bar{\nu}$$

where q_u represents a generic up-type quark. The presence of the neutrino leads to undetected energy, and hence to an underestimation of the jet energy. Another and more general effect is due to the fact that in general the hadronization of the b quark is different from that of light quarks, while the jet calibration is usually done on light jet quarks. This leads to a systematic mismeasurement of the energy of jets coming from b quarks. As described above the needed correction can be measured from the displacement of the m_{bb} peak with respect to the one observed in the light quark pairs invariant mass distribution.

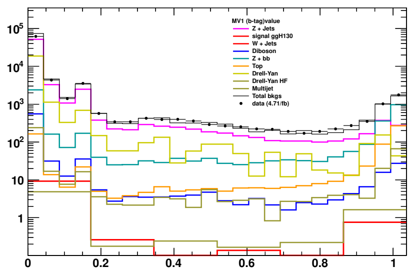

(a)

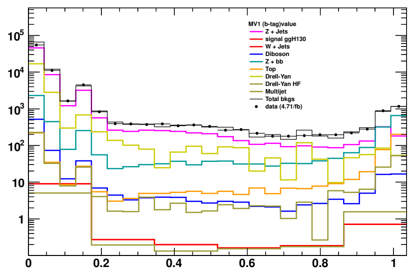

(b)

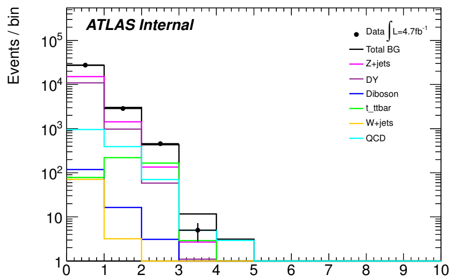

(c)

Figure 5.15. MV1 discriminant for the leading 5.15(a) and subleading jet 5.15(b) and number of b-tagged jet 5.15(c)

The algorithm to choose the jet pairing for the invariant mass calculation is based on a χ^2 minimization using the known Z boson mass as a constraint and varying the jet energies within their uncertainties. The algorithm and its performance are described in the subsequent section 5.3.3. The jet pair with the minimum χ^2 is choosen for the signal selection in the untagged channel, while the in the tagged channel the two b-tagged jets are chosen.

A signal region (SR) and two sideband regions (SB1,SB2) are defined using the invariant mass of the dijet system which minimizes χ^2. The signal region is defined for events where the di-jet system has invariant mass in the range 60 GeV/c^2 $< m_{jj} <$ 115 GeV/c^2. The two sidebands regions are statistically independent from the SR and correspond to the regions below and above the Z-peak region. The low mass sideband, SB1, is defined with 40 GeV/c^2 $< m_{jj} <$ 60 GeV/c^2 while the high mass sideband, SB2, is defined with 115 GeV/c^2 $< m_{jj} <$ 160 GeV/c^2. The two sideband region ranges are chosen such that they give similar event statistics in the two regions. In the following we collectively call SB-region the union of the SB1 and SB2 sidebands.

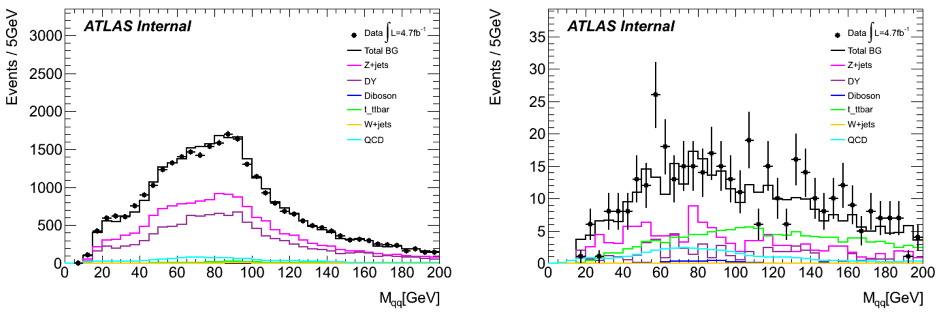

(a) (b)

Figure 5.16. Distributions of the dijet mass after missing energy requirement for the untagged (a) and tagged (b) selection for the combined eletron and muon sample.

Summing up both muon and electron sample, the resulting total analysis selection efficiency for the $H \to ZZ \to \ell\ell qq$ signal increases between 0.7–3% for the untagged selection and 0.05–0.25% for the tagged up to a maximum at roughly 170 GeV/c^2 Higgs mass, dropping somewhat at the high end due to the requirement of an off-shell Z boson decaying to lepton pair. These efficiencies include $Z \to \tau^+\tau^-$ decays. For the individual channels, taking only into account muon and electron decays separately the efficiencies are shown in fig. 5.17(a), 5.17(b), respectively.

5.3.3 Kinematic fit

As said in the previous section, the criterion to select the jets used to build the final $\ell\ell jj$ system among all the jets in the event makes use of a χ^2 minimization. This method aims at selecting the two jets used to build the final $m_{\ell\ell jj}$ distribution taking advantage of the fact that the two jets come from the decay of a Z boson in the signal process, while they don't show a resonant peak for most of the backgrounds (exception is the WZ, ZZ process which is however almost neglibile compared to others).

The basic idea of such a kinematic fit is taken from the studies and measurements performed by the CDF collaboration about the top quark explained in [58]. Some work was needed to adapt the idea to this analysis because of the different final state and physics process being studied.

The χ^2 is built using jet four-momenta, the expected jet energy resolution σ_{jet_i} measured as a function of the jet η and p_T [40] and the world average M_Z and Γ_Z [19]:

$$\chi^2 = \left(\frac{M_Z - m_{jj}}{\Gamma_Z}\right)^2 + \sum_{i=1,2} \frac{(p_{\mathrm{T}_i} - p_{\mathrm{T}_i}^{fit})^2}{\sigma^2_{\mathrm{jet}_i}} \tag{5.1}$$

The χ^2 function is minimized for each jet pair in the event satisfying the jet selection criteria in Table 5.9, varying the jet p_T within the constraint given by the

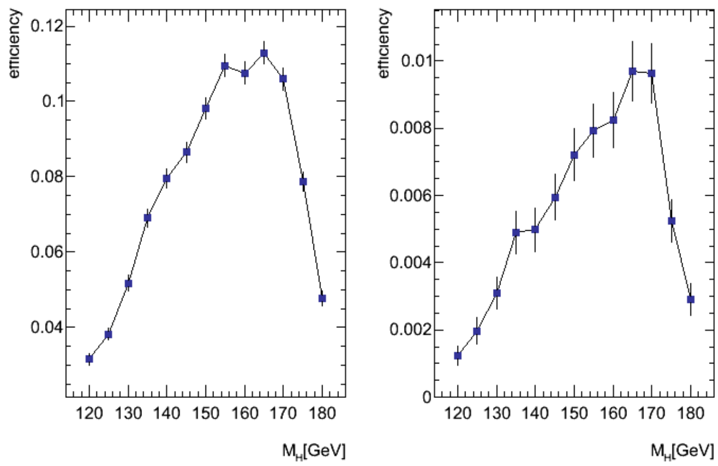

(a)

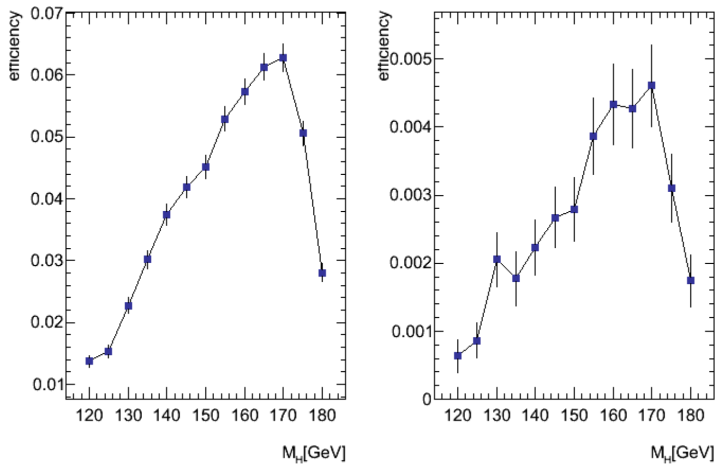

(b)

Figure 5.17. Total efficiency in the electron channel 5.17(b) for the untagged (left) and tagged (right) selections and for the muon channel 5.17(a)

individual jet energy resolution σ_{jet_i}. The jet energy resolution is measured in data with the method described in section 3.4.1 and is parametrized in bins of p_T and η.

The combination which gives the minimum χ^2 is chosen for further analysis. Furthermore, for the purpose of the Higgs mass reconstruction, the $m_{\ell\ell jj}$ is calculated using the p_T corrected according to the fit result. The χ^2 minimization has then a dual purpose: it gives first a criterion for choosing the most likely pair to be produced from the Higgs signal, and it improves significantly the reconstruction of the Higgs mass. When dealing with the untagged channel, this approach allows an efficient reduction of the combinatorial background with respect to the strategy consisting in keeping all jet pairs within some definite mass window, while in the tagged channel (as said in the previous section) the two jets are already chosen to be the two b-tagged jets, and hence the kinematic fit has the only effect of improving the Higgs mass resolution. The distribution of the χ^2 after the dilepton plus at least two jets selection is shown in fig. 5.18, while the improvement in the mass resolution for signal events is demonstrated on the MC simulation in fig. 5.19 for several mass points. The resolution of the event peaking at the right mass is about 2.7 GeV at 130 GeV/c^2 Higgs mass.

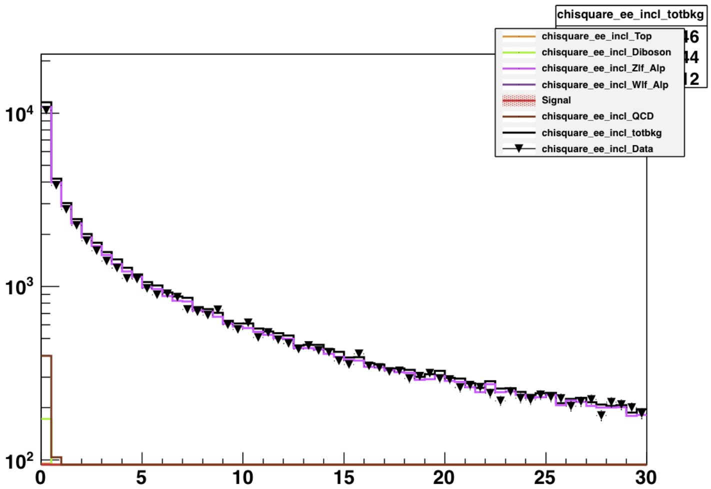

Figure 5.18. The distribution of the χ^2 of the kinematic fitter.

In fig. 5.19 a tail on the high mass side can be seen, specially for lower Higgs masses, even after the action of the kinematic fit. Figure 5.20 shows the distribution of the $m_{\ell\ell}$ variable for the events lying in the tail of the $m_{\ell\ell jj}$ distribution (blue line) and for those lying under the peak. The plot is done using a signal sample with $m_H = 130$ GeV/c^2 and the events are considered in the tail if they are more than 10 GeV/c^2 away from the Higgs boson nominal mass, otherwise they are considered in the peak. From figure 5.20 it is possible to see that the events in the peak of the $m_{\ell\ell jj}$ variable are distributed at very low masses, while the dilepton mass distribution of the events having a large $m_{\ell\ell jj}$ value is much wider. This means that the events having large $m_{\ell\ell jj}$ are composed of a lepton pair with relatively high mass, which means that in this case the Z boson decaying into quarks may not be on-shell. It turns out that the kinematic fit is not effective on this kind of events, and it does not improve the resolution on the $m_{\ell\ell jj}$variable with respect to the raw one.

In principle this effect can be avoided by modifying the $m_{\ell\ell}$ and the m_{jj} widows as a function of the postulated Higgs boson mass both in terms of width and position: fig. 5.20(b) shows the dilepton mass distribution of the events surviving the full selection for three different Higgs boson mass hypotheses: $m_H = 130$ GeV/c^2 in red, $m_H = 150$ GeV/c^2 in blue and $m_H = 170$ GeV/c^2 in green. It can be seen that the dilepton mass window could be optimized as a function of the Higgs mass in order to select only the shoulder present is such a distribution due to the $Z^* \to \ell^+\ell^-$ process, but this have been proved to not have such a big effect on the final significance of the signal. In fact even if an event lies on the tail of the $m_{\ell\ell jj}$ distribution it is still a signal event contributing to the final signal yield. If the dilepton mass window

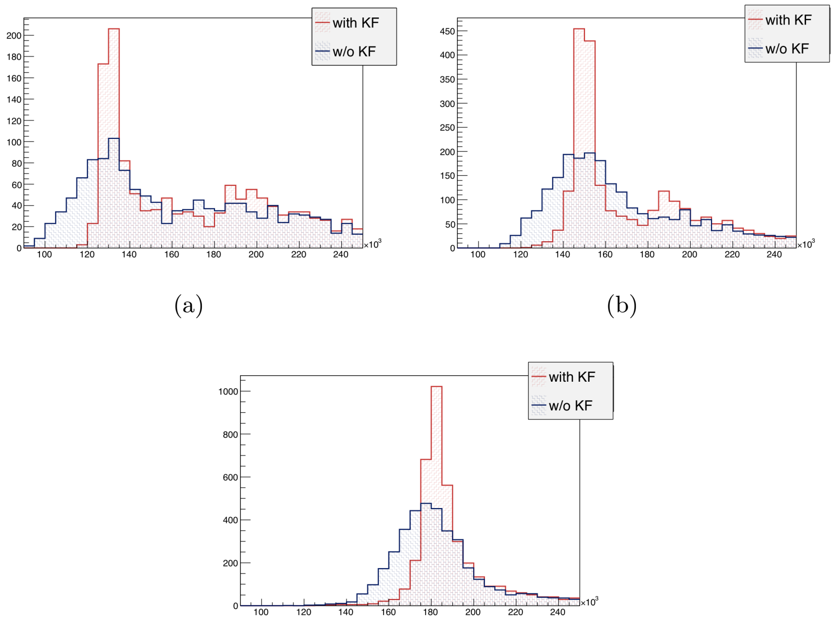

(a) (b)

(c)

Figure 5.19. The distribution of $m_{\ell\ell jj}$ on a signal MC (130 GeV mass) before and after the kinematic fitting for three Higgs mass hypothesis: 130 5.19(a), 150 5.19(b) and 180 GeV/c^2 5.19(c)

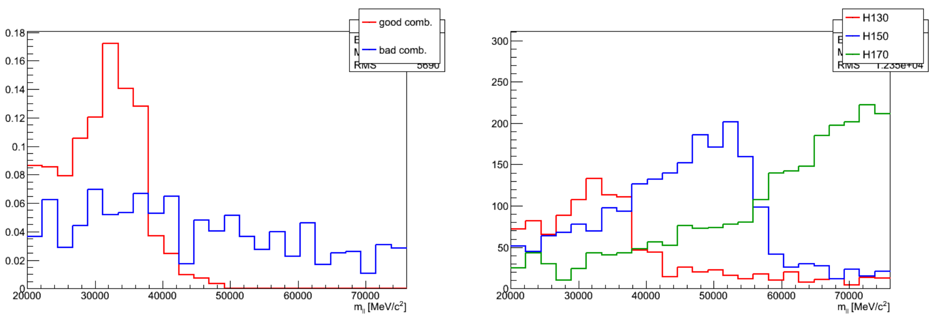

(a) (b)

Figure 5.20. Dilepton invariant mass of events in the tail of the $m_{\ell\ell jj}$ distribution (blue line) and for those in the peak (red line) for an Higgs mass of 130 GeV/c^2 5.20(a); comparison of the $m_{\ell\ell}$ distribution for several Higgs boson masses 5.20(b)

is optimized, for sure a narrower peak for the signal is obtained, but the price for this optimization is a loss of signal events. For this reason we decided to keep the default dilepton mass window $20 < m_{\ell\ell} < 76$ GeV/c^2.

The criterion here proposed to select the jet pair tu be used to build the $Z \to q\bar{q}$ candidate may be compared to other pairing algorithms. In particular this χ^2-based algorithm is one of the innovation introduced with respect to the usual Higgs boson search in the $H \to ZZ \to \ell^+\ell^- q\bar{q}$ decay channel, which is usually performed in the high-mass range ($m_H > 200$ GeV/c^2) [63, 64]. In the high-mass analysis the following jet selection and pairing criterion is used: in each event jets are selected with requirements similar to those explained in section 5.2.3. Starting from this jet collection, all the pairs made using the three leading jets are considered, and a m_{jj} window is applied to each of these dijet systems: all the jet pairs (therefore up to three) passing the $75 < m_{jj} < 105$ GeV/c^2 are taken into account to build the final $m_{\ell\ell jj}$ distribution. Figure 5.21 shows the number of dijet combinations selected in

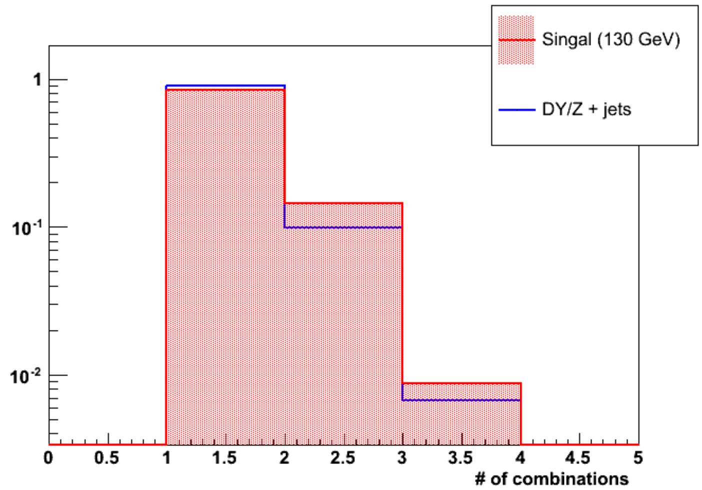

Figure 5.21. Number of dijet combinations contributing to the final $\ell^+\ell^- q\bar{q}$ sample in the high mass-like selection for the signal sample ($m_H = 130$ GeV/c^2) and for the main background

the final sample after the high the selection used in the high mass search. In this figure the signal sample ($m_H = 130$ GeV/c^2) and the DY/Z + jets samples are shown. Finally the dijet systems passing the dijet mass window requirement are scaled to the Z boson mass with the m_{jj}/m_Z factor. The two methods (the one proposed here and the one used in the high-mass analysis) can be compared in terms of both efficiency on the signal sample and resolution on the $m_{\ell\ell jj}$ variable. The resolution on the $m_{\ell\ell jj}$ variable is measured fitting the peak reconstructed Higgs peak with a Gaussian function. This is done separately for the two selections and then the widths of the two Gaussians are compared. Figure 5.22 shows the two fits performed on the peak of the $m_{\ell\ell jj}$ variable after the two different selections: fig. 5.22(b) is the fit after the χ^2-based selection used in this analysis and fig. 5.22(c) is the analogous fit after the event selection done as in the high-mass $H \to ZZ \to \ell^+\ell^- q\bar{q}$ search, while fig. 5.22(a) shows the comparison between the $m_{\ell\ell jj}$ spectra obtained with the two selections. In particular, in order to compare the same events and hence having a real measurement of the resolution that it is possible to obtain with the two methods, in the high mass selection only one combination is taken: among the available combinations, the one with the two hardest leading jet is taken. Moreover the same dijet mass window $70 < m_{jj} < 105$ GeV/c^2 is applied. The results of the fits are shown in table 5.11 for a signal sample with $m_H = 130$ GeV/c^2. From the numbers in tab. 5.11 it is possible to see that the results of the two fits are similar, but the kinematic fit provides better reconstruction of the Higgs boson mass.

Another comparison between the two methods can be done applying the two full

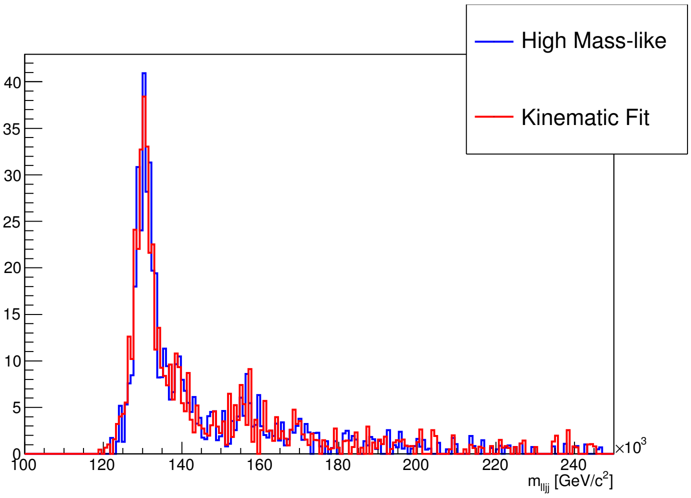

(a)

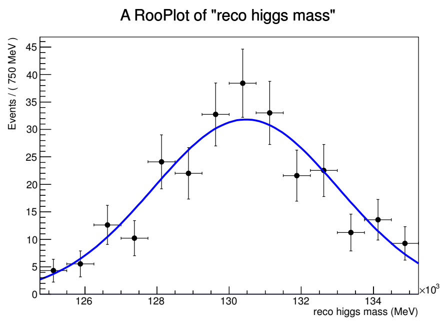

(b)

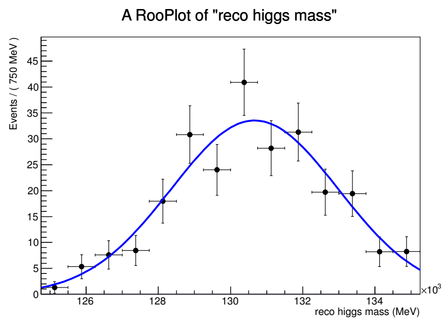

(c)

Figure 5.22. Comparison of the $m_{\ell\ell jj}$ spectra obtained with the two different selections 5.22(a) and fits to the core of the $m_{\ell\ell jj}$ distribution for the χ^2-based selection 5.22(b) and for an "high mass-like" selction 5.22(c)

	kinematic fit	high-mass sel.
μ (GeV/c^2)	130.1 ± 0.1	130.4 ± 0.1
σ (GeV/c^2)	2.7 ± 0.1	2.8 ± 0.1

Table 5.11. Results of the fits performed on the Higgs boson mass peak reconstructed with the two different methods. The corresponding plots are shown in fig. 5.22

selections to both signal and background samples, and then extract the significance from the obtained yields. In order to evaluate the impact of the two methods on the peak of the signal, a 10 GeV/c^2 window around the nominal Higgs boson mass is used. In table 5.12 the significances obtained with the two methods in the electron and muon channels separately are shown as well as the result obtained considering electrons and muons together. The significance is evaluated using the formula:

$$\text{significance} = \sqrt{2 \times \left((s+b) \times \log\left(1 + \frac{s}{b}\right) - s \right)} \tag{5.2}$$

selection	significance (%)		significance ($e + \mu$) (%)
	e	μ	
high mass	5.8	7.4	8.9
kinematic fit	10.1	9.3	13.7

Table 5.12. Significance obtained for the two methods in the electron and muon separately. The last column shows the significance obtained merging the two samples. The significance is calculated with formula 5.2

where s and b are the signal and background yields evaluated respectively. As can be seen from table 5.12, the jet pairing algorithm based on the kinematic fit gives much better significance with respect to the method used in the high-mass search. Since, as shown in table 5.11, the two methods give similar resolution on the signal sample, the gain in significance obtained with the kinematic fit comes mainly from the better background rejection. This derives from the fact that for in the kinematic fit-based method up to one dijet combination per event is taken into account, while in the high mass selection several dijet combinations found in the same event may contribute to the final sample (see fig. 5.21 for details).

5.4 Event weight

In order to have a Monte Carlo simulation which properly reproduces the data many corrections have to be taken into account. There are two types of correction: the corrections on the kinematic variables of the reconstructed particles (leptons, jets) due to detector features not properly reproduced in the Monte Carlo simulation (e.g. misalignments) are explained in section 4.3, and the corrections arising from different performances of algorithms (such as trigger or b-tagging) on Monte Carlo and data as can be seen as an example in fig. 5.8 or fig. 5.7, where little differences between the efficiencies measured in data and Monte Carlo can be seen. Each of these corrections is evaluated as a weight for the Monte Carlo event, and each weight depends on the intrinsic features of the correction itself: as an example (as explained in section 5.2.3) the b-tagging scale factor depends on the true flavor of the jet, on the weight that the tagger assigns to that jet and on the η and p_T of the jet itself. The corrections taken into account are due to:

- reconstruction of final state physics objects
- trigger
- b-tagging (the global event weight is obtained multiplying the scale factor for each jet)
- Higgs boson p_T (to make it agree with the latest calculation, only for the signal sample via gluon fusion)
- pileup
- Monte Carlo weight: some Monte Carlo samples (MC@NLO) have an intrinsic weight which takes into account higher order calculations

The scale factors coming from the several sources listed above are combined in a single scale factor for the whole event just multiplying them together, and the resulting scale factor is used as a weight for the Monte Carlo event.

5.5 Backgrounds

The main backgrounds are discussed in this section. The dominant background is expected to be from Drell-Yan/Z + jets events, with multijet and top production events contributing significantly. Data driven methods are used to determine or control these backgrounds. Smaller contributions are expected from diboson production which are estimated using Monte Carlo simulation. Finally the small contribution of W + jets events is estimated through simulation, but possible discrepancies are covered in the data driven multijet background estimation.

5.5.1 Drell-Yan/Z + jets background

Drell-Yan and Z + jets is the dominant background in the untagged case, while the Drell-Yan and Z+ heavy jets process has the higher contribution in the tagged case, and, as said in section 5.1, ALPGEN Monte Carlo is used to model them. Anyway, ALPGEN is a LO Monte Carlo and processes with jets are notoriously difficult to predict, therefore uncertainties on their cross sections are large, and because of this it is convenient to constrain both the overall normalization and the shape of the Drell-Yan and Z + jets using ad hoc control regions. The control regions for the Drell-Yan/Z + jets background are the side bands of the m_{jj} window required in the analysis (defined in the previous section), and the check is performed building the final $m_{\ell\ell jj}$ distribution replacing the nominal m_{jj} window cut with the requirements that the dijet mass lies in the sideband region. At the end of the selection the data and Monte Carlo expectations are compared. As for the DY/Z + jets, also the normalization of the top background in the tagged case is estimated from a control region (details are given in section 5.5.2). During the procedure to obtain the sample normalization the other backgrounds are subtracted from data, and hence the result found for a given sample (say the DY/Z + jets) may affect the normalization of the other sample (sat top) and viceversa. In order to avoid this effect, the normalizations of the DY/Z + jets and top backgrounds are performed in parallel using an iterative estimation. In addition to this, a systematic uncertainty to take into account this correlation is used, as described in detail in section 6.1. Due to the low available number of events in the tagged case, the electron and the muons channels are considered together.

Several systematic checks are performed to verify the robustness of the method and estimate the uncertainties of its application: separate estimates are calculated from the low and the high m_{jj} side bands and the size of the side bands as well as the mass window positions are altered in order to check the stability of the resulting scale factor. Figure 5.23 presents the comparison between data and simulation for the contribution of the DY/Z + jets background. The obtained scale factors are found to be:

Untagged electron:	$1.02 \pm 0.03 \pm 0.02$
Untagged muon:	$0.99 \pm 0.02 \pm 0.04$
Tagged:	$1.22 \pm 0.13 \pm 0.12$

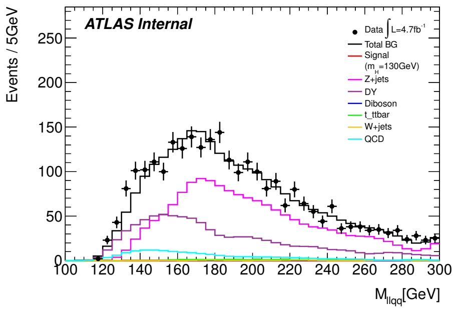

(a)

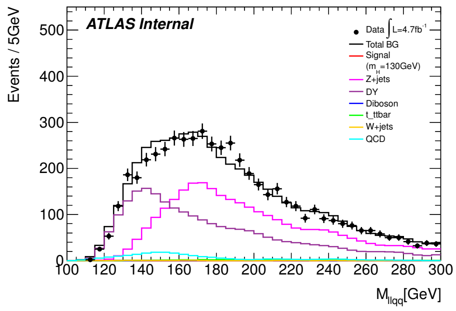

(b)

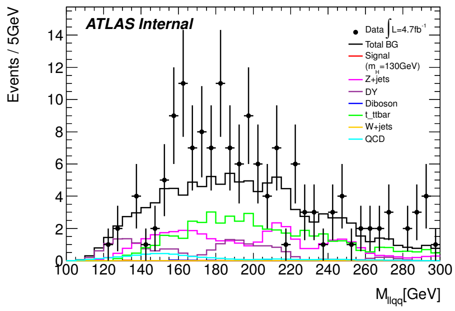

(c)

Figure 5.23. Comparison between data and simulation for the contribution of $DY + \text{jets}$ background, estimated from the m_{jj} side bands, before the application of the scale factor. 5.23(a) and 5.23(b) correspond to the electron and muon channel respectively of the untagged case and 5.23(c) to the tagged case for both channels together

The above scale factors are obtained as the ratio between the data from which all the background contributions but the DY$/Z + \text{jets}$ are subtracted and the DY$/Z + \text{jets}$ background itself as it is obtained by the fully Monte Carlo-based estimation. It is worth to remark that figure 5.23 shows a very good agreement between data and Monte Carlo. This is confirmed by the scale factors which are consistent with one within the errors. The systematic uncertainty in the untagged case receives contributions both from the multijet subtraction and the variation of the side band windows. In the tagged case the systematic uncertainty is dominated by the uncertainty on the subtracted contributions of top and multijet backgrounds.

5.5.2 Top background

Top production constitutes a significant background in the tagged case and gives also a small contribution in the untagged case. This background is dominated by leptonic $t\bar{t}$ decays in which the leptons originate either from the W boson decays or the b-jets from the top quark decays as shown in chapter 1. The presence of neutrinos in the leptonic decays of $t\bar{t}$ leads to large values of missing transverse energy. Therefore, the requirement of low missing energy (see 5.3.1) reduces this background considerably. The isolation requirement on the leptons reduces further the contribution of leptons originating from hadrons in the top decays.

As for the DY/Z + jets background, also the top normalization is estimated from data, studying the control region obtained by inverting the $E_T^{\rm miss}$ requirement ($E_T^{\rm miss} > 40$ GeV). The inverted $E_T^{\rm miss}$ control region of the tagged case is dominated by top decays, receiving a small contribution (of 4%) from multijet events which is estimated with the *ABCD method* described below.

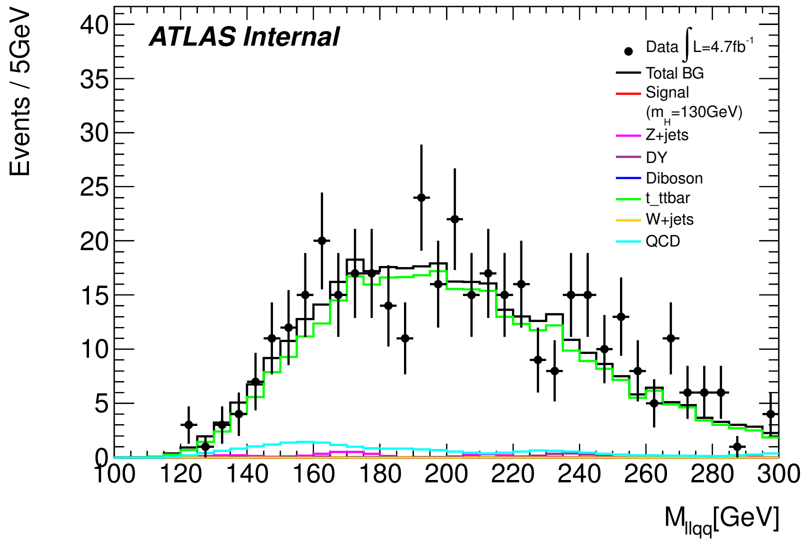

Figure 5.24. Comparison between data and simulation for the contribution of top background in the tagged sample, estimated from the inverted $E_T^{\rm miss}$ control region, before the application of the scale factor

The comparison between data and simulation for the top background contribution in the tagged sample computed from the inverted $E_T^{\rm miss}$ control region is presented in fig. 5.24, and the scale factor obtained from this comparison is the following:

$$\text{Tagged:} \quad 1.09 \pm 0.06 \pm 0.04$$

where the first error is statistical and the second systematic. As for the DY/Z + jets background, a good agreement is found between data and purely Monte Carlo-based estimation. This is confirmed by the obtained scale factor which is found to be consistent with unity. Nevertheless this scale factor is applied to the top quark background estimation for the subsequent studies. As can be seen, the dominant systematic contribution arises from the subtraction of the other processes in the control region. The DY/Z + jets in the untagged case and the multijet background in the tagged case. The calculation of the systematic uncertainty is explained in section 5.6.

5.5.3 Diboson background

The Standard Model ZZ background process is difficult to constrain from data in the $H \to ZZ^* \to \ell^+\ell^- q\bar{q}$channel because of the large DY/Z + jets background and possible contamination from the signal. Anyway even if the Standard Model $ZZ \to \ell^+\ell^- q\bar{q}$ process is the only irreducible background, it turns out to be not so important in this analysis since the huge contribution from the DY/Z + jets production. Hence in this analysis it is completely estimated from the Monte Carlo simulation. An additional small background from WZ production, which is dominated by the case in which the Z boson decays leptonically and the W boson decays hadronically. This background is also estimated from Monte Carlo simulation as well as the WW process, which is expected to give an even smaller contribution.

5.5.4 Multijet background

The multijet background is significant in the low mass dilepton region where this search is performed, and since this background is notoriously difficult to model, we adopt two distinct data-driven methods to evaluate both its size and the shape for the final analysis. Some general remarks valid for both the methods have do be given before going through the details of the estimation of this background: in general many QCD-enriched samples are available (details for each channel are given in the following paragraphs), and therefore the choice of the default one may be an issue. To overcome this problem quality checks have been performed on the several samples and the ones used as default resulted to be the best ones in terms of statistical tests performed using the two methods. Additional details on these statistical tests are given in the sections explaining the two methods. It is worth to remark that the choice of the default QCD samples performed independently for the two methods gave the same results for both the muon and electron channel.

Another issue that may affect the multijet background background is the low statistics of the tagged sample, since the QCD templates are taken from data, which usually have much less statistics than the Monte Carlo samples. For this reason the same shape is assumed for both the tagged and the untagged case, which is the one provided by the final selection without splitting the events in the tagged/untagged categories, while the normalization is estimated separately for the two subsamples, measuring the tagged event rate in the QCD-enriched samples.

Multijet background estimation using a template fit method

The template method aims at taking the multijet background estimation from data. The shape of the background is obtained from a sample dominated by multijets and then subsequently normalized to the signal selection.

The normalization of this multijet sample is estimated by fitting the dilepton invariant mass spectrum after applying the nominal selection up to the requirement of ≥ 2 jets. This is performed over the mass range $15 < m_{\ell\ell} < 120$ GeV/c^2 using two components to fit the data distribution:

- The multijet template derived from data using an ad hoc selection (see the following for details in each channel)
- The sum of all the others contributions (including the signal sample) obtained with Monte Carlo simulations with the nominal selection up to the ≥ 2 jets requirement.

The result of the fit is a scale factor that has to be applied to the multijet sample in order to let it have the right normalization with respect to the data sample.

After the fit is performed, the quality of the result can be checked looking at the obtained χ^2. The default QCD template is chosen among the available ones as the one for which the template fit gives the best χ^2. In the following paragraphs the tested templates are listed for each channel.

Application of the template fit method for the dimuon sample The sample used for the template fit method in the muon channel are the following:

- same sign muon pairs, with all the isolation and quality requirements were left unchanged
- opposite-sign muon pairs, inverting the isolation requirement on at least one of the two

The first sample is used as default since it gives a better χ^2 when used for the fit, while the second is used for the systematic studies on both normalization and shape of the QCD background shown in the following. The fit is performed on the dimuon mass distribution obtained after the missing energy and the two jets requirements. The result extrapolated to the dilepton signal region ($20 < m_{\ell\ell} < 76$ GeV/c^2) corresponds to a fraction of QCD multijet events with respect to the selected number of data events for both tagged and untagged samples. The normalization of the tagged sample is obtained adding the request of exactly two tagged jets. The results obtained are the following:

$$\begin{aligned} \text{untagged:} &\quad [4.3 \pm 1.0 \text{ (stat)}]\% \\ \text{tagged:} &\quad [10.9 \pm 2.8 \text{ (stat)}]\% \end{aligned}$$

The considerably higher QCD multijet background in the tagged sample is attributed by an increased proportion of heavy flavour decays in the muon multijet sample naturally leading to an higher tagging rate. In both the samples the systematic contribution to the uncertainty due to the variation of the sample is negligible.

Besides the normalization it is important to establish also the expected $m_{\ell\ell jj}$ shape for this background. To do this the two multijet-enriched selections have been compared and, as can be seen from fig. 5.25(a), the impact on the $m_{\ell\ell jj}$ modelling of either of the choices is limited.

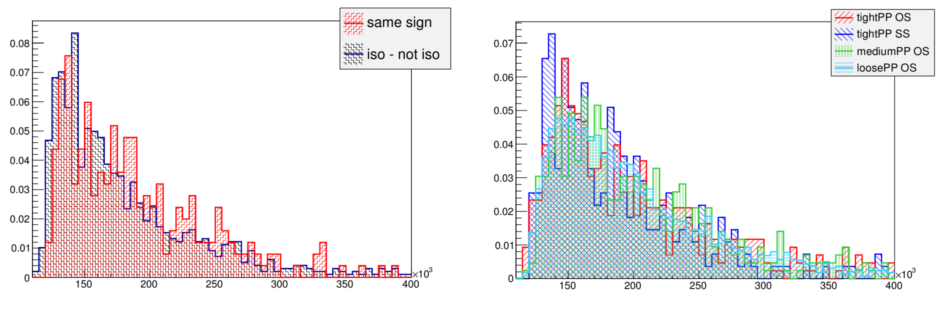

(a) (b)

Figure 5.25. Comparison of the $m_{\ell\ell jj}$ distribution for two different selection of QCD dominated control regions for muon sample 5.25(a), and electron sample 5.25(b)

Application of the template fit method for the di-electron sample The multijet samples used in the dielectron channel can be obtained varying the sign and the isolation of the pairs (as in the muon channel), but in the electron channel also the quality of the reconstructed electrons can be varied. The QCD-enriched samples used in this study are:

- tight++, opposite sign pairs, in which exactly one of the two electrons is required to be isolated and the other one anti-isolated
- tight++, same sign pairs, one isolated electron and the other anti-isolated
- medium++ (excluding tight++), opposite sign pairs with the same isolation requirements as above
- loose++ (excluding medium++), opposite sign with the same isolation requirements as above

Among the above samples, the first one is used as default, while the others are used for systematic variations. The resulting QCD fraction in the dilepton signal region is:

$$\begin{aligned} \text{untagged:} \quad & [12.0 \pm 1.4 \text{ (stat) } \pm 2.3 \text{ (syst)}]\% \\ \text{tagged:} \quad & [11.9 \pm 2.9 \text{ (stat) } \pm 1.6 \text{ (syst)}]\% \end{aligned}$$

The systematic uncertainty is quoted from the maximum difference of the fit result obtained using the other templates described above. The dilepton mass distribution after the template fit is shown for electron and muons in Fig. 5.26.

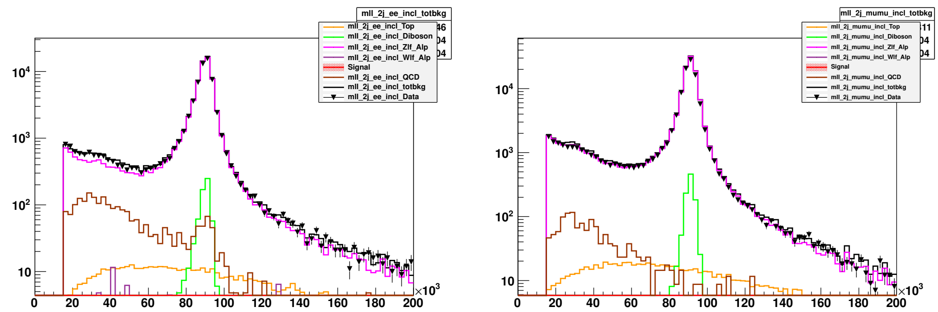

(a) (b)

Figure 5.26. The distribution of the dilepton mass used for QCD fit: 5.26(a) for electrons and 5.26(b) for muons

As for the dimuon cases a comparison of the $m_{\ell\ell jj}$ shape obtained with different selections aimed at enhancing the contribution of QCD multijet fakes is shown in fig. 5.25(b).

Background estimation using an ABCD method

The other procedure that is used to estimate the QCD background is the ABCD method, based on modified charge and isolation criteria for the selected leptons. In particular, we define the four regions:

A: events with leptons of opposite charge, both isolated
B: events with leptons of opposite charge, one isolated one non isolated
C: events with leptons of same charge, both isolated
D: events with leptons of same charge, one isolated one non isolated

where A is the "signal region" and regions B, C and D are dominated by multijet processes. Considering there is no correlation between the charge and isolation requirements, we can estimate the expected number of multijet events in signal region A from the number of multijet events in regions B, C and D, assuming the ABCD relation A = B × (C/D) within statistical uncertainty. To perform the calculation, a profile-likelihood approach is used. Denoting the unknown number of multijet events in region A as μ_U, we can express the number of multijet events in each region by introducing two nuisance parameters τ_B , τ_C:

A: μ^U
B: $\mu^U \tau_B$
C: $\mu^U \tau_C$
D: $\mu^U \tau_B \tau_C$

The corresponding total events in each of the regions are then:

$$
\begin{aligned}
\mu^A &= s^A + b^A + \mu^U \\
\mu^B &= s^B + b^B + \mu^U \tau_B \\
\mu^C &= s^C + b^C + \mu^U \tau_C \\
\mu^D &= s^D + b^D + \mu^U \tau_B \tau_C
\end{aligned}
$$

where $s^{A,B,C,D}$ and $b^{A,B,C,D}$ are the known contributions from signal and electroweak background processes in each region. The likelihood function is the product of the four likelihoods for the counting experiments in the four regions:

$$L(n_A, n_B, n_C, n_D \mid \mu^U, \tau_B, \tau_C) = \prod_{i=A,B,C,D} \frac{e^{-\mu_i} \mu_i^{n_i}}{n_i!} \tag{5.3}$$

The parameter of interest μ^U and the nuisance parameters τ_B,τ_C are calculated from the minimization of $\log L$. Therefore, the application of the ABCD method provides the normalization of the multijet background in the signal region.

Once the normalization is found, it has to be applied to a template used to model the shape of the QCD background. As said above several templates are available to model the QCD shape in both muon and electron channels. Among the available samples, the default ones in the two channels are chosen as follows: the data-Monte Carlo agreement in both signal region and m_{jj} sidebands is probed performing Kolmogorov-Smirnov tests. The samples with the best Kolmogorov-Smirnov probability are chosen as default, and the others are used for systematic variations.

Application of the ABCD method for the dimuon sample As described in the previous section, the application of the ABCD method defines the normalization of the multijet background in the signal region. The second ingredient needed for the complete background estimation is the shape of the corresponding background. Also using this approach the samples listed in 5.5.4 are used for default and systematic variations.

The statistical uncertainty on the evaluation of the multijet background is determined by the number of events of the B, C and D regions. Systematic uncertainties include either uncertainties on the normalization or the shape of the distributions. The statistical accuracy of the method is found to be 8% and 40% for the untagged and the tagged case respectively. As a measure of the shape uncertainty, the distributions corresponding to the m_{jj} side bands are used instead of the ones corresponding to the signal region. To estimate the normalization uncertainties, the normalization of the multijet background is estimated at different stages of the event selection. In addition different control regions are studied as a function of the muon "anti-isolation" condition imposed. Adding these contributions in quadrature an estimate of 10% and 34% is found for the untagged and the tagged case respectively.

The final estimate for the QCD multijet background percentage over the total in the dimuon case, is thus estimated as:

$$\begin{aligned} \text{untagged:} &\quad 3.49 \pm 0.24 \pm 0.35\% \\ \text{tagged:} &\quad 11.0 \pm 4.4 \pm 3.7\% \end{aligned}$$

Application of the ABCD method for the dielectron sample In the electron channel there is one more degree of freedom, both in determining the normalization factor from the ABCD method and also in using a control region of events to provide the shapes. This is the electron identification quality. The best combination is chosen according to the quality of the description of data by the estimation both for the side band region of m_{jj} and the signal region between 100 and 300 GeV/c^2 in m_{eejj}. Also with this approach the samples used as default and for systematic variations are the same listed in 5.5.4. As said at the beginning of section 5.5.4 because of lack of statistics in the tagged analysis bin, the same shape distribution is assumed for both the tagged and the untagged case, which is the one provided by the final selection without the b-tagging requirement.

The systematic uncertainties are estimated in a similar way as in the dimuon case. The final estimate for the QCD multijet background percentage over the total in the dielectron case, is estimated as:

$$\begin{aligned} \text{untagged:} &\quad 6.57 \pm 0.6 \pm 2.3\% \\ \text{tagged:} &\quad 11.5 \pm 5.1 \pm 2.6\% \end{aligned}$$

The final fraction of QCD background used for the normalization of this background is a combination of the results obtained with the two independent methods described above. In particular the weighted mean of the two estimations is taken as central value and the maximum between the difference of these two values and the single systematics is taken as global systematic uncertainty. Thus the results are:

channel	central value (%)		stat. unc. (%)		syst. unc (%)
muon untagged:	3.99	±	0.27	±	0.51
muon tagged:	11.0	±	4.4	±	3.7
electron untagged:	9.7	±	0.9	±	3.1
electron tagged:	11.5	±	5.1	±	2.6

expressed as fraction of multijet events with respect to the data in the final $m_{\ell\ell jj}$ sample.

5.5.5 Summary of backgrounds

The comparison between data and Monte Carlo simulation for the m_{jj} side band region, using all the data driven corrections described in the previous sections, is presented in fig. 5.27. From this figure it is possible to see that the agreement between

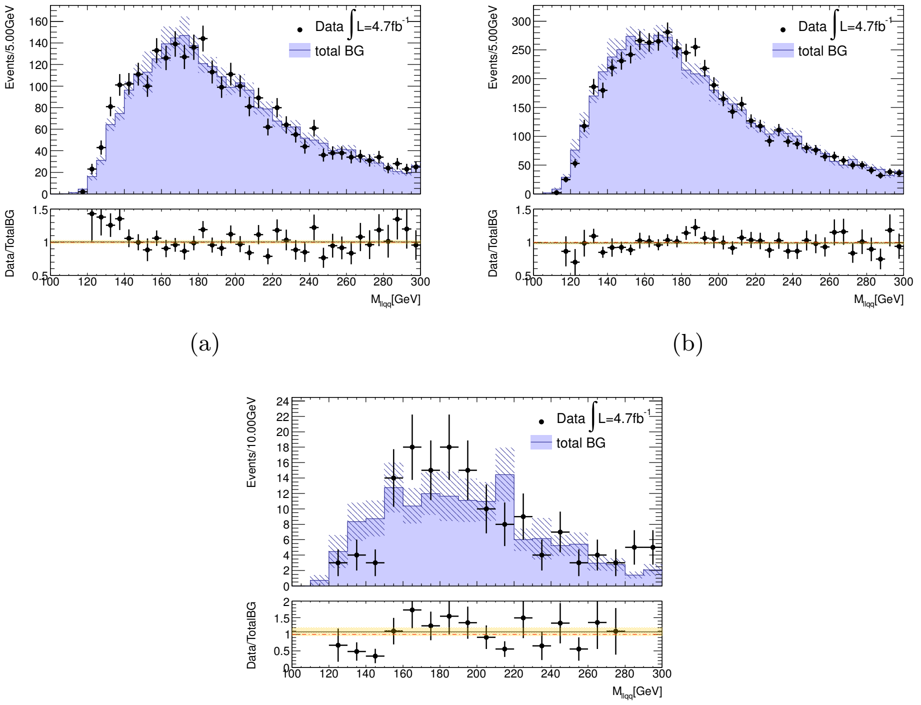

(a) (b) (c)

Figure 5.27. Comparison between data and simulation for the m_{jj} side band region, after the application of the scale factors and using the systematic uncertainty estimates. 5.27(a) and 5.27(b) correspond to the electron and muon channel respectively of the untagged case and 5.27(c) to the tagged case for both channels together.

data and Monte Carlo expectations is quite good over all the $m_{\ell\ell jj}$ spectrum in both tagged and untagged case, for electrons and muons. The statistical uncertainties of the Monte Carlo templates are shown since after all the selection they appear to be not negligible with respect to the usually dominant statistical uncertainty on data. The effect of these uncertainty is included in the calculation explained in the next chapter.

5.6 Systematic Uncertainties

This section describes the calculation of the systematic uncertainties for this analysis. Several systematic uncertainties have been considered: an important contribution comes from theoretical uncertainties on the signal cross section. In addition to this, theoretical uncertainties on the background processes have to be taken into account as well as systematics that may affect the data driven estimations performed for some of the backgrounds, as described in 5.5. Moreover systematics coming from the experimental apparatus and techniques have to be taken into account.

Reconstruction and identification The main detector-related contributions to the systematic uncertainties are the lepton, jet, and E_T^{miss} reconstruction and identification efficiencies, their momentum or energy resolution and scale, and the b-tagging efficiency and mistagging rates, and can be computed measuring the effecto on the final signal, background and data yields after having varied the definition of these objects.

Concerning the muon (electron) p_T (E_T) smearing, the computation of the systematic error derives from the fact that the correction itself is evaluated by means of a Gaussian function using its central value for the nominal correction: systematic variation are obtained varying the central value by $\pm 1\ \sigma$.

The uncertainties on lepton reconstruction, identification and trigger efficiencies are mainly of statistical nature since they are measured from data with the *tag and probe* method, but they have also systematic uncertainty coming from the definition of the tag and the probe leptons used to perform such a measurement.

Jet-related uncertainties include the jet energy scale and resolution uncertainties, which have a direct impact on the signal selection efficiency. Those include uncertainties for close-by jets and the fraction of quarks and gluons in the sample. For b-jets an extra scale uncertainty of between 1% and 2.5%, depending on the jet p_T, is added in quadrature in order to take into account the dependence of the jet energy scale and resolution on the jet flavor. Uncertainties on the MV1 b-tagging efficiency and mistag efficiency are evaluated taking into account the tagger working point, and the fraction of the various quark flavor in the Monte Carlo samples. The uncertainty on E_T^{miss} is obtained by propagating the uncertainties on the individual objects as described in 5.2.4. The size of these detector-related uncertainties are summarized in Table 5.13.

The detailed results of the application of these experimental uncertainties on the selection of signal and background in the different branches of the analysis are presented briefly below. Figure 5.28 and 5.29 show the effect of the jet energy scale systematic uncertainty on the background and signal, respectively. This is the uncertainty which is expected to have the maximum effect on the shape of the $m_{\ell\ell jj}$ distribution, while it can be seen that also due to the use of the kinematic fit on the dijet system, the effect of this uncertainty on the shape has a reduced impact on both the signal and background shape. In the following we will neglect shape uncertainty from jet-energy-scale systematic uncertainty.

Signal cross sections Higgs boson production cross sections have been studied extensively by the LHC Higgs cross section working group and the results are compiled in [53]. Theoretical uncertainties on the cross sections have been estimated to be between $15-20\%$ for $gg \to H$ and $3-9\%$ for $qq \to qqH$ (VBF) for m_H relevant for this analysis. In addition to this another systematic effect has to be considered in order to take into account the accuracy with which the QCD scale is known. This uncertainty amounts to $\sim 14\%$ for all the Higgs mass spectrum.

Source of uncertainty	Treatment in analysis
Luminosity	3.9%
Jet energy scale (JES)	2–7%, as a function of p_T and η
Jet pileup uncertainty	3–7%, as a function of p_T and η
b-quark energy scale	2.5–1% as a function of p_T
Jet energy resolution	1–4%
Electron selection efficiency	0.7–3%, as a function of p_T; 0.4–6%, as a function of η
Electron reconstruction efficiency	0.7–1.8%, as a function of η
Electron energy scale	0.1–6%, as a function of η, pileup, material effects, etc.
Electron energy resolution	Sampling term 20%; a small constant term has a large variation with η
Muon selection efficiency	0.2–3%, as a function of p_T
Muon trigger efficiency	$< 1\%$
Muon momentum scale	2–16%, as a function of η
Muon momentum resolution	p_T and η dependent resolution smearing functions, systematic $\leq 1\%$
b-tagging efficiency	5–15%, as a function of p_T
b-tagging mistag rate	10-22%, as a function of p_T and η
Missing transverse energy	Add/subtract object uncertainties in E_T^{miss} + uncertainty on“SoftJet” and “CellOut” terms

Table 5.13. Systematic uncertainties related to object reconstruction and identification

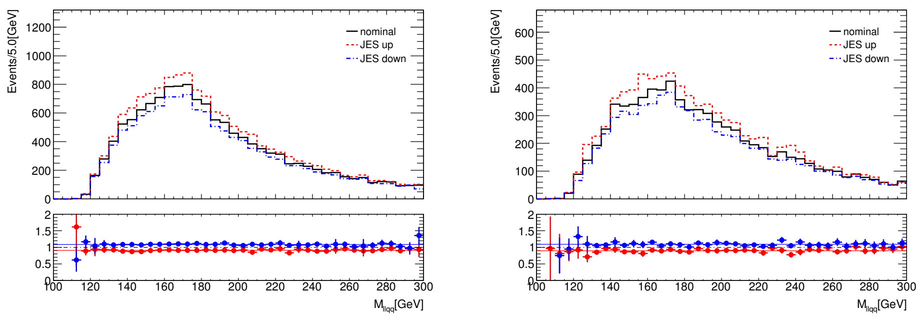

(a) (b)

Figure 5.28. Reconstructed Higgs mass for nominal jet energy scale compared to the $\pm 1\sigma$ variation, for background events in the signal region 5.28(a) and sideband region 5.28(b).

Background normalization The normalization uncertainties of the Z/DY +jets and top backgrounds are estimated through the data driven methods varying the control regions discussed in 5.5, and the variation of the resulting normalization is used as systematic error. The resulting uncertainty for the DY/Z+ jets sample is approximately $3-4\%$ in the untagged channel, while in the tagged case it reaches the value of 17%. The top background uncertainty is estimated to be 10% (7%) for the untagged (tagged) case. The diboson background contributions are assigned a theory uncertainty of 11%.

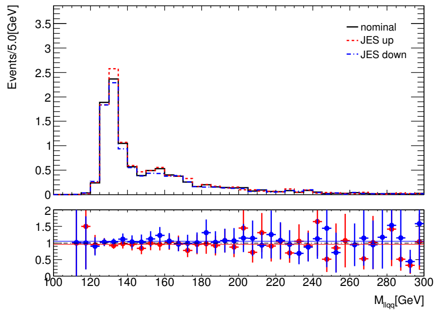

(a)

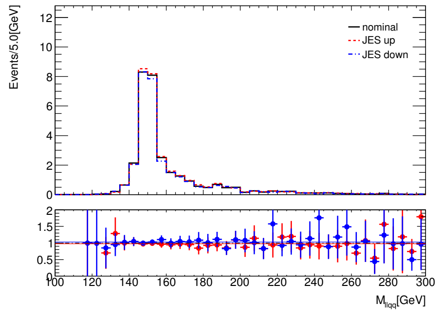

(b)

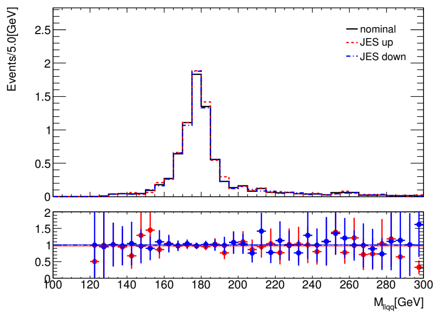

(c)

Figure 5.29. Reconstructed Higgs mass for nominal jet energy scale compared to the $\pm 1\sigma$ variation, for Higgs signal simulation for 130 5.29(a), 150 5.29(b), and 180 GeV/c^2 Higgs mass 5.29(c)

DY + jets shape As it is shown in fig. 5.27, the shape of the background afternormalization corrections is reasonably described by the Monte Carlo simulation. Nevertheless, the shape uncertainty for the DY +jets background is estimated by parametrizing the remaining difference of the $m_{\ell\ell jj}$ distribution of the m_{jj} sidebands, after the application of the normalization scale factor as a function of $m_{\ell\ell jj}$. In the tagged case the statistical accuracy obtained in this sample is not adequate for such a study and therefore the results of the untagged case are used.

Multijet background normalization The multijet background normalization uncertainty is calculated as described in Section 5.5.4: since the normalization of this background can is calculated with two independent methods, and in each method several QCD-enriched samples can be used, the maximum between the half difference of the two estimations and each systematic (calculated varying the QCD sample) is taken as systematic. The result of this study is that the QCD normalization uncertainty in the muon untagged channel is $\sim 15\%$ in the muon untagged sample, $\sim 35\%$ in the electron untagged channel, while it is $\sim 50\%$ in the untagged channels (both muons and electrons).

Multijet background shape The shape uncertainty on the multijet background is evaluated building the final $m_{\ell\ell jj}$ ditribution with the other available multijet samples besides the default ones, as explained in 5.5.4 and shown in fig. 5.25. The shape uncertainty on this background is evaluated to be negligible.

Luminosity The luminosity uncertainty for 2011 data is 3.9%. This uncertainty is only applied to MC samples for which the normalization uncertainty is not taken directly from a comparison between data and MC, which is everything except the DY/Z + jets, the top and the multijet background. Where it is applied this systematic uncertainty is assumed to be correlated across all samples.

Additional details on how the systematic uncertainties listed above are implemented and details about the possible correlations between them are given in section 6.1.

Chapter 6

Results

The search for the Higgs boson is performed by comparing the invariant mass of the $\ell\ell jj$ system, i.e. the reconstructed Higgs boson mass, in the data to that of the expected background. Following the full selection explained in chapter 5, four independent research channels are obtained splitting the analysis in two leptonic sub-channels (e and μ) and in tagged and untagged sub-channels, composed of events containing exactly two jets tagged as coming from a b quark and events containing up to one b-tagged jets respectively. After the full selection the Higgs boson is expected to appear as a narrow peak over a smooth background distribution. This is due to one of the main features of this analysis, that is the possibility to fully reconstruct the final state, which is not possible for other analyses (e.g. the $H \to WW$ analyses) which include undetected particles such as neutrinos in the final state.

After the kinematic fit the expected resolution for the core signal event distribution is expected to be around 3 GeV/c^2, as shown in fig. 5.19. A long tail is also present above the nominal Higgs mass, specially for the very low mass hypotheses as explained in section 5.3.3. The background invariant mass distribution has instead a very broad distribution peaking at around 170 GeV/c^2, with a width of about 40 GeV/c^2. The distribution of the $\ell\ell jj$ system invariant mass, $m_{\ell\ell jj}$, for data compared to the predicted background after all data-driven scale factor are applied are shown in fig. 6.1 and fig. 6.2 for the muon and electron channels respectively. The expected Higgs signal for 130 GeV/c^2 mass (multiplied by a factor 20 in the untagged case and by a factor 5 in the tagged case) is displayed on top of the background prediction. A detailed breakdown of the different predicted background sources, data counts and expected signal number of events are also reported in tables 6.1 and 6.2, for the four independent analysis channels.

The goodness of the agreement between data and Monte Carlo has been checked with several studies aimed at comparing data to Monte Carlo expectations in signal-free sidebands (details in section 5.5), and scale factors have been obtained for the main backgrounds in order to account for any possible disagreement. Once the data-Monte Carlo agreement is checked in the control regions, the background expectation can be compared to data in the signal region and, as can be seen in fig. 6.1 and fig. 6.2, no significant excess of observed events over background is found.

The only disagreement between the data and the background model is found in the muon untagged channel in the region $160 \lesssim m_{\ell\ell jj} \lesssim 180$ GeV/c^2. The undershoot of data with respect to background prediction is discussed in detail in section 6.2.

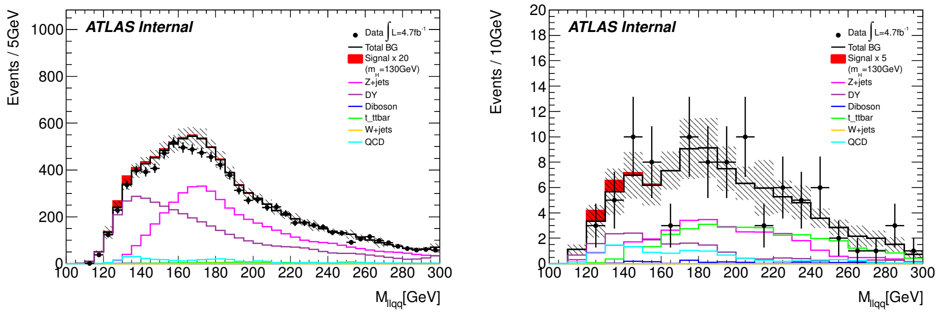

(a) (b)

Figure 6.1. Distribution of the reconstructed Higgs mass in the muon channel with data compared to the background prediction including signal for an Higgs mass hypothesis of 130 GeV/c^2. Untagged selection 6.1(a) and tagged selection 6.1(b)

Source	Untagged	Tagged
DY+jets	9635 $\pm$ 101 $\pm$ 409	53.0 $\pm$ 5.3 $\pm$ 7.7
Top	99.0 $\pm$ 1.8 $\pm$ 9.8	33.8 $\pm$ 1.0 $\pm$ 2.2
Multijet	388 $\pm$ 26 $\pm$ 50	11.0 $\pm$ 4.4 $\pm$ 1.6
Diboson	60.9 $\pm$ 1.2 $\pm$ 9.1	1.7 $\pm$ 0.2 $\pm$ 0.3
W+jet	10.9 $\pm$ 2.5 $\pm$ 1.6	–
Total background	10194 $\pm$ 105 $\pm$ 412	99.5 $\pm$ 7.0 $\pm$ 8.2
Data	9714	105
Signal $m_H = 120$ GeV	2.07 $\pm$ 0.10 $\pm$ 0.12	0.080 $\pm$ 0.018 $\pm$ 0.010
Signal $m_H = 130$ GeV	7.26 $\pm$ 0.28 $\pm$ 0.38	0.431 $\pm$ 0.067 $\pm$ 0.051
Signal $m_H = 150$ GeV	21.1 $\pm$ 0.60 $\pm$ 0.73	1.561 $\pm$ 0.167 $\pm$ 0.178
Signal $m_H = 180$ GeV	4.86 $\pm$ 0.20 $\pm$ 0.17	0.299 $\pm$ 0.049 $\pm$ 0.034

Table 6.1. Summary of the expected number of background events, observed events in data, and expected signal events for the untagged and tagged selections in the muon sample. The statistical and systematic uncertainties on the estimated background and signal events are also shown

For the moment, in order to go on with the analysis, it is just important to note that the disagreement in that area is covered considering the statistical uncertainty of the Monte Carlo samples (represented by the shaded area in fig. 6.1 and 6.2) and the statistical uncertainty affecting the data.

Since no relevant data excess is observed, the obtained distributions can be used to set limits on the Higgs boson production cross section: a tiny signal contribution is expected in the final sample (see fig. 6.1 and fig. 6.2 and tables 6.1 and 6.2), nevertheless a statistical test can be performed to determine the minimum Higgs boson production cross section that can be excluded by the present data. The test compare data with background-only and background+signal hypotheses for different signal cross section values as a function of the hypothetical Higgs mass.

In the following the statistical procedure and tools used to set the limits on the Higgs boson cross section in this final state are described.

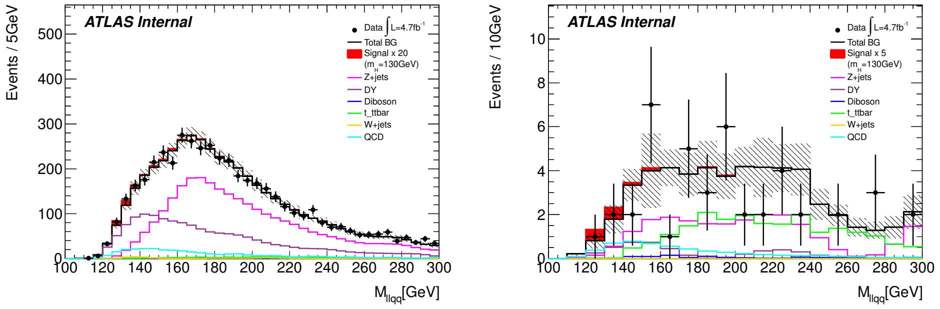

(a) (b)

Figure 6.2. Distribution of the reconstructed Higgs mass in the electron channel with data compared to the background prediction including signal for an Higgs mass hypothesis of 130 GeV/c^2. Untagged selection 6.2(a) and tagged selection 6.2(b)

Source	Untagged					Tagged				
DY+jets	4654	±	42	±	161	30.5	±	3.5	±	4.4
Top	69.0	±	1.5	±	7.8	22.2	±	0.8	±	1.6
Multijet	502	±	46	±	165	7.0	±	3.2	±	2.5
Diboson	36.3	±	1.0	±	5.3	1.1	±	0.2	±	0.2
W+jet	30.2	±	10.7	±	4.3			–		
Total background	5291	±	63	±	231	60.8	±	4.8	±	5.3
Data	5197					51				
Signal $m_H = 120$ GeV	0.90	±	0.06	±	0.07	0.042	±	0.016	±	0.006
Signal $m_H = 130$ GeV	3.19	±	0.18	±	0.24	0.288	±	0.055	±	0.037
Signal $m_H = 150$ GeV	9.70	±	0.40	±	0.55	0.594	±	0.100	±	0.072
Signal $m_H = 180$ GeV	2.85	±	0.15	±	0.14	0.177	±	0.039	±	0.021

Table 6.2. Summary of the expected number of background events, observed events in data, and expected signal events for the untagged and tagged selections in the electron sample. The statistical and systematic uncertainties on the estimated background and signal events are also shown.

6.1 Exclusion confidence level determination

Once an expected distribution for the known processes is obtained (the background distribution) and also a data distribution is available, many statistical tests can be performed in order to measure the compatibility of the data with the background-only or with the signal plus background hypotheses [59].

Usually the hypothesis tests are performed calculating the ratio between the likelihood fit to the observed data using the background-only and signal-plus-background hypotheses. We also adopt this approach in this analysis using the CL_s frequentist formalism [61]. The CL_s limit procedure ensures stable results even when the final sample is dominated by the background processes with just a tiny contribution from the signal processes. Since this analysis falls within this category, as shown in tables 6.1 and 6.2, the CL_s approach is chosen.

Given the two hypotheses, namely the background-only hypothesis b and the signal-plus-background hypothesis $s+b$, the CL_s is defined as [61]:

$$CL_s = \frac{p_{s+b}}{1-p_b} \tag{6.1}$$

where p_h is the *p-value* of the hypothesis h. The *p-value* is defined as the probability to observe a fluctuation in data that is equal or bigger than the observed one, once an hypothesis is considered.

In principle the CL_s consists of the generation of Monte Carlo toy experiments to evaluate the distribution of the test statistics and upper limit on the cross section and the bands representing the possible statistical fluctuation of the actual result in a frequentistic approach. In our case, since the final sample has very high statistics the asymptotic approach can be used to obtain the probability density function (p.d.f.) of the likelihood ratio: the asymptotic approach allows to extract the expected significance and the 1 and 2 σ variations for a given C.L. from an analytical calculation. The results obtained with the asymptotic calculation converge to the results obtained with toy Monte Carlo experiments when the data sample is largely populated, as shown in [59]. This approach has been already successfully followed in the Higgs boson search in the high mass range [63, 64], in which the population of the final samples is similar to what is obtained in this analysis. The implementation of such a study was performed using the RooStats package [62].

The input distributions to the statistical procedure described above are histograms representing the expected distributions of $m_{\ell\ell jj}$ for background and signal as well as those observed in data, which are obtained applying the full selection explained in chapter 5 and shown in fig. 6.1–6.2 for all the four sub-channels.

For signal process the samples described in section 5.1.2 are used, and 13 mass points in the $120 - 180$ GeV/c^2 interval with 5 GeV/c^2 spacing are considered.

In addition to the input histograms described above, a set of nuisance parameters is considered to take into account the systematic uncertainties listed in section 5.6. In principle several kinds of systematic uncertainties can be considered. In this analysis several checks have been performed in order to have a proper modelling of all the systematic uncertainties affecting the measurement. As explained in section 5.6 the biggest uncertainties arises from the jet energy scale. As can be seen in figures 5.28 and 5.29, the variation of the jet energy scale has and effect on the normalization of both signal and backgrounds, but does not introduce systematic variation on the shapes. This can be seen from the ratios shown in lower part of the plots in figures 5.28 and 5.29, where no particular trend is observed when the jet energy scale is varied with respect to its default value. Because of this no shape systematic is taken into account.

The systematic uncertainty on the normalization of the templates is evaluated by varying the several selection criteria that may have an impact on the final distributions as well as on the calculation of the scale factors. The observed variation of the final yield is taken as normalization uncertainty for each sample. Concerning this kind of uncertainty each sample receives contribution from both sources common to all the other samples and particular sources affecting only the considered sample: the common uncertainties are related to the definition of the physical objects used to select the events. As an example, if the definition of a good muon given in section 5.2.1 is changed, this may have an impact on the number of good muons found in each event and hence, since exactly two same flavor leptons are required in each event and the presence of any additional lepton is vetoed, the final event selection could be affected too. The same holds for jets and electrons definition and energy scale. In principle the effects of a given systematic uncertainty may be correlated between different samples. As an example consider the jet energy scale: if the jet energy scale is varied upwards, the energy of each jet in the event is increased, and hence more events containing at least two jets having p_T greater than the minimum threshold of 25 GeV/c will be available, and this is true for all the samples (signal and backgrounds) that are evaluated with Monte Carlo simulations. Since the QCD background is basically evaluated, in both methods described in section 5.5.4, as the remaining part between the data distribution and the Monte Carlo expectation, an enhancement of the Monte Carlo expectation reflects in a reduction of the fraction of QCD events. Following the explanation given above, the jet energy scale effect on the QCD background is considered to be anticorrelated with respect to the impact that it has on the Monte Carlo-based samples. Moreover, since the normalization of some backgrounds, namely top in the tagged channel only and DY/Z + jets, is evaluated from comparison to data in ad hoc control regions (see sections 5.5.1 and 5.5.2 for details), the systematic uncertainty on their normalization is evaluated from control regions too by varying the definition of the control regions themselves. Because of this, the contribution to the normalization uncertainty coming from the variation of the detector- and selection-related parameters is not included in the normalization uncertainty of these two samples. In particular the normalization uncertainties of the top and the DY/Z + jets background in the tagged sample (in which both the samples are normalized to control regions) are considered to be somehow anticorrelated: since the final total yield is fixed from what is observed in the data and these are the two main background in this channel one can naively think that when one of the two backgrounds is varied upwards the other one is forced to vary downwards and viceversa.

Other than the common systematics, some particular source of uncertainty are considered for each sample: For the signal samples theoretical uncertainties due to the limited knowledge of the QCD scale (see section 5.6 for details) are considered for both gluon fusion and vector boson fusion processes. An additional uncertainty is considered only for the gluon fusion process to take into account the uncertainty related to the Higgs p_T reweighting explained in section 5.1.2.

As already said, the uncertainty on the normalization of the top sample in the tagged case is evaluated from the control region obtained inverting the E_T^{miss} cut, varying the value of the cut. However in the untagged sample the normalization of this is taken from the Monte Carlo simulation, and therefore the common systematics listed above (and in section 5.6) are applied. In addition to those, a theoretical uncertainty on the top production cross section is applied.

As mentioned in section 5.5.1 the systematic uncertainty on the DY/Z + jets normalization is evaluated varying the definition of the sidebands used to evaluate the normalization itself. Since this procedure is applied in all the four subchannels, no additional systematics are added to this background.

For the others Monte Carlo-based backgrounds only theoretical uncertainties on the production cross sections are considered in addition to the common systematics.

For all the common systematic uncertainties in the QCD sample the treatment explained above for the jet energy scale holds, and therefore their effect on this sample is considered anticorrelated with the corresponding effect on the other samples. For the QCD an additional uncertainty coming from the difference of the result obtained with the two different methods used to estimate it and from the variation of the result obtained varying the template used to model the QCD sample.

In addition to the systematics described above and in section 5.6, another kind of nuisance parameter is considered: in figures 6.1 and 6.2 the statistical uncertainty of the total background expectation is shown as a shaded area. As it can be seen from these figures, it turns out that this kind of uncertainty is not negligible, since it is comparable to the statistical uncertainty of the data. Because of this the statistical uncertainty of the Monte Carlo samples is included in the following statistical procedure. It is considered as a nuisance parameters which allows each bin of the total expected background to vary within its maximum and minimum values independently from the others.

Given the above inputs and nuisance parameters, a maximum likelihood fit is performed, the likelihood ratio is built and its p.d.f. is obtained with the asymptotic calculation introduced above and explained in [59]. From the obtained p.d.f. the expected and 1 and 2σ variations are extracted for 95% C.L. for each of the mass points used in this analysis.

The results obtained following the above procedure are shown in fig. 6.3 and are normalized to the Standard Model expectation so that the existence of the Standard Model Higgs boson is excluded at 95% C.L. when the observed limit reaches value 1, highlighted with a red horizontal line: the dashed line represent the expected limit on the production cross section of the Higgs boson, the green and yellow bands represent the 1 and 2σ variation respectively, while the observed limit is represented by the the black markers connected with a black solid line. The corresponding numbers are shown in table 6.3.

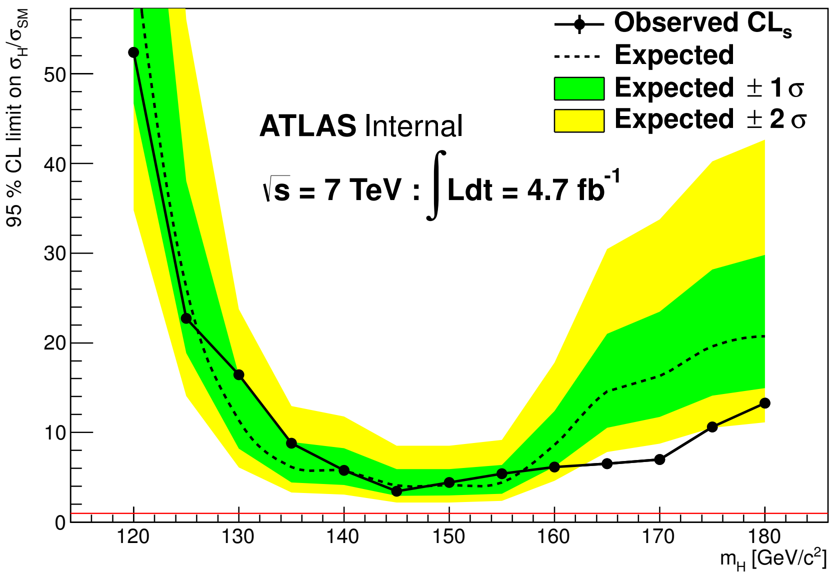

Figure 6.3. Limits on the Higgs boson existence in the $\ell\ell q\bar{q}$ final state. The dashed line represents the expected limit, with 1 and 2 σ variations shown with green and yellow bands respectively. The black markers and the solid black line represent the observed limit. The red orizontal line is at $\sigma_{\rm H}/\sigma_{\rm SM} = 1$

m_H (GeV/c^2)	Observed $\mu/\mu_{\rm SM}$	Expected $\mu/\mu_{\rm SM}$ -2σ	-1σ	Median	$+1\sigma$	$+2\sigma$
120	52.38	34.78	46.69	64.79	94.22	139.71
125	22.72	14.07	18.88	26.21	38.05	56.04
130	16.43	6.11	8.21	11.39	16.42	23.77
135	8.80	3.31	4.45	6.17	8.93	12.96
140	5.79	3.08	4.13	5.74	8.23	11.80
145	3.45	2.20	2.95	4.10	5.91	8.53
150	4.45	2.22	2.98	4.14	5.94	8.52
155	5.39	2.37	3.18	4.41	6.37	9.19
160	6.16	4.63	6.21	8.62	12.40	17.79
165	6.54	7.83	10.51	14.58	21.02	30.43
170	6.98	8.74	11.73	16.28	23.47	33.77
175	10.61	10.52	14.12	19.60	28.15	40.24
180	13.28	11.13	14.94	20.74	29.78	42.63

Table 6.3. Limits on the Higgs boson existence in the $\ell\ell q\bar{q}$ final state

With the full 2011 ATLAS data sample no exclusion is obtained for the $H \to ZZ^* \to \ell^+\ell^- q\bar{q}$ process in the $120 - 180$ GeV/c^2 mass range. The best sensitivity is reached for $m_H = 145$ GeV/c^2, where an expected limit of 4.10 times the Standard Model Higgs boson cross section is obtained, while the corresponding observed sensitivity is 3.45 times the SM Higgs boson cross section. The observed limit in the $160 - 170$ GeV/c^2 range is found to be below the expected limit of more than 2σ. This underfluctuation of the data comes mainly from the background overshoot that can be observed in the final $m_{\ell\ell jj}$ spectrum in the untagged muon channel. In the next section a detailed study of this data-Monte Carlo disagreement is reported.

6.2 Detailed cross checks on the result

As can be seen from figure 6.1(a) in the $160 \lesssim m_{\ell\ell jj} \lesssim 180$ GeV/c^2 mass range the background prediction exceeds the data. Many detailed studies have been carried out in order to understand the origin of this disagreement, and it has been found that part of the overshoot in the background expectation is due to few events coming from the ALPGEN Drell-Yan *Np0* sample (that is the Drell-Yan production without any additional parton, see section 4.2.1 for details) which survives the full selection and contributes to the final background sample with very high weight (see section 5.4 for details on the weight of the Monte Carlo events). This can be seen in detail in figure 6.4, in which the ALPGEN Drell-Yan sample with n additional partons (where n goes from 0 to 5) are drawn independently for muons (6.4(a)) and electrons (6.4(b)). First of all it is worth to notice that this is a really extreme condition for the ALPGEN phase space: in the hard scattering there are no partons generated in addition to the lepton pair and at the end we find two jets in the event. The two reconstruct jets come from the fragmentation process which is modelled with HERWIG. Looking at fig. 6.4 can be seen that the Drell-Yan with 0 additional partons survives the full selection only in the muon channel and it is not there in the final Drell-Yan electron sample. This difference is mainly due to little differences in reconstruction

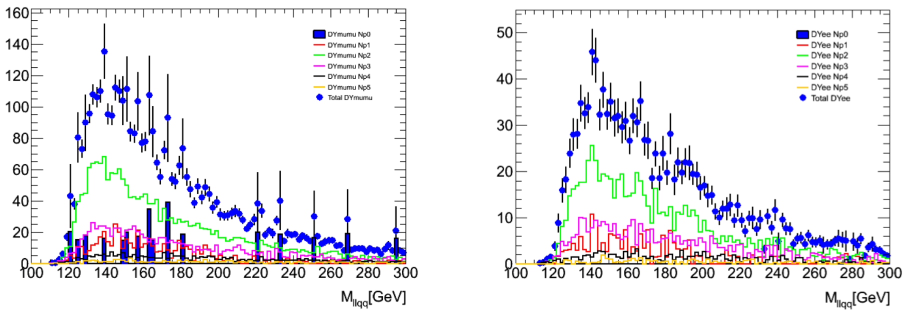

(a) (b)

Figure 6.4. Detailed $m_{\ell\ell jj}$ distribution for the ALPGEN Drell-Yan with n addidional partons ($n = 0, ..., 5$) for muon 6.4(a) and electrons 6.4(b) in the untagged channel

and selection efficiency between muons and electrons: the lowest trigger threshold is 14 GeV for electrons E_T, while it goes down to 12 GeV/c for the muon p_T (details on trigger selection are given in section 5.3.1), thus allowing more Drell-Yan events (containing low-p_T leptons) to be selected in the muon channel than in the electron channel. In addition to this identification and reconstruction efficiencies for electrons are in general lower than those for muons: in particular, as said in sections 5.2.1 and 5.2.2, the combined identification and reconstruction efficiency for the muon category used in this analysis is above 95%, while for electrons it is $\sim 80\%$.

The events coming from the DY+*Np0* sample are shown with the blue histogram in fig. 6.4(a): they are really few and they contribute with very high weight. In the same plot also the sum of all the Drell-Yan samples is shown together with its statistical uncertainty: it is represented by the blue markers with the associated error bars. It can be seen that the total distribution shows spikes and large uncertainties in correspondence of the events with 0 additional partons. Even though the Drell-Yan with 0 additional partons introduces the distortion just described we decide to keep the events coming from this sample in the final shape and normalization since it is the real outcome of this analysis.

In addition to what is said above, a detailed check on the data-Monte Carlo discrepancy seen in fig. 6.1(a) can be done looking at the results of the maximum likelihood fit performed to extract the limit on the Higgs production cross section. In the fit each nuisance parameter is varied within its maximum and minimum values given by the uncertainties applied to it, and the result from the fit is variation for each sample, corresponding to new normalization of that sample giving the best agreement between data and Monte Carlo. The variation is expressed in terms of a fraction of the considered uncertainty. From this variation obtained from the fit, a scale factor can be obtained with the relation:

$$\text{scale factor} = \prod_i (1 + \alpha_i \times \sigma_i) \tag{6.2}$$

where the product includes all the systematics affecting the considered sample, α_i is the variation as obtained from the fit and σ_i is the value of the systematic uncertainty taken into account. The obtained scale factors in the muon untagged channel are all between -1 and 1, which means that the best fit is obtained varying the several samples within just one σ, and therefore the excess is well covered considering the systematic uncertainties explained in section 5.6 and the bin by bin statistical uncertainty applied to the Monte Carlo templates. Figure 6.5 shows the final $m_{\ell\ell jj}$

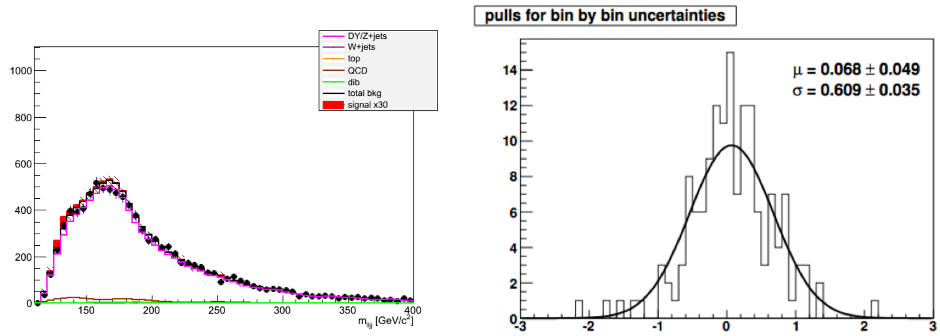

(a) (b)

Figure 6.5. $m_{\ell\ell jj}$ spectrum including the scale factor for each sample obtained with the maximum likelihood fit

distribution in the muon untagged channel in which each sample is rescaled according to result of the fit. As it can be seen the agreement between data and Monte Carlo is better than in figure 6.1(a). Among all the scale factors, the most relevant is obtained for the DY/Z + jets sample. This can be expected since, as shown above and in fig. 6.4, the Drell-Yan sample (and the *Np0* sub-sample in particular) is one of the main responsible for the Monte Carlo overshoot, therefore a negative variation (corresponding to a scale factor smaller than one) may be foreseen. That is indeed what is found: the obtained variation is -0.89 ± 0.33, which corresponds to a scale factor of 0.961 ± 0.014.

Beside to the systematic uncertainties, also statistical uncertainties of the Monte Carlo templates are taken into account. As already explained in section 6.1, this kind of uncertainty is treated as an additional bin by bin nuisance parameter. Also in this case the results obtained from the fit confirm that the combination of the two kinds of uncertainty completely cover the data-Monte Carlo discrepancy: as can be seen from fig. 6.5(b) the great part of the variations obtained for this kind of errors are within -1 and 1.

6.3 Comparison with similar results

The result obtained with this analysis can be compared to similar results already published: in particular ATLAS has already published the Higgs search in the $H \to ZZ \to \ell^+\ell^- q\bar{q}$ process in the high-mass region ($m_H > 200$ GeV/c^2) and the detailed explanation of this search can be found in [63] and [64], while the CMS experiment published the same search over the whole mass range, and details can be found in [65] and [66]. A detailed comparison with these two results is given in the following. At the end of section 6.3.2 a comparison between our result and the une obtained with the Higgs boson search in the $H \to ZZ^* \to \ell^+\ell^-\ell^+\ell^-$ channel is given. As already said in chapter 1, the $\to 4\ell$ channel is the "golden channel" for the Higgs search, so the comparison is to see at which point with respect to one of the best results available the analysis presented in this thesis is.

6.3.1 Comparison with CMS

As already mentioned, the CMS collaboration published the Higgs search in the $H \to ZZ^* \to \ell^+\ell^- q\bar{q}$ channel on the whole mass range on 2011 data [66, 65]. A directo comparison between the results of the analysis shown in this thesis and the results published by the CMS collaboration can be done since the same dataset (full 2011 statistics at $\sqrt{s} = 7$ TeV) and the same final state are used. Figure 6.6 shows

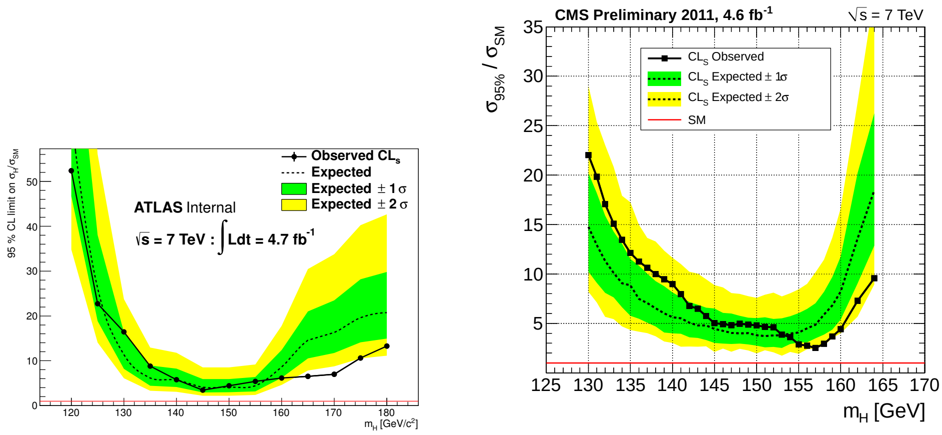

(a) (b)

Figure 6.6. Comparison of the limits obtained with this analysis 6.6(a) (already shown in fig. 6.7(a) and fig. 6.3) and the results published by the CMS collaboration with the 2011 full dataset in the same final state and in a similar mass region

the comparison between the result obtained with this analysis and the corresponding result published by CMS. In general can be seen that the results presented in this thesis is slightly better than the one published by CMS: table 6.4 shows the obtained expected and observed limits for three different mass points. The relevant number

	This analysis		CMS	
m_H (GeV/c^2)	Expected	Observed	Expected	Observed
130	11.39	16.43	~ 15	~ 22
145	4.10	3.45	~ 4.5	~ 5
160	8.62	6.16	~ 8	~ 4.5

Table 6.4. Comparison of the expected and observed limit on the Standard Model Higgs boson cross section (expressed as μ/μ_{SM}) in the $\ell^+\ell^- q\bar{q}$ final state as obtained in this analysis and as published by the CMS collaboration

to look at in order to have a direct comparison between the two analyses is the expected limit, and it can be seen that the analysis presented in this thesis has a lower expected limit with respect to the one published by the CMS collaboration. This difference mainly arises from differences in acceptance between the two analyses: to study this final state the CMS collaboration requires the jet p_T to be above

30 GeV/c, that is a threshold 10 GeV/c higher than the one used in this analysis (as explained in section 5.2.3). Another item that may explain the difference of the two results is on the lepton selection: as shown in section 5.3.1 two types of trigger are used to select the events used to study the $H \to ZZ^* \to \ell^+\ell^- q\bar{q}$ process: a single lepton trigger requiring the presence of an high-p_T lepton, to which corresponds the configuration with an high-p_T lepton and a low-p_T one ($p_{T,1} > 20$ GeV/c and $p_{T,2} > 7$ GeV/c), and a dilepton trigger, which is associated to events containing two leptons with intermediate p_T values ($p_{T,1,2} > 12 - 14$ GeV/c for muons−electrons). The latter configuration has no equivalent in the CMS search. This has an impact specially in the very low Higgs boson mass region ($m_H < 150$ GeV/c^2), where the analysis presented in this thesis has better performances: as an example consider an Higgs boson with $m_H = 130$ GeV/c^2. As mentioned in section 5.3.1, the usage of the double lepton trigger in addition to the single lepton one brings a gain on the final Higgs yield of about $\sim 30\%$ in the muon channel and $\sim 23\%$ in the electron channel.

6.3.2 Comparison with other ATLAS results

As already mentioned in the previous chapter, the work presented in this thesis is the first search of the Higgs boson in the $H \to ZZ^* \to \ell^+\ell^- q\bar{q}$ final state, therefore no corresponding results for a direct comparison are available in the ATLAS literature. The only similar result is the standard Higgs boson search with the $H \to ZZ \to \ell^+\ell^- q\bar{q}$ process which is performed in the high-mass range ($m_H > 200$ GeV/c^2). Actually the analysis shown in this thesis has been conceived and developed as an extension of the standard $H \to ZZ \to \ell^+\ell^- q\bar{q}$ search, and therefore a comparison between these two analyses follows.

In figure 6.7 the limit on $\sigma/\sigma_{\mathrm{SM}}$ obtained with this analisis and shown in fig. 6.3 is compared to the final limit obtained in the high-mass range by ATLAS with the full 2011 data sample. The analysis in the high-mass region is optimized

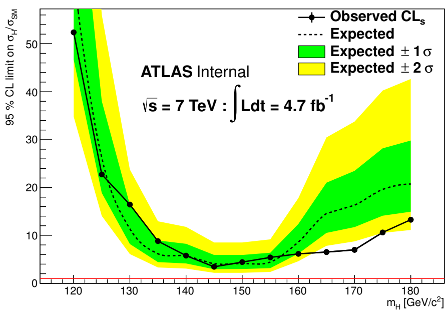

(a)

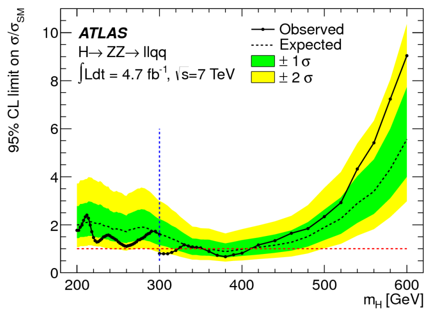

(b)

Figure 6.7. Comparison of the limits on the existence of the Standard Model Higgs boson. 6.7(a) represents the result obtained with this analysis (already shown in fig. 6.3), while 6.7(b) represents the public result of the ATLAS collaboration before the study shown in this thesis was performed.

taking into account the characteristics that this channel offers in that region (e.g. both the Z bosons coming from the Higgs boson decay are on-mass-shell) and the discontinuity an $m_H = 300$ GeV/c^2 in fig. 6.7(b) is due to further optimization in the very-high-mass region. As can be seen from the comparison, the result published by ATLAS in the high-mass region is more competitive than the one obtained with this analysis in the low mass region. Although the two analyses are not directly comparable since different procedures are used as explained in detail in section 5.3.3, the difference between the two results can be discussed, and, besides the already mentioned intrinsic difference in the jet selection criterion, can be accounted for to several reasons: the search in the low mass region is affected by relatively higher backgrounds: the best signal to background ratio in the high-mass search is 2.6% in the untagged channel and 30.7% in the tagged channel, while they drop to 0.2% in the untagged channel and 1.6% in the tagged channel for the low-mass search. In particular the multijet and the top background which are considered among the minor backgrounds in the high-mass analysis (in which the only dominant background is the $Z+$jets process, without any contribution from the lower part of the dilepton mass spectrum) become relevant in the low mass search. In addition to this the intrinsic difference of the signal process in the two mass regions need to be taken into account: as shown in figure 1.8 the branching ratio of the $H \to ZZ$ decay is quite flat for $m_H \gtrsim 200$ GeV/c^2, while it varies a lot in the $120-180$ GeV/c^2 since in the low mass region many others decay channels are available. This implies that, besides the irregular behaviour, the values of this branching ratio in the low mass region are in general lower than those in the high-mass region, where only the $H \to W^+W^-$ decay channel is present, and the $H \to t\bar{t}$ process starts at very high masses and gives a little contribution. As an example the value of $\sigma_H \times \mathrm{BR}(H \to ZZ^*)$ can be considered in two points used in the two analyses: for $m_H = 140$ GeV/c^2 we obtain $\sigma_H \times \mathrm{BR}(H \to ZZ^*) = 0.129$ pb, while for an Higgs with $m_H = 500$ GeV/c^2 it is $\sigma_H \times \mathrm{BR}(H \to ZZ^*) = 0.252$ pb, that is almost a factor of two higher. The trend of the $H \to ZZ^*$ branching ratio in the $120-180$ GeV/c^2 region together with the selection efficiency shown in figure 5.17 have an impact on the behaviour of the expected limit: in particular if for a given Higgs boson mass a lower number of signal events is expected (because of a lower Higgs boson branching ratio or due to a not optimal selection efficiency) this would be reflected in an higher expected limit, as can be seen in the two extreme regions (i.e. $m_H < 130$ GeV/c^2 and $m_H > 165$ GeV/c^2) of the limit plot in fig. 6.3. Moreover in this analysis only half of the signal sample is taken into account: as shown in fig. 5.9 the signal samples is made of two main contribution, the one use in this analysis in which the on-shell Z boson decays into quarks while the off-shell Z boson gives rise to leptons and the one in which the on shell Z boson decays to leptons and the virtual Z boson decays to quarks. In particular the second contribution is not usable for an Higgs search since the main background coming from the $Z+$jets process would be an irreducible background, and given the huge cross section of this process with respect to the signal's one, the analysis would be almost impossible.

In conclusion, the $H \to ZZ \to \ell^+\ell^- q\bar{q}$ search has been extended to the low mass region, where the search in the same final state is much more difficoult, and a competitive result is obtained.

Finally a third comparison can be performed with the results obtained with the Higgs boson search in the $H \to ZZ^* \to \ell^+\ell^-\ell^+\ell^-$ process, which is well known to be the most powerful search channel in the low mass region. As already said in section 1.6, the analysis $H \to ZZ^* \to \ell^+\ell^-\ell^+\ell^-$ process in both 2011 and 2012 datasets gave one of the most important contribution to the discovery of the Higgs-like particle which has been announced on July 4th 2012. However, in order to have a meaningful comparison, the results of this analysis is compared with the one obtained in the four lepton channel on the same dataset. Details about this analysis are given in [67] and [68]. As said in chapter 1, the $H \to ZZ^* \to \ell^+\ell^-\ell^+\ell^-$ process represents the

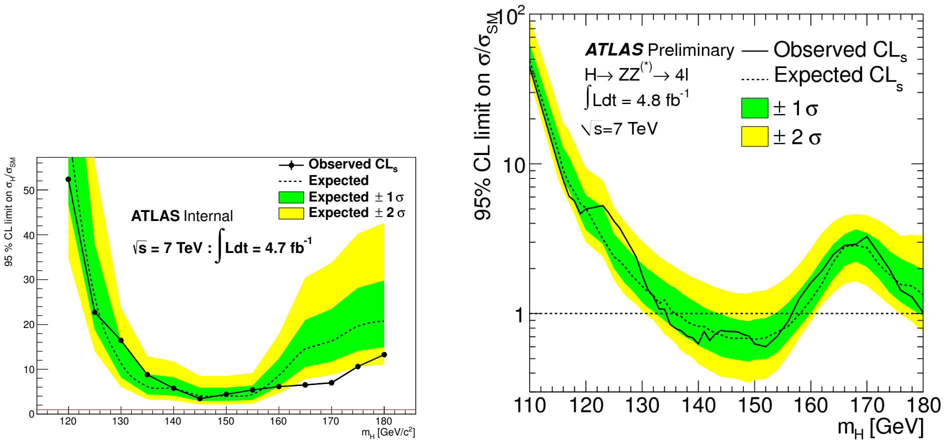

(a) (b)

Figure 6.8. Comparison of the limits obtained with this analysis 6.6(a) (already shown in fig. 6.7(a), 6.3 and 6.6(a)) and the results obtained by the ATLAS collaboration with the same dataset with the analysis of the $H \to ZZ^* \to \ell^+\ell^-\ell^+\ell^-$ process 6.8(b)

"gold-plated channel" for the search of the Higgs boson, since it gives a very clean final state and the background are really tiny: the dominant background in this channel is the Standard Model ZZ production, while $Z + jets$ and $t\bar{t}$ give minor contribution. The direct comparison of the two results is given in fig. 6.8: figure 6.8(b) shows the

	This analysis		$H \to 4\ell$	
m_H (GeV/c^2)	Expected	Observed	Expected	Observed
120	64.79	52.38	5.06	5.00
130	11.39	16.43	1.53	1.81
150	4.14	4.45	0.67	0.63

Table 6.5. Comparison of the expected and observed limit on the Standard Model Higgs boson cross section (expressed as μ/μ_{SM}) in the $\ell^+\ell^- q\bar{q}$ final state as obtained in this analysis and the corresponding results obtained with the Standard Model Higgs boson search performed in the $H \to ZZ^* \to \ell^+\ell^-\ell^+\ell^-$ channel in the same data sample

observed limit (solid line) as well as the expected limit with 1 and 2σ variations. As can be seen from this figure, differently from what is obtained in the analysis presented in this thesis the expected limit in this channel at $m_H = 180$ GeV/c^2 is lower than the one at $m_H = 170$ GeV/c^2. As can be seen in [67, 68], the $H \to 4\ell$ analysis is performed varying the cuts on the mass window of the reconstructed off-mass-shell Z boson as a function of the reconstructed $m_{\ell\ell\ell\ell}$. This leads to an optimized mass window for each value of m_H, which gives optimal performances for each mass point. The comparison of the results shown in fig. 6.8 and summarized in table 6.5 for three mass points show how powerful is the $H \to ZZ^* \to \ell^+\ell^-\ell^+\ell^-$ with respect to the analysis presented in this thesis despite the big difference in branching ratio (see section 1.5). Of course another contribution to the difference between the results that we obtained and the one of the four lepton final state comes from the fact that in the latter all the final configuration are used and not only one half of them as it is done in our analysis (as already explained above).

Of course this last comparison does not diminish the results obtained with this analysis: it is just to see at which point and which power this analysis may have with respect to the most powerful search among the available ones in the same mass region. The relevant result is that this has been the first Higgs boson search in ATLAS in this mass range and in this final state, and the results are competitive with those obtained by the CMS collaboration.

6.4 Future and perspectives

As already explained, this is the first search for the Higgs boson in this mass range and in this final state. Even if an Higgs-like particle has already been discovered (see section 1.6), this search and its results may contribute to our understanding of the new particle and its features. In this context the first next step for this analysis is to contribute to the combination of the ATLAS results on the Higgs boson search: here all the results coming from the searches in all its decay channels are combined in order to have a complete result over the whole mass range, as well as the best characterization of the Higgs-like particle under study since all the available information is taken into account.

In addition to this, many improvements with respect to the baseline analysis performed in the high-mass region [64, 63] have been introduced in order to face all the challenges specific to this search. The main improvement among the ones that were introduced is the criterion used to select the jets to build the Z boson candidate explained in section 5.3.3. In section 5.3.3 the χ^2-based jet selection used in this analysis is compared to other possible jet selection criteria. In particular in the high-mass analysis the jet pairs are selected with a simple mass window cut, and all the combination of the three leading jets that satisfy the dijet mass window requirement are used to build the final $m_{\ell\ell jj}$ distribution. It has been proven in the same section that the χ^2-based jet selection criterion has better performances in terms of significance of the signal selection over the background processes, offering the same performances in terms of resolution on the $m_{\ell\ell jj}$ variable. Because of this, one of the future steps for this analysis is to extend what we learned in this search and the tools that were developed to the analysis of the full mass spectrum. Since both the analysis presented in this thesis and the one published by ATLAS in the same final state in the high-mass region [64, 63] make use only of the data collected in 2011 by ATLAS, the new complete analysis shall include also the 2012 data sample. The 2012 data sample has many different features with respect to the 2011 one: an example could be that different luminosity leads to different pileup conditions, but the striking difference which makes the 2012 and 2011 data samples two independent samples is the energy in the center of mass: as already mentioned, in 2011 LHC provided pp collisions at $\sqrt{s} = 7$ TeV while in 2012 the center of mass energy was raised to $\sqrt{s} = 8$ TeV. The increase of the center of mass energy leads to the change of the cross sections for both signal and background processes, thus changing the composition of the data sample under study. This means that to analyze the 2012 data the analysis presented in this thesis can be used as a starting point, but new optimization of many aspects of the selection is needed.

At the end of 2012 an integrated luminosity of ~ 25 fb^{-1} is expected, which is about 5 times the integrated luminosity recorded in 2011 that has been used for this analysis. In addition to this the trigger thresholds that are being used in the 2012 data taking are very similar to those used in 2011, therefore a rough estimation of the improvement that we can expect only including the 2012 data sample in the analysis can be done. It is important to remark that this is just a rough estimation, since, as already mentioned, the 2012 sample has several intrinsic and challenging features which make it different from the 2011 (harsher pileup conditions, different cross sections). In these conditions we can assume the expected limit on the Higgs boson production cross section obtained with this analysis to scale as a function of the square root of the luminosity used in the analysis. Therefore the limit obtained using the 2011 data sample would scale of a factor $\sqrt{L_{\mathrm{tot}}/L_{2011}} \sim 2.5$, where L_{tot} is the total luminosity used in the new analysis, which include both 2011 and 2012 data samples, and L_{2011} is the luminosity of the 2011 data sample. Such an improvement would imply the possibility for this analysis to be able to exclude the presence of the Higgs boson around $m_H = 140$ GeV/c^2, while the expected limit would be about 10 times the Standard Model expectation for $m_H = 125$ GeV/c^2.

Chapter 7

Conclusions

The Higgs boson search in the $120 - 180$ GeV/c^2 mass range in the $H \to ZZ^* \to \ell^+\ell^- q\bar{q}$ decay channel has been presented. It has been the first search for the Higgs boson in the low mass range using the $\ell^+\ell^- q\bar{q}$ final state ever performed in ATLAS. The presence of jets in the final state is one of the most challenging aspects of this analysis, as they may worsen the resolution on the reconstructed Higgs mass and the requirement of at least two jets in the final state gives rise to high background contamination. The main tool developed and used within this thesis to face these problems is the jet pairing method based on a kinematic fit. This method allows to choose the dijet pair among the jets selected in each event by constraining the dijet mass to the Z boson mass, allowing both to reduce combinatorial background and to improve the resolution on the reconstructed Higgs boson mass.

After the full selection is applied to the 4.7 fb^{-1} of data recorded with the ATLAS detector in the 2011 LHC run, no evidence of the Standard Model Higgs boson in this final state is found. Anyway upper limits on its production cross section have been set: the best sensitivity is reached at $m_H = 145$ GeV/c^2 where the expected limit on the Higgs production cross section is $4.1 \times \sigma_{\mathrm{SM}}$, and the observed limit is $3.45 \times \sigma_{\mathrm{SM}}$, while for $m_H \sim 125$ GeV/c^2, that is the mass of the recently discovered Higgs-like boson, the sensitivity of this analysis is $26.21 \times \sigma_{\mathrm{SM}}$ and therefore no additional information can be added to our knowledge of the new particle with the currently analyzed luminosity. The obtained results are competitive with the corresponding results already published, and the expected limit on the Higgs boson production cross section is lower with respect to the one published by the CMS collaboration in the same final state and mass range.

It has been proven that the jet pairing method developed in this thesis gives better performances in terms of significance of the signal over the background with respect to the method used in the baseline Higgs search in this final state, performed in the high-mass ($200 - 600$ GeV/c^2) range. Therefore a great increase of sensitivity is expected in the full mass range using the jet pairing algorithm proposed in this thesis, as well as including in the analysis also the full data sample recorded in the 2012 LHC run. To analyze the 2012 data sample many reoptimization of the analysis selections are needed, since it offers different challenges with respect to the 2011 one. An additional development could be to push the search for new particles beyond the 600 GeV/c^2 limit. In this very-high-mass region theoretical problems concerning the interference of several processes giving similar final states need to be taken into account, but many models beyond the Standard Model [69, 70] foresee new particles with very high masses which may decay to Z boson pairs, and therefore being able to efficiently reconstruct this final state is of crucial importance.

Bibliography

[1] S. L. Glashow, *Partial-symmetry of weak interactions*, Nucl. Phys. **22** no. 4, (1961) 579

[2] S. Weinberg, *A model of leptons*, Phys. Rev. Lett. **19**, (1967) 1264

[3] A. Salam, *Weak and electromagnetic interactions*, in *Elementary particle theory: relaticistic groups and analyticity*, NN. Svartholm, ed., p.367, Almqvist & Wiksell, 1968, Proceeding of the eighth Nobel Symposium

[4] G. 't Hooft and M. Veltman, *Regularization and Renormalization of Gauge fields*, Nucl. Phys. **B44**, (1972) 189

[5] Kenneth G. Wilson, *Confinement of Quarks*, Phys. Rev. D 10, 2445âĂŞ2459 (1974)

[6] Precision electroweak measurements on the Z resonance, Physics Reports, **427** (2006), 257. Available from: http://dx.doi.org/10.1016/j.physrep.2005.12.006, http://dx.doi.org/10.1016/j.physrep.2005.12.006 doi:10.1016/j.physrep.2005.12.006

[7] F. Englert and R. Brout, *Broken symmetry and the mass of gauge vector mesons*, Phys. Rev. Lett. **13**, (1964) 321

[8] P. W. Higgs, *Broken symmetries and the masses of gauge bosons*, Phys. Rev. Lett. **13**, (1964) 508

[9] G. S. Guralnik, C. R. Hagen, and T. W. B. Kibble, *Global conservation laws and massless particles*, Phys. Rev. Lett. **13** (1964) 585

[10] P. W. Higgs, *Spontaneous symmetry breakdown without massless bosons*, Phys. Rev. **145** (1966) 1156

[11] T. W. B. Kibble, *Symmetry breaking in non-Abelian gauge theories*, Phys. Rev. **155** (1967) 1554

[12] De Palma, M. et al., ALEPH: Techincal Report 1983 - CERN-LEPC-83-2

[13] Bartl, W. et al., DELPHI: Techincal Proposal - DELPHI-83-66-1

[14] von Dardel, G., Walenta, A. H., Lubelsmeyer, K., Deutschmann, M., Leiste, R., et al. L3 Technical Proposal. (1983). See the BOOKS subfile under the following call number: QCD197:E951

[15] THE OPAL DETECTOR. TECHNICAL PROPOSAL - LEPC-83-4

[16] Blair, R. et al. The CDF-II detector: Technical design report - FERMILAB-DESIGN-1996-01

[17] Abazov, V. et al. D0 Run IIB upgrade technical design report (2002)

[18] The CDF and D0 collaborations, "Updated Combination of CDF and D0 Searches for Standard Model Higgs Boson Production with up to 10.0 fb-1 of Data", FERMILAB-CONF-12-318-E; CDF Note 10884; D0 Note 6348, arXiv:1207.0449

[19] J. Beringer et al. (Particle Data Group), Phys. Rev. D*86*, 010001 (2012)

[20] http://pos.sissa.it/cgi-bin/reader/conf.cgi?confid=134, XXIst International Europhysics Conference on High Energy Physics

[21] O. S. Brüning, P. Collier, P. Lebrun, S. Myers, R. Ostojic, J. Poole and P. Proudlock, LHC Design Report, CERN, Geneva, 2004

[22] **ATLAS** Collaboration, CERN/LHCC 97-21 (1997)

[23] **ATLAS** Collaboration, CERN/LHCC 97-19 (1997)

[24] **ATLAS** Collaboration, CERN/LHCC 97-20 (1997)

[25] **ATLAS** Collaboration, ATLAS Trigger Performances, ATL-COM-PHYS-2008-067, CERN (2008)

[26] **ATLAS** Collaboration, arXiv:0901.0512v4 [hep-ex], CERN (2008)

[27] T. Cornelissen and W. Liebig, Nuclear Physics B Proceedings Supplements, 172, (2007)

[28] **ATLAS** Collaboration, "The ATLAS Inner Detector commissioning and calibration", Eur. Phys. J. C, 70, 3 (2010) 787-821, DOI: 10.1140/epjc/s10052-010-1366-7

[29] **ATLAS** Collaboration, "Performance of the ATLAS Detector using First Collision Data", JHEP 1009:056,2010 (arXiv:1005.5254)

[30] **ATLAS** Collaboration, arXiv:0901.0512v4 [hep-ex], CERN (2008)

[31] S. Hassani, L. Chevalier, E. Lancon, J. F. Laporte, R. Nicolaidou and A. Ouraou, *A muon identification and combined reconstruction procedure for the ATLAS detector at the LHC using the (MUONBOY, STACO, MuTag) reconstruction packages*, Nucl. Instrum. Meth. A 572, 77 (2007)

[32] T. Lagouri et al., *A muon identification and combined reconstruction procedure for the ATLAS detector at the LHC at CERN*, IEEE Trans. Nucl. Sci. 51, 3030-3033 (2004)

[33] W. Lampl et al., *Calorimeter Clustering Algorithms: Description and Performance*, ATL-LARG-PUB-2008-002

[34] ATLAS-PHYS-PUB-2011-006 (2011)

[35] **ATLAS** Collaboration, *Selection of jets produced in proton-proton collisions with the ATLAS detector using 2011 data*, ATLAS-CONF-2012-020 (2012)

[36] **ATLAS** Collaboration, *Jet energy resolution and reconstruction efficiencies from in-situ techniques with the ATLAS Detector Using Proton-Proton Collisions at a Center of Mass Energy* $\sqrt{s} = 7$ TeV, ATLAS-CONF-2010-054 (2010)

[37] **ATLAS** Collaboration, *Commissioning of the ATLAS high-performance b-tagging algorithms in the 7 TeV collision data*, ATLAS-CONF-2011-102 (2011)

[38] **ATLAS** Collaboration, *Measuring the b-tag efficiency in a top-pair sample with* 4.7 fb^{-1} *of data from the ATLAS detector*, ATLAS-CONF-2012-097 (2012)

[39] **ATLAS** Collaboration, *Performance of Missing Transverse Momentum Reconstruction in ATLAS with 2011 Proton-Proton Collisions at* $\sqrt{s} = 7$ TeV, ATLAS-CONF-2012-101 (2012)

[40] **ATLAS** Collaboration, *Jet energy resolution and reconstruction efficiencies from in-situ techniques with the ATLAS Detector Using Proton-Proton Collisions at a Center of Mass Energy* $\sqrt{s} = 7$ TeV, ATLAS-CONF-2010-054 (2010)

[41] J. Campbell, K. Ellis, C. Williams, *MCFM - Monte Carlo for FeMtobarn processes*, http://mcfm.fnal.gov/

[42] **ATLAS** Collaboration, *Measurement of the cross-section for b-jets produced in association with a Z boson at* $\sqrt{s} = 7$ TeV *with the ATLAS detector*, Phys.Lett.B 706 (2012) 295-313 (arXiv:1109.1403)

[43] GEANT4 Collaboration, S. Agostinelli et al., GEANT4: *A simulation toolkit*, Nucl. Instrum. Meth. **A 506** (2003) 250-303

[44] **ATLAS** Collaboration, *The ATLAS simulation infrastructure*, Eur. Phys. J. **C 70** (2010) 823-874, (arXiv:1005.4568) [physics.ins-det]

[45] M. L. Mangano et al., *ALPGEN, a generator for hard multi-parton processes in hadronic collisions*, JHEP **07** (2003) 001

[46] **ATLAS** Collaboration, *Measurement of the top quark pair production cross section with ATLAS in ppcollisions at* $\sqrt{s} = 7$ TeV *in dilepton final states*, ATLAS-CONF-2011-034 (2011)

[47] S. Frixione, B. R. Webber, *Matching NLO QCD Computations and Parton Shower Simulations*, JHEP **0206** (2002) 029 (arXiv:hep-ph/0204244)

[48] S. Frixione, P. Nason, C. Oleari, *Matching NLO QCD computations with Parton Shower simulations: the POWHEG method*, JHEP **11** (2007) 070 (arXiv:0709.2092)

[49] S. Alioli, P. Nason, C. Oleari, and E. Re, *NLO Higgs boson production via gluon fusion matched with shower in POWHEG*, JHEP **04** (2009) 002 (arXiv:0812.0578)

[50] P. Nason and C. Oleari, *NLO Higgs boson production via vector-boson fusion matched with shower in POWHEG*, JHEP **02** (2010) 037 (arXiv:0911.5299)

[51] S. Jadach, Z. Was, R. Decker and J. H. Kuhn, *The Tau Decay Library Tauola: Version 2.4*, Comp. Phys. Comm. **76** (1993) 361

[52] E. Barberio and Z. Was, *PHOTOS: A Universal Monte Carlo for QED radiative corrections. Version 2.0*, Comp. Phys. Comm. **79** (1994) 291

[53] LHC Higgs Cross Section Working Group, *Handbook of LHC Higgs Cross Sections*, arXiv:1101.0593 [hep-ph]

[54] J. M. Butterworth, J. R. Forshaw, and M. H. Seymour, *Multiparton interactions in photoproduction at HERA*, Z. Phys. **C72** (1996) 637âĂŞ646 (arXiv:hep-ph/9601371)

[55] LHC Cross Section Working Group,
https : //twiki.cern.ch/twiki/bin/view/LHCPhysics/CrossSections
#CERN_Reports_Handbook_of_LHC_Hig

[56] W. Lampl et al., *Calorimeter Clustering Algorithms: Description and Performance*, ATL-LARG-PUB-2008-002 (2008)

[57] M. Cacciari, G. P. Salam, and G. Soyez, *Anti-KT jet clustering Algorithm*, JHEP **04** (2008) 063, (arXiv:0802.1189)

[58] CDF Collaboration, *Measurement of the top quark mass with in situ jet energy scale calibration in the all-hadronic channel using the Template Method with* 5.8fb^{-1}, CDF-10456 (June 2011)

[59] G. Cowan, K. Cranmer, E. Gross, O. Vitells, *Asymptotic formulae for likelihood-based tests of new physics*, Eur.Phys.J.C71:1554,2011 (arXiv:1007.1727)

[60] G. Bozzi, S. Catani, D. de Florian, and M. Grazzini, *Transverse-momentum resummation and the spectrum of the Higgs boson at the LHC*, Nucl. Phys. **B737** (2006) 73âĂŞ120

[61] A. L. Read, *Presentation of search results: the CL_s technique*, J. Phys. G: Nucl. Part. Phys. **28** (2002) 2693-2704

[62] L. Moneta, K. Belasco, K. Cranmer, A. Lazzaro, D. Piparo, G. Schott, W. Verkerke, M. and Wolf, *The RooStats Project*, (2010) Available from: http://arxiv.org/abs/1009.1003, http://arxiv.org/abs/1009.1003 (arXiv:1009.1003)

[63] **ATLAS** Collaboration, *Search for a Standard Model Higgs boson in the mass range 200-600 GeV in the $H \to ZZ \to \ell^+\ell^- q\bar{q}$ decay channel with the ATLAS Detector*, ATLAS-CONF-2012-017 (2012)

[64] **ATLAS** Collaboration, *Search for a Standard Model Higgs boson in the mass range 200-600 GeV in the* $H \to ZZ \to \ell^+\ell^- q\bar{q}$ *decay channel*, CERN-PH-EP-2012-125 (arXiv:1206.2443)

[65] *CMS* Collaboration, CMS PAS HIG-11-027 (2011)

[66] *CMS* Collaboration, *Search for a Higgs boson in the decay channel* $H \to ZZ^* \to \ell^+\ell^- q\bar{q}$ *in pp collisions at* $\sqrt{s} = 7$ TeV, J. High Energy Phys. 04 (2012) 036 (arXiv:1202.1416)

[67] **ATLAS** Collaboration, *Search for the Standard Model Higgs boson in the decay channel* $H \to ZZ^* \to \ell^+\ell^-\ell^+\ell^-$ *with* 4.8 fb^{-1} *of pp collisions at* $\sqrt{s} = 7$ TeV, ATLAS-CONF-2011-162 (2011)

[68] **ATLAS** Collaboration, *Search for the Standard Model Higgs boson in the decay channel* $H \to ZZ^* \to \ell^+\ell^-\ell^+\ell^-$ *with* 4.8 fb^{-1} *of pp collisions at* $\sqrt{s} = 7$ TeV, Phys. Lett. B 710 (2012) 383-402 (arXiv:1202.1415)

[69] M. Kober, B. Koch and M. Bleicher, Phys. Rev. D**76** 125001 (2007)

[70] L. Randall and R. Sundrum, Phys. Rev. D**83** 4690 (1999)